

JAERI - M  
86-067

REPORT OF THE JOINT SEMINAR ON  
HEAVY-ION NUCLEAR PHYSICS AND  
NUCLEAR CHEMISTRY IN THE ENERGY  
REGION OF TANDEM ACCELERATORS(II)

April 1986

Department of Physics

日 本 原 子 力 研 究 所  
Japan Atomic Energy Research Institute

JAERI-M レポートは、日本原子力研究所が不定期に公刊している研究報告書です。  
入手の問合わせは、日本原子力研究所技術情報部情報資料課（〒319-11茨城県那珂郡東海村）  
あて、お申しこしてください。なお、このほかに財団法人原子力弘済会資料センター（〒319-11茨城  
県那珂郡東海村日本原子力研究所内）で複写による実費頒布をおこなっております。

JAERI-M reports are issued irregularly.  
Inquiries about availability of the reports should be addressed to Information Division, Department  
of Technical Information, Japan Atomic Energy Research Institute, Tokai-mura, Naka-gun,  
Ibaraki-ken 319-11, Japan.

© Japan Atomic Energy Research Institute, 1986

---

編集兼発行	日本原子力研究所
印刷	日立高速印刷株式会社

Report of the Joint Seminar on Heavy-Ion Nuclear Physics and  
Nuclear Chemistry in the Energy Region of Tandem Accelerators (II)

Department of Physics  
Tokai Research Establishment  
Japan Atomic Energy Research Institute  
Tokai-mura, Naka-gun, Ibaraki-ken

(Received March 31, 1986)

A meeting of the second joint seminar on Heavy-Ion Nuclear Physics and Nuclear Chemistry in the Energy Region of Tandem Accelerators was held after an interval of two years at the Tokai Research Establishment of the JAERI, for three days from January 9 to 11, 1986.

In the seminar, about 70 nuclear physicists and nuclear chemists of JAERI and other Institutes participated, and 38 papers were presented. These include general reviews and topical subjects which have been developed intensively in recent years, as well as the new results obtained by using the JAERI tandem accelerator. This report is a collection of the papers presented to the seminar.

Organizing Committee

Y. Sugiyama	Japan Atomic Energy Research Institute
A. Iwamoto	"
S. Baba	"
M. Ishihara	The Institute of Physical and Chemical Research

Keywords: Heavy Ion, Tandem Accelerator, Nuclear Physics,  
Nuclear Structure, Nuclear Chemistry

The organizing committee would like to thank all participants for their assistance and cooperation in making the seminar so successful and fruitful.

「タンデム領域の重イオン核物理・核化学の研究会（Ⅱ）報告集」

日本原子力研究所東海研究所物理部

（1986年3月31日受理）

1986年1月9日から11日の3日間、タンデム領域の重イオン核物理・核化学の第2回目の研究会が2年振りに日本原子力研究所東海研究所において開催された。

研究会には日本原子力研究所及び所外の研究所、大学の核物理、核化学部門の約70人が参加し、38の研究報告が発表された。これらの報告には最近集中的に研究開発されたテーマのレビューとトピックス、そしてJAERIタンデム加速器により得られた新しい結果が含まれている。

この報告書は研究会で発表された研究報告をまとめたものである。

研究会世話人 杉山 康治（日本原子力研究所）  
岩本 昭（       "       ）  
馬場 澄子（       "       ）  
石原 正泰（理化学研究所）

研究会の世話人一同は、盛大で成果の多い研究会に出来たことを参加者一同に感謝致します。

## CONTENTS

1. Development of Superconducting Post-accelerator .....	1
S. Takeuchi	
2. RIKEN Ring Cyclotron and Its Experimental Program .....	3
T. Inamura	
3. On the Application of He-jet Transport System and IGISOL .....	5
H. Kudo	
4. Application of Laser Spectroscopy to Heavy-Ion Reaction .....	9
T. Horiguchi	
5. A Study of nuclei Far from Stability by using ISOL .....	12
T. Sekine	
6. Note on the Backbending .....	16
M. Sakai	
7. Existence of the Odd-Spin Rotation-Aligned Band and its Properties .....	21
A. Ikeda	
8. Effects of Bandcrossings on M1-Transition Probabilities at High-Spin States .....	23
M. Matsuzaki	
9. Multiple Coulomb Excitation of Deformed Odd Nuclei .....	27
<u>M. Oshima</u> , S. Kikuchi, S. Ichikawa, T. Aruga, T. Inamura, A. Hashizume and H. Kusakari	
10. High Energy Gamma Rays Emitted from Highly Excited States in the Continuum .....	30
<u>T. Murakami</u> , J. Kasagi, H. Harada, H. Tachibanaki, K. Yoshida, S. Kubono, M. Yasue, M.H. Tanaka, M.S. Lee, M. Ogiwara, H. Fujiwara and S.C. Jeong	
11. Study of In-Beam Gamma-Ray Spectroscopy by $^{58,60}\text{Ni} + ^{28}\text{Si}$ Reactions	33
<u>K. Kuroyanagi</u> , S. Mitarai, Y. Onizuka, S. Suematsu Y. Ishikawa, K. Heiguchi, B.M. Min, J. Taguchi and H. Tomura	
12. Electromagnetic Properties of High-Spin Isomers .....	37
H. Taketani	
13. B(E2) Anomaly in Ground-State Bands in Ce-126 and -124 .....	38
<u>M. Ishii</u> , M. Hoshi, T. Ishii and M. Ogawa	
14. High Spin States in $^{110,112}\text{Sn}$ .....	40
<u>H. Harada</u> , J. Kasagi, T. Murakami, H. Tachibanaki K. Yoshida, Y. Shibata, T. Inamura and T. Kubo	

15.	Description of High-Spin States Using the Interacting Boson Model .....	44
	<u>N. Yoshida</u> and A. Arima	
16.	Heavy-Ion Spectroscopy Viewed from the IBM .....	46
	T. Otsuka	
17.	Highly Excited and High-Spin States in $^{16}\text{O}$ Populated by ( $^{12}\text{C}, ^8\text{Be}_{\text{g.s.}}$ ) Reaction .....	48
	K. Ekuni, S. Shimoura, K. Takimoto, A. Sakaguchi, N. Ikeda, A. Nakamura and M. Fukada	
18.	Giant Resonances in Hot and Rotating Nuclei .....	51
	<u>K. Tanabe</u> and K. Sugawara-Tanabe	
19.	Hartree-Fock Approach for Thermal Nuclei .....	55
	H. Sagawa	
20.	Self-Consistent Transport Coefficients for Damped Large Scale Collective Motion .....	57
	<u>S. Yamaji</u> , H. Hofmann and R. Samhammer	
21.	Neutron Emission from High Temperature Region Formed in Heavy Ion Reactions .....	60
	J. Kasagi	
22.	Phase Anomaly for Elastic and Inelastic Scattering of the $^{19}\text{F}+^{16}\text{O}$ System .....	63
	<u>H. Fijita</u> , N. Kato, T. Tachikawa, T. Sugimitsu, K. Kimura, Y. Ikeda, H. Yamaguchi, Y. Sugiyama, Y. Tomita, H. Ikezoe, K. Ideno, N. Shikazono, S. Kubono and M. Tanaka	
23.	Examination of Spin-Orbit Term in the Optical Potential for Light Heavy Ions .....	67
	<u>T. Yamaya</u> , O. Satoh, K. Katajima, K. Hasegawa, T. Shinozuka and M. Fujioka	
24.	Coupled-Channel Study of ( $^6\text{Li}, \alpha d$ ) and ( $^7\text{Li}, \alpha t$ ) Reactions .....	70
	Y. Sakuragi	
25.	Intermediate Resonances Observed in the $^{12}\text{C}+^{16}\text{O}$ Fusion Channels ..	74
	<u>T. Sugimitsu</u> , K. Kimura, N. Kato, H. Fujita, Y. Ikeda, and Y. Nakajima	
26.	Measurements of Evaporation Residues to Investigate Lower Limiting Angular Momenta in Fusion Reaction .....	77
	<u>H. Ikezoe</u> , N. Shikazono, Y. Tomita, K. Ideno, Y. Sugiyama, E. Takekoshi, T. Tachikawa and T. Nomura	

27.	Angular and Mass Distribution of Fission Fragments .....	80
	T. Nakagawa	
28.	Coincidence Study of Damped Reaction Fragments for the Systems of $^{35}\text{Cl}+^{46}\text{Ti}$ and $^{37}\text{Cl}+^{48}\text{Ti}$ .....	83
	K. Ideno	
29.	Dynamical Decay of Nuclei at High Temperature: Competition between Particle Emission and Fission Decay .....	85
	<u>Y. Abe</u> , H. Delagrange, C. Gregoire and F. Scheuter	
30.	New Approach to Pre-Equilibrium Reaction Theory .....	89
	S. Yoshida	
31.	Anomalous Properties of Spontaneous Fission in Heavy-Actinide Nuclides .....	93
	I. Fujiwara	
32.	Decay Properties of Light Einsteinium Isotopes ( $A \leq 247$ ) .....	97
	<u>Y. Hatsukawa</u> , M. Magara, T. Ohtsuki, K. Sueki, H. Nakahara and I. Kohno	
33.	Ion Exchange Separation of Short-lived Transplutonium Nuclides .....	99
	<u>S. Usuda</u> , H. Yoshikawa and N. Shinohara	
34.	Radioisotope Beam Production at GANIL .....	102
	<u>Y. Gono</u> , K. Hatanaka, R. Bimbot, P. Aguer, G. Bastin R. Anne, H. Delagrange and Y. Schuz	
35.	Nucleus-Nucleus Scattering and the Interaction Radii of Stable and Unstable Nuclei .....	105
	H. Sato	
36.	Sub-barrier Fusion Reactions: Multi-phonon and Isotope Effects .....	109
	<u>N. Takigawa</u> and K. Ikeda	
37.	Subbarrier Fusion Reactions .....	111
	<u>A. Iwamoto</u> and K. Harada	
38.	Transfer Cross Sections for $^{28}\text{Si}+^{58,62}\text{Ni}$ Reactions near the Coulomb Barrier .....	114
	<u>Y. Sugiyama</u> , Y. Tomita, H. Ikezoe, K. Ideno, N. Shikazono, N. Kato, H. Fujita, T. Sugimitsu and S. Kubono	

---

Speakers in paper of collaboration are denoted by underlines.

## 1. Development of Superconducting Post-accelerator

Suehiro Takeuchi

Department of Physics, Japan Atomic Energy Research Institute

JAERI is presently considering the construction of a 30 MV superconducting linac for the tandem, which will boost the beam energy enough for the heavy ion experiments with a mass number up to about 120. The reporter has started the development of a niobium superconducting quarter wave resonator. The first resonator for testing is being fabricated by Mitsubishi Electric Corporation, Kobe.

Superconducting linacs and their resonators developed for the tandems at a number of laboratories are shown in table 1. The construction of many of the superconducting linacs was stimulated by the success at the two leading laboratories, Argonne National Laboratory and State University of NY, Stony Brook. The attractive feature of the superconducting linacs is that they consume only about 10 times less electrical power than normal-conducting ones do. The substantial power is used for the refrigeration system but not at all for the rf power system. The heavy ion linacs with modular structure and independently phased resonators are well matched to the broad range of ion beams from tandems. The modular structure is also advantageous for the construction, as it is seen in the table that a number of laboratories have started with a small project with the intension of adding on more modules later.

ANL and State University of NY developed split-ring(SLR) resonators for their linacs with niobium and lead-plated copper, respectively.

Recently, Table 1. Superconducting post-accelerators for tandems

quarter wave (QW) line resonators	Laboratory	Super- conductor, resonator	Injector	Status
are prevail-	Argonne Nat. Lab.	Nb SLR	FN	50 MV completed(ATLAS)
ing at many	Florida State Univ.	Nb SLR	FN	12 MV under construction
laboratories.	CEN Saclay	Nb Helix	FN	under construction
	SUNY, Stony Brook	Pb SLR	FN	20 MV completed(SUNYLAC)
	Oxford University	Pb SLR	up-down 10MV	1 module under construction
They have	Tata Inst. Bombay	Pb SLR	14UD	1 module under construction
	Weizmann Inst.	Pb QW	14UD	1 module under construction
good points	U. of Washington,Seattle	Pb QW	Dual FN	26 MV under construction
such that	Australian Nat. Univ.	Pb QW	14UD	1 module under construction



1) the simple structure is convenient for their fabrication, 2) it is highly rigid to give good stability of the resonant frequency, and 3) the acceptable velocity range for incident ions is broad. All the QW resonators in the table are made of lead-plated copper. A QW resonator made of niobium was also fabricated and tested at Argonne<sup>1)</sup>. It generated the accelerating field level of 4.7 MV/m with rf dissipation of only 2.8 watts. This remarkable result makes us decide to develop niobium QW resonators for our linac.

Our first niobium model resonator is illustrated in fig. 1. The center conductor, the drift tube and the upper shorting plate are made of pure niobium. The outer conductor and the bottom cover plate are made of explosively bonded niobium-copper plates. The optimum velocity of the incident beams is one-tenth of the light velocity,  $c$ . The lowest limit of the velocity range is  $0.045 c$ . The resonant frequency is 128 MHz. This resonator will be able to accelerate ions with a mass number up to 210 from the tandem with a terminal voltage of 16 MV and with a foil stripper, and up to 120 with a gas stripper.

In order to realize a 30 MV linac, about 40 of these resonators need to be employed on the assumption that the accelerating field level of 4.7 MV/m is attainable. They will be put into five cryostats, each of which cools 8 resonators and 2 superconducting solenoids. The basic beam bunch frequency will be 32 MHz (or 64 MHz). We will use same QW resonators for the post buncher and the de-buncher. In the fiscal year of the 1986, we are going to make resonators for the post buncher and its cryostat. For the construction site, two plans are still under consideration. One is to put the linac at the end of the zero degree target beam line from the beam switching magnet. New target room is necessary. The other is to put the linac south of the analysing magnet of the tandem to lead the beams to the present target rooms.

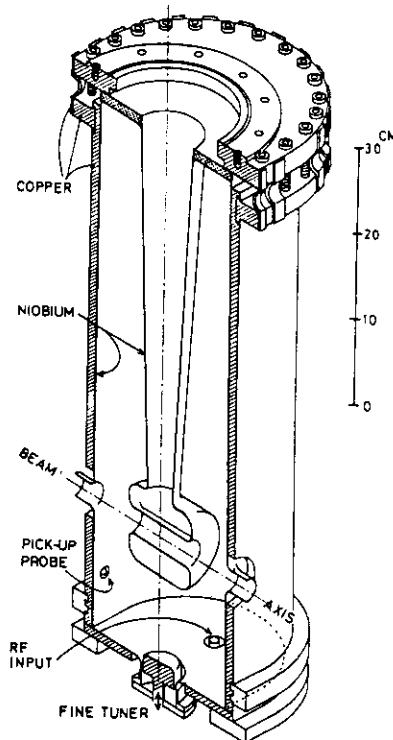


Fig. 1. A niobium superconducting quarter wave resonator.

1) K. W. Shepard, S. Takeuchi and G. P. Zinkann:  
IEEE Trans. on Magnetics MAG-21(1985)146.

## 2. RIKEN Ring Cyclotron and Its Experimental Program

Takashi Inamura

Cyclotron Laboratory, RIKEN

Construction of the RIKEN Ring Cyclotron(K=540) started in 1980. The construction work is almost on schedule and the first beam is expected this October.

The plan view of the Ring Cyclotron facilities is presented in Fig. 1. A slight modification has been made to accommodate time-sharing of beams between different experimental vaults and a radioisotope beam channel. The Ring Cyclotron can accelerate every element in the periodic table. Characteristics of beams are summarized in Tables 1 and 2. Beams except protons are injected from RILAC, a heavy-ion linear accelerator. Protons are injected from an AVF cyclotron with K=65 which will be completed by 1989; light heavy-ions with  $A < 40$  are also injected from the AVF cyclotron when their energies are required to be greater than 70 MeV/n.

The first beam will be  $^{40}\text{Ar}$  ions with the energy of about 26 MeV/n.

Experimental program is as follows. Firstly, an on-line mass

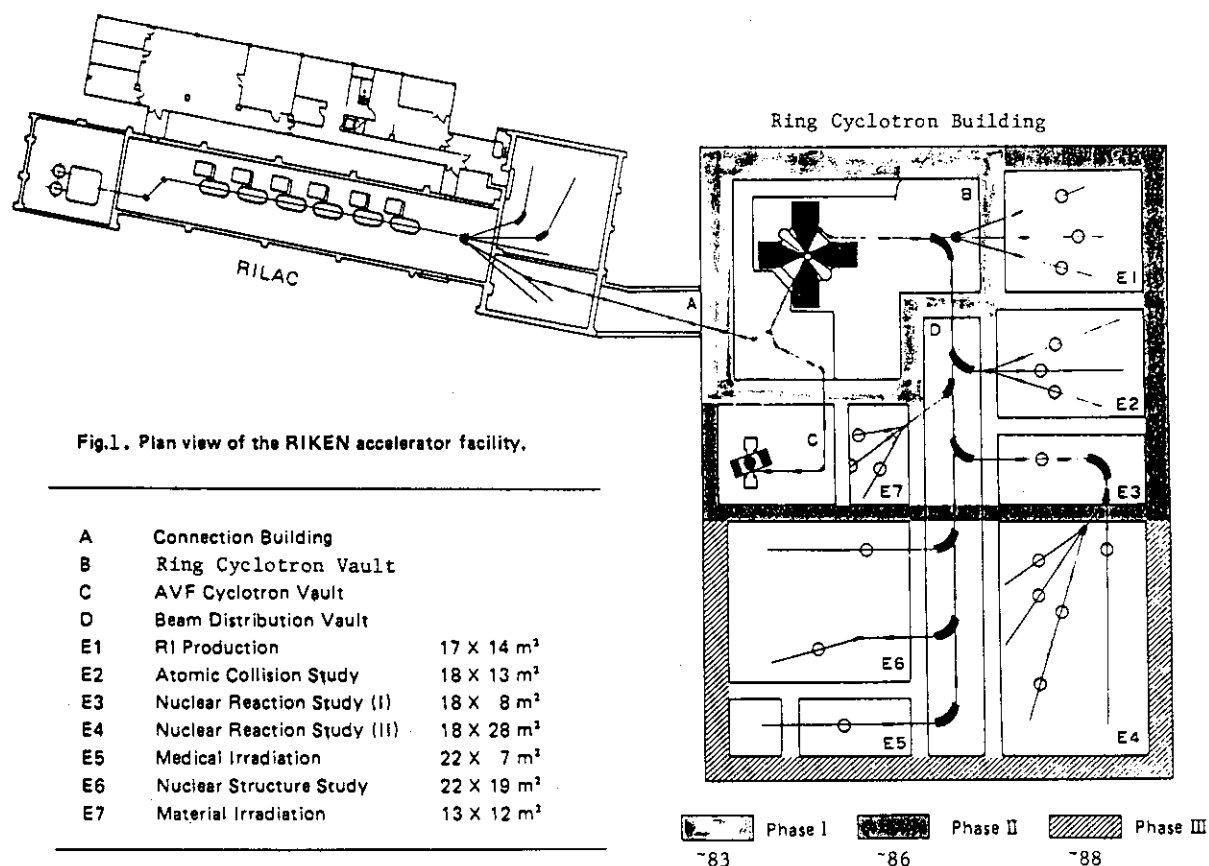


Table 1. Characteristics of beams from the Ring Cyclotron.

Maximum energy per nucleon	
proton	210 Mev
$^3\text{He}$	185 MeV/u
d, alpha	135 MeV/u
Heavy ion	$540 (q/A)^2$ MeV/u
Energy resolution	0.05%
Emittance	$1.25 \pi$ mm mrad
Time resolution	200 ps

Table 2. Characteristics of beams on target.

Dispersive transport	
Energy resolution	0.01%
Achromatic transport	
Energy resolution	0.02%
Isochronous transport	
Time resolution	300 ps

separator and a radioisotope beam channel will be installed to study nuclei far from stability. Nuclear laser spectroscopy facilities will also be installed, being combined with the first two facilities. Secondly, a station for particle correlation experiments will be completed to study the hot and dense nuclear matter produced in heavy-ion collisions and the heavy-ion reaction mechanism. Pion/muon facilities are also installed for material science as well as for heavy-ion nuclear physics. Thirdly, a high resolution particle spectrometer and a neutron time-of-flight facility will be installed.

Besides these nuclear physics facilities, atomic physics and biomedical facilities are to be installed. A biological irradiation device will be placed at the earliest stage of commissioning.

## 3. On the applications of He-jet transport system and IGISOL

Hisaaki Kudo

Department of Chemistry, Faculty of Science, Niigata University

In recent years, a gas-jet transport system is widely used for the study of short-lived nuclides. The gas-jet transport system is not only useful as it is, but also capable of various combinations with other experimental facilities such as those for rapid chemistry and on-line isotope separation. An example of a helium-jet transport system is shown in Fig.1-3, which is constructed at RIKEN for the study of heavy-ion induced reactions.<sup>1)</sup> This system consists of the aerosol generator (Fig.1), the reaction chamber (Fig.2), and the collection tape system (Fig.3). By use of this system, the nuclide of a half life down to 119 ms ( $^{212}\text{At}$ ) was identified in the reaction of 100 MeV  $^{16}\text{O}$  on  $^{209}\text{Bi}$ .

There are two ways for the gas-jet coupled rapid chemistry. One is based on the ordinary solution chemistry, and the other is carried out by use of a gas phase chemistry. To subject recoil products to an ordinary chemical separation, it is necessary to transfer the products to suitable solution from huge amount of carrier gas. Once the recoil products are dissolved in a solution, various kinds of chemical separations can be applicable. For continuous conversion of gas phase to liquid phase, it is useful to employ such techniques as adsorption on soluble material,<sup>2)</sup> introduction of gas to mixer and centrifuge.<sup>3)</sup> An alternate method for separation is a gas-phase chemistry. In this method, recoil products are subjected to gas chromatography,<sup>4)</sup> thermochromatography,<sup>5)</sup> adsorption on char coal or glass wool,<sup>6)</sup> etc, after adding some complexing agent when necessary. For the more fast chemistry, a partial separation in the course of the thermalization and/or the transportation processes<sup>7)</sup> could be useful.

In any case, an accelerator beam line should be held at high vacuum, whereas the pressure inside the target chamber needs to be maintained at about 1 atm. It seems to be very effective especially in the accelerator required a high vacuum to use such a kind target system as that at the UNILAC.<sup>8)</sup> This target system has two different security systems to avoid a gas flow into the accelerator vacuum. One is a temperature monitoring

system and the other is a fast closing valve system.

Comparing with the usual on-line mass separator, a gas-jet coupled mass separator has several advantages. For example, (1) a measurement of rare events can be carried out at a low background site, (2) a precious target can be used repeatedly, (3) the time spent in an ion source is greatly reduced in the case of the element having a long diffusion time, (4) usually it is easy to prepare a target in a desired form, and (5) a target material itself is not introduced into the ion source, which is essential to use of a highly radioactive material as a target. On the other hand, it also has disadvantages as can be seen from the fact that only recoiled-out products can be available for the mass separation, thus the yields may be small. Some examples of gas-jet coupled mass separators are UNISOL at Oak Ridge,<sup>9)</sup> RAMA at Berkeley,<sup>10)</sup> HELIOS at Mainz,<sup>11)</sup> and KUR-ISOL at Kyoto.<sup>12)</sup> The former two are installed in accelerators, while the latter two are in reactors. All of these examples have their own ion source for mass separation. Recoil atoms carried by gas-jet are once introduced to the ion source, and (re-)ionized there by the suitable method. Therefore, the overall

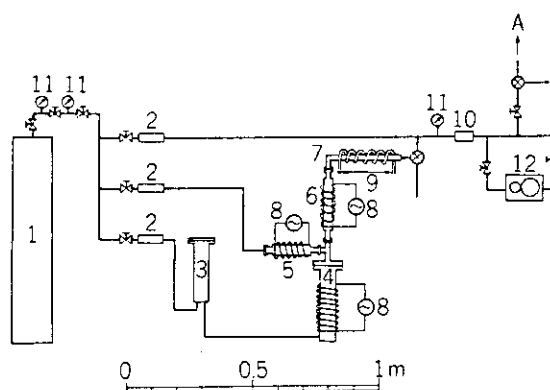


Fig. 1. Aerosol generator and gas supply system  
1: helium gas, 2: rotameter, 3: reservoir, 4: nebulizer, 5: nucleator, 6: reheater, 7: condenser, 8: temperature-controlled heater, 9: water cooling, 10: check valve, 11: pressure gauge, 12: compressor.

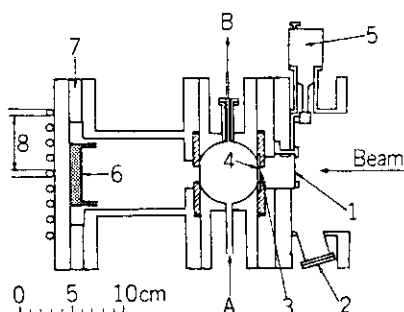


Fig. 2. Reaction chamber  
1: energy degrader, 2: viewer, 3: vacuum seal foil, 4: target, 5: vacuum sealed rotator, 6: graphite beam stopper, 7: insulator, 8: water cooling.

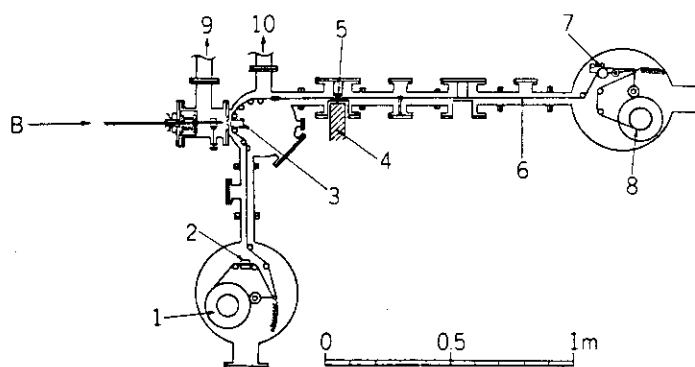


Fig. 3. Collection tape system  
1: feed reel, 2: photo-sensor, 3: heater, 4: Ge(Li) detector position, 5: Si (Au) detector position, 6: collection tape, 7: pulse motor, 8: take-up reel, 9: to roots pump, 10: to diffusion pump.

efficiency of mass separation depends largely on the ionization process. There seems to be no universal ion source suited for any elements. It is also very difficult to design and construct an efficient ion source even in the case of gas-jet coupled mass separator, because of requirements for operation at a high uniform temperature.

Under the circumstances, a new kind of an isotope separator which does not have an ion source is developed at the University of Jyvaskyla, Finland.<sup>13)</sup> The main part of this separator is shown in Fig.4. Recoil products which are highly charged immediately after the nuclear reaction are thermalized by collision with carrier gas with reducing their charges. However, not all of them become neutral, but some remain as +1 ions. These ions together with carrier gas go through the exit hole of thermalizing room (3), pass through the hole of skimmer (4) being directed by an electric field, and are accelerated with the extraction electrode (5). From the fact that primary ions are used in this type of mass separator, it is called an Ion-Guide Isotope Separator On-Line (IGISOL). This method allows a fast ( $\sim 1$  ms) separation of various elements including highly refractory elements, such as Cr, V, Nb, Mo, Tc, W, with an efficiency of 1 - 10 %, where the efficiency refers to the ratio of the number of mass separated atoms to that of recoiled ones. Up to now about 50 kinds of nuclear reactions have been investigated by use of IGISOL, and this method has been found very useful. However, the mechanism of ion-guide has not been

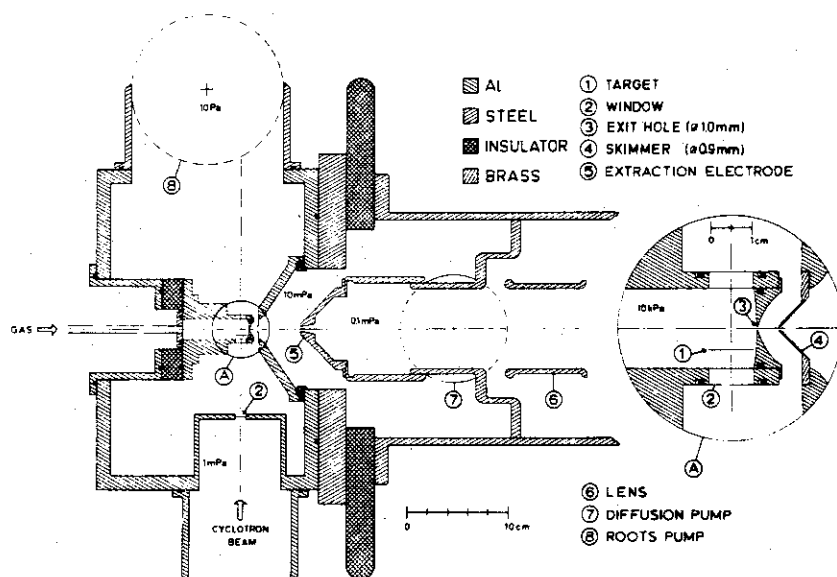


Fig.4. Main part of IGISOL.<sup>13)</sup>

explained quantitatively, because of difficulties arising from wide pressure ranges and high applied voltage, and also difficulty in understanding the atomic collision process in the range of very low kinetic energies (below 1 eV). A small amount of concomitants, such as  $N_2$ ,  $O_2$ ,  $H_2O$ , in carrier gas (usually helium) seems to play an important role.<sup>13)</sup> These problems should be solved in the future.

The application of IGISOL have been limited in light-ion induced reactions so far, in which recoil ranges of reaction products are short so that the volume of the thermalizing room can be made small and the pressure in it need not be high. For the separation of products with considerable recoil energy by this ion-guide technique, there are some problems to be settled: (1) will recoil products survive as +1 ions in a higher helium pressure and/or in a large thermalizing room (the evacuation time increases linearly with its volume) ? (2) what will be the consequence of the impact of an intense, high energetic beam of heavy ions inside the reaction chamber ? Preliminary investigations on the application of IGISOL to heavy-ion induced reactions are now in progress at Leuven University, Belgium, and at the Institute for Nuclear Study of University of Tokyo.

#### References

- 1) H.Kudo et al, RIKEN Accel. Prog. Rep. 18, 127(1984)
- 2) E.K.Hulet et al, J. Inorg. Nucl. Chem. 42, 79(1980)
- 3) N.Trautmann et al, Inorg. Nucl. Chem. Letters, 11, 729(1975)
- 4) R.D.von Dencklage et al, Nucl. Instrum. Methods,176,529(1980)
- 5) U.Hickmann et al, Nucl. Instrum. Methods,175,507(1980)
- 6) M.Zendel et al, Nucl. Instrum. Methods,153,149(1978), K.Rengan et al, Nucl. Instrum. Methods,197,427(1982)
- 7) K.L.Kosanke et al, Nucl. Instrum. Methods,125,253(1975), C.Cabot et al, Nucl. Instrum. Methods,125,397(1975)
- 8) E.Georg et al, Nucl. Instrum. Methods,157,9(1978)
- 9) W.D.Schmidt-ott et al, Nucl. Instrum. Methods,124,83(1975)
- 10) D.M.Molts et al, Nucl. Instrum. Methods,172,507(1980)
- 11) A.K.Mazumdar et al, Nucl. Instrum. Methods,174,183(1980)
- 12) K.Okano et al, Nucl. Instrum. Methods,186,115(1981)
- 13) J.Aysto et al, Phys. Letters, 138B, 369(1984), J.Arje et al, Phys. Rev. Letters, 54, 99(1985)

## 4. Application of laser spectroscopy to heavy-ion reaction

T. Horiguchi

Faculty of Science, Hiroshima University

In recent years, Isotope shifts, magnetic moments and electric quadrupole moments of various short-lived nuclides were measured by the laser spectroscopy with tunable dye laser.<sup>1)</sup> However, the study was limited to nuclides which were produced by proton spallation reaction or fission because of their production yields. Recently, neutron-deficient In isotopes produced by heavy-ion reaction were studied by the laser spectroscopy with GSI-ISOL.<sup>2,3)</sup> The author partly participated in the experiment and the results will be reported.<sup>4)</sup> Moreover, the trial of highly-sensitive detection scheme with the field ionization of Rydberg states will be mentioned.

Neutron-deficient In-isotopes were produced by  $\text{Mo}(^{16}\text{O}, \text{pxn})\text{In}$  reactions with UNILAC accelerator at GSI, and separated with GSI-ISOL. The general layout of the laser spectroscopy apparatus is shown in Fig. 1.

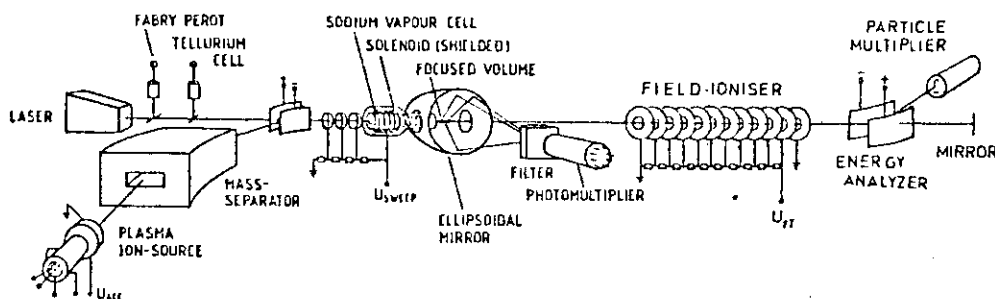


Fig. 1 Set-up of collinear fast-beam laser spectroscopy at GSI-ISOL.

In-isotopes were ionized with FEBIAD-B type ion-source<sup>5)</sup>, mass-separated and led to laser spectroscopy course after the deflection of  $60^\circ$ . The laser light is collinearly passing through the course. This light is produced by the ring dye laser (Coherent CR699-21) pumped by Ar-ion laser (CR18). Indium atoms, after being neutralized in Na charge-exchange cell, are resonantly excited by the 451 nm light ( $5p\ ^2P_{3/2} - 6s\ ^2S_{1/2}$ ) (Fig. 2). Fluorescence lights of 411 nm ( $6s\ ^2S_{1/2} - 5p\ ^2P_{1/2}$ ) are collected by an ellipsoidal mirror and counted by a photomultiplier. Fluorescence spectrum is measured by the laser frequency scanning or the voltage-sweep of acceleration-retardation electrode (Doppler tuning) in front of the charge-exchange cell.

To increase the detection sensitivity of In isotopes, The pulse-operation of FEBIAD-IS was tried. During the irradiation, Mo target container was cooled by the contact of water-cooled Cu-cone. Produced In isotopes were



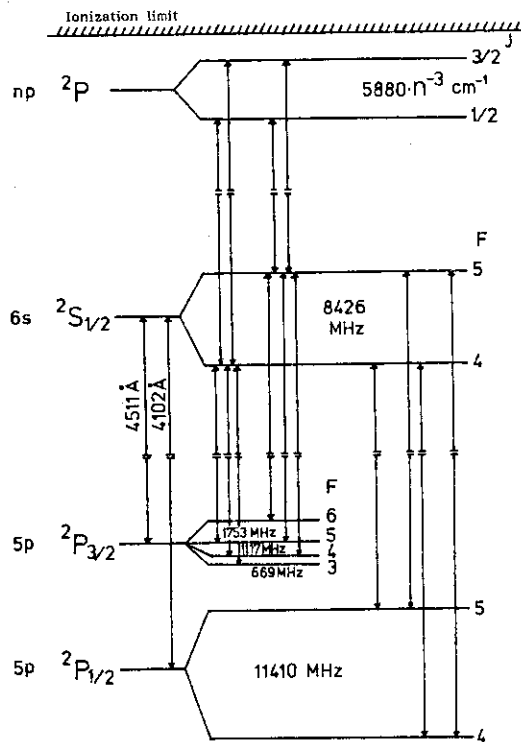


Fig. 2 Hyperfine splitting of 5p-6s transitions of  $^{115}\text{In}$ .

trapped in a cold part, and after the irradiation, evaporated from the part with the temperature increase and ionized. The time profile of extracted  $^{108}\text{In}$  is shown in Fig. 3, a). Most In atoms were extracted within about 1 s from 0.3 s after the stop of cooling. Fluorescence spectrum of  $^{108}\text{In}$  measured by Doppler tuning is shown in Fig. 3, b).

In addition to 6 HFS transitions of  $^{108g}\text{In}$  ( $T_{1/2}=53\text{m}$ ,  $I=7$ ), 5 HFS transitions of  $^{108m}\text{In}$  ( $T_{1/2}=40\text{m}$ ) were newly measured. By the pulse operation of ion-source, The S/N ratio was improved about 700 times<sup>4)</sup> compared with the usual operation.<sup>2)</sup> From HFS splittings, the following results were obtained;

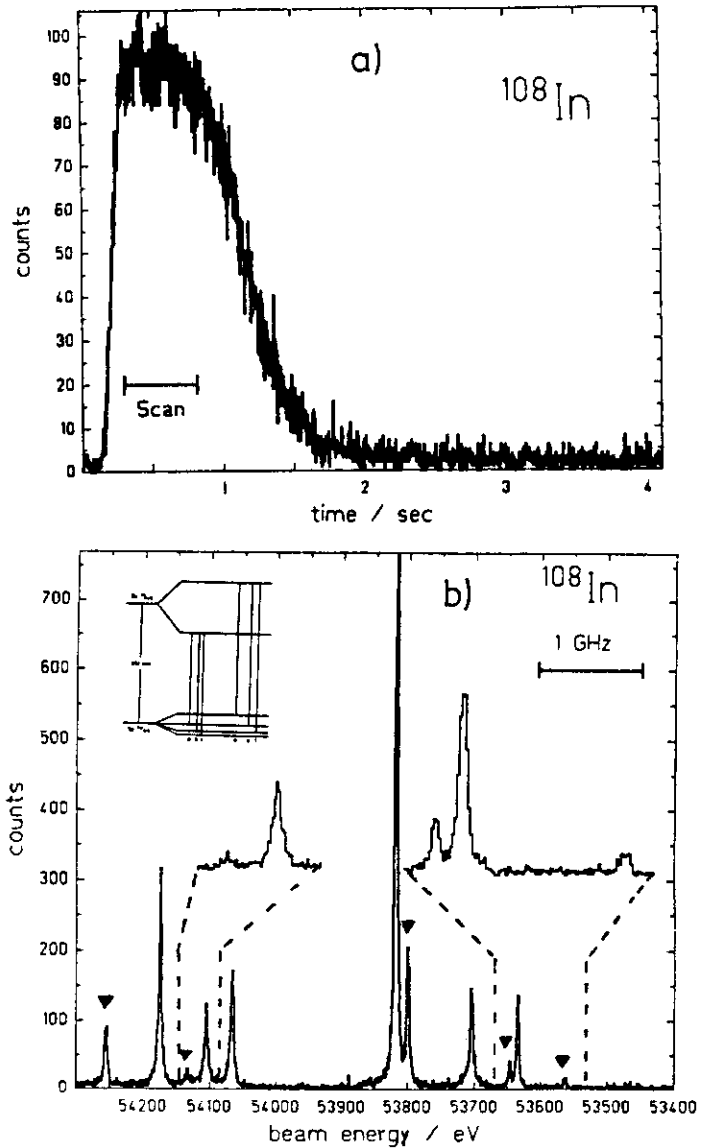


Fig. 3 a) Time profile of mass-separated  $^{108}\text{In}$  for the pulse operation of ion-source.  
b) Fluorescence spectrum of HFS of  $5p\ 2P_{3/2}-6s\ 2S_{1/2}$  transition. The lines marked by triangle belong to newly identified  $^{108m}\text{In}$ .

$\mu_1 = 4.561(3)$  nm,  $Q_s = 1.005(7)$  b for  $^{108g}\text{In}$  and  $I=2$ ,  $\mu_1 = 4.935(5)$  nm,  $Q_s = 0.467$  (14) b for  $^{108m}\text{In}$ , respectively.<sup>4)</sup>

In the series of experimental studies,<sup>2-4)</sup> laser resonance fluorescence spectroscopy of neutron-deficient In isotopes produced by heavy-ion reactions was successfully carried out. This method is relatively simple and also highly sensitive. The wave-lengths of the most promising ground-state transitions for use in resonance fluorescence method are shown in Table 1.

Future ( 50 - 210 nm )		Frequency-doubled or pulsed dye laser ( 210 - 420 nm )		CW dye laser ( 420 - 800 nm )	
H	121.6	Be	234.9	Li	670.8
He	59.1	B	249.7	Na	589.0
N	120.1	C	296.7	K	766.5
O	135.9	Mg	285.2	Ca	657.3
F	95.6	Al	396.1	Sc	621.1
Ne	74.4	Si	251.4	Ti	517.4
P	177.5	Ni	362.5	V	485.1
S	191.5	Cu	327.4	Cr	429.0
Cl	139.6	Zn	307.6	Mn	543.3
Ar	106.7	Ga	403.3	Fe	511.0
As	193.7	Ge	265.2	Co	423.4
Se	207.7	Mo	390.3	Rb	780.0
Br	154.1	Ru	392.6	Sr	460.7
Kr	125.0	Rh	369.2	Y	622.3
I	178.3	Pd	276.3	Zr	613.5
Xe	149.1	Ag	338.3	Nb	525.2
Rn	178.6	Cd	326.1	Tc	592.5
		In	410.5	Cs	459.3
		Sn	286.3	Ba	553.5
		Sb	231.1	La	550.1
				Ce	556.8
				Pr	513.3
				Nd	614.9
				Sm	562.6
				Eu	601.8
				Gd	570.9
				Tb	537.6
				Er	582.7
				Tm	597.1
				Yb	555.6
				Lu	573.7
				Hf	618.5
				Ta	540.3
				W	498.3
				Re	527.6
				Os	442.0
				Pr	780.0
				Ra	482.6
				Ac	636.0
				Th	576.1
				U	591.5
				Pu	586.5
				Am	605.5
				Es	520.4

Table 1. Wave-length of ground-state transition for each element.

However, in order to extend the laser spectroscopy study to the region of  $^{100}\text{Sn}$ , it is needed to develop much more highly-sensitive detection scheme because of the small production yields. Now, the preliminary study is being carried out at GSI-ISOL, which is two-photon excitation to high-n Rydberg state following field ionization and ion-counting (the latter part of Fig. 1). In the test experiment using stable  $^{115}\text{In}$  isotope ( $5p\ ^2P_{3/2}-6s\ ^2S_{1/2}-29p\ ^2P_{3/2}$ ), detection sensitivity was  $2.5 \times 10^{-6}$  counts/primary ion.<sup>6)</sup> Out of the various factors contributing to the sensitivity, the largest one is two-photon excitation probability to high-n Rydberg state (about  $3 \times 10^{-4}$ ). To improve this factor, an optical passive resonator for two-photon excitation of fast-atomic beam was constructed and the test is now in progress.

#### Reference

- 1) E. W. Otten, Proc. 1984 INS-RIKEN Int. Symp. Heavy Ion Phys., Tokyo and J. Phys. Soc. Jpn. 54 (1985) Suppl. I, 59
- 2) G. Ulm et al., Z. Phys. A321 (1985) 395
- 3) H. Lochmann et al., Z. Phys. A322 (1985) 703
- 4) J. Eberz et al., submitted to Z. Phys.
- 5) R. Kirchner et al., Nucl. Instr. Meth. 186 (1981) 295
- 6) U. Dinger, Diplomarbeit in Mainz Universität, 1985

## 5. A Study of Nuclei Far from Stability by Using ISOL

Toshiaki Sekine

Production Development Division, Department of Radioisotopes, Japan Atomic Energy Research Institute

An isotope separator on-line (ISOL) to a heavy-ion accelerator is a powerful instrument for studying nuclei far from the beta-stability line. Recently, new type mass separators without ion source, recoil mass separator and ion-guide ISOL, have been constructed to extend the range of accessible isotopes to shorter half-lives and to obtain mass-separated beams without elemental selectivity. On the other hand, for conventional ISOLs with ion source, many efforts have been made to develop elemental selectivity, so as to obtain mono-isotopic beams, as well as versatility in ionization. The present report describes two topics with respect to the use of ISOL with ion source; readers may refer to a comprehensive review on this field by Hardy et al.<sup>1)</sup> First, examples of applying elemental selectivity in ionization are presented. Second, we shall show the result of the decay study of the new  $T_z = -1$  nucleus  $^{48}\text{Mn}$  by taking advantage of mass separation using a new FEBIAD ion source with extended versatility.

## Chemical separation in ion source

Generally, an ion source must be operated at high temperatures. This requirement limits the lifetime of the ion source, and demands usually heat-shieldings between target and ion-source window. From the second thing, an extra recoil energy is needed for products to pass through foils of heat shield. Although high temperature operation seems a disadvantage, temperature is a crucial factor for chemical separation in the ion source, as seen in the following examples.

Surface ionization has been used in many ISOLs to ionize elements with relatively low ionization potential such as alkali, alkaline-earth, and rare-earth elements. Therefore, surface ionization gives elemental selectivity to a certain extent. Further, using a tantalum recoil catcher in a surface ion source, Karnaukhov et al.<sup>2)</sup> found a strong dependence of the yield of  $^{121}\text{Ba}$ , produced in the reaction  $^{32}\text{S} + \text{Zr}$ , on the ionizer temperature between 2000 K and 2700 K. This fact was applied by Ichikawa et al.<sup>3)</sup> to

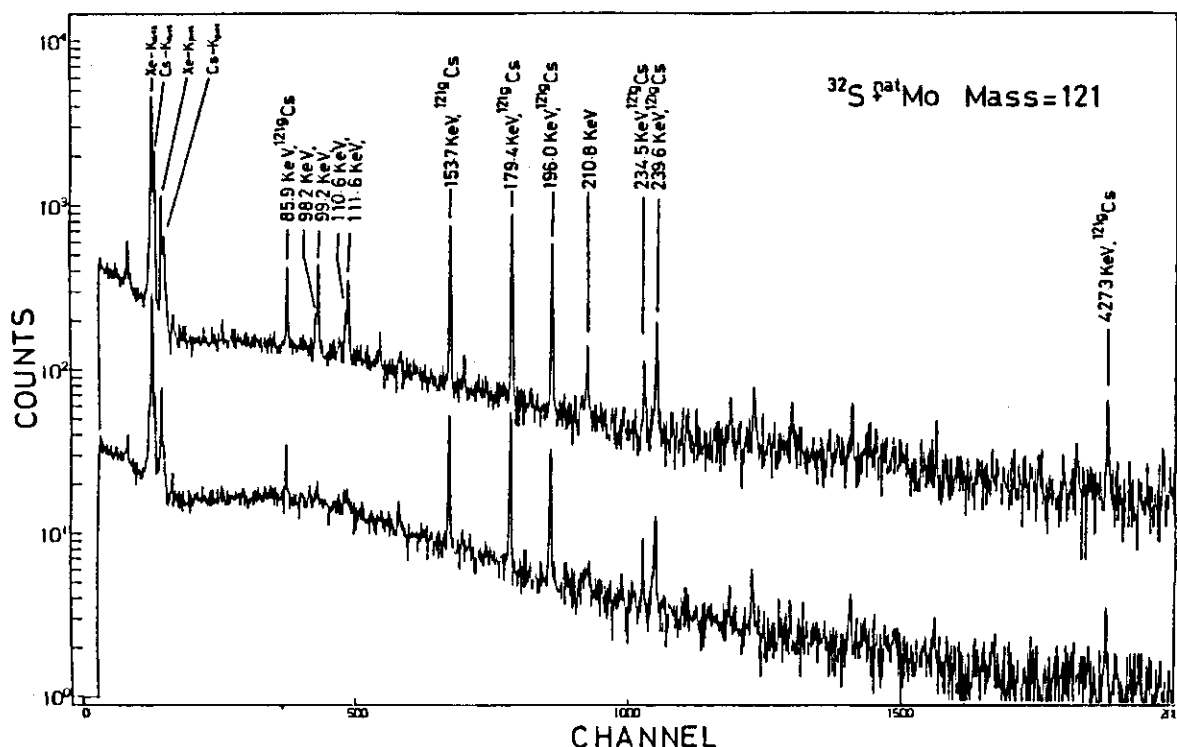


Fig. 1 Gamma and X-ray spectra obtained for  $A=121$  in the  $5.2\text{-MeV/u } ^{32}\text{S} + ^{nat}\text{Mo}$  reaction at the ionizer temperatures of  $\sim 2700\text{ K}$  (upper part) and  $\sim 2200\text{ K}$  (lower part). Gamma lines around  $100\text{ keV}$  and Cs X-rays reduced considerably at the lower temperature are assigned to  $^{121}\text{Ba}$ .<sup>3)</sup>

assignment of newly-observed gamma rays to  $^{121}\text{Ba}$ , as shown in Fig. 1. The behaviour of the barium isotope observed here would be understood, considering the thermionic electron emission from the inner wall of hot cavity.<sup>4)</sup>

In the above technique, ion-source temperature was kept constant. On the other hand, a novel ion-source technique, "bunched beam-release," tested successfully at the GSI ISOL<sup>5)</sup> applies the temporal variation of temperature. In this method, a target acting as a catcher is placed in a pocket the temperature of which can be reduced by contact with a movable cooling block. The pocket is cooled for storage of reaction products. After an accumulation period, the temperature is increased and the reaction products are released from the pocket for ionization. In the reaction  $^{16}\text{O} + ^{97}\text{Mo}$ ,  $^{108}\text{In}$  nuclei accumulated during 10 min were found to be released within less than 1 sec, while the isobaric product  $^{108}\text{Sn}$  was released more slowly. The high indium beam intensity during the short release interval resulted in a substantial improvement of the signal-to-noise ratio in collinear laser spectroscopy for  $^{108}\text{In}$ [6]. Furthermore, such a storage-release procedure offers the possibility of doing chemical separation by setting time windows due to the element specific release profiles.

Decay study of the new  $T_z = -1$  nucleus  $^{48}\text{Mn}$ 

The  $T_z = -1$  nucleus  $^{48}\text{Mn}$  was searched for by making use of the GSI ISOL. This nucleus was produced in the bombardment of  $^{12}\text{C}$  target with a  $^{40}\text{Ca}$  beam, through the lp3n channel. The  $^{12}\text{C}$  target (graphite 0.15 mm thick) was placed inside the ion source, acting as a catcher. Such a thick target is considerably advantageous in production of the  $^{48}\text{Mn}$  nuclei with cross sections predicted to be as small as 30  $\mu\text{b}$  at maximum.

The  $^{48}\text{Mn}$  nucleus was identified first in a test experiment<sup>7)</sup> with a half-life of  $150 \pm 10$  ms and strong gamma lines at 752.1 keV ( $2^+ \rightarrow 0^+$ ) and 1106.1 keV ( $4^+ \rightarrow 2^+$ ). In a recent measurement, detailed decay spectroscopy was performed for this nucleus.<sup>8)</sup> From gamma-gamma coincidence data, measured for higher transition energies, higher-lying levels were identified, including the  $4^+$ ,  $T=1$  isobaric analogue state at  $5792.4 \pm 0.6$  keV in  $^{48}\text{Cr}$ . Beta-delayed proton emission was observed for  $^{48}\text{Mn}$  with an intensity of  $0.5 \pm 0.1\%$  per decay, which extends the  $A=4n$ ,  $T_z = -1$  family of precursors beyond the so-far heaviest member  $^{44}\text{V}$ .

In the above experiments, an ultra-high temperature discharge ion source FEBIAD-F<sup>9)</sup> was utilized. Mass-separated beam intensities obtained with this ion source are summarized in Table 1 for fusion-evaporation residues in the reaction 7.3- or 10.4-MeV/u  $^{40}\text{Ca} + ^{12}\text{C}$ . The values are normalized to a  $^{40}\text{Ca}$ -beam current of 100 particle nA; typical beam currents were 50 to 100 particle nA. One can note in Table 1 that the known  $T_z = -3/2$

Table 1. Yields of fusion-evaporation residues produced in the 7.3-MeV/u  $^{40}\text{Ca} + ^{12}\text{C}$  reaction and mass-separated using FEBIAD-F ion source

Nuclide	$T_z$	Half-life	Observed Radiation	Reaction channel	Yield (atoms/sec at 100 particle nA)
$^{49}\text{Fe}$	-3/2	0.075 s	$\beta\text{p}$	3n	$\geq 3 \times 10^{-1}$ *)
$^{50\text{m}}\text{Mn}$	0	1.75 m	$\gamma$	1p1n	$2.2 \times 10^5$
$^{49}\text{Mn}$	-1/2	0.384 s	$\beta$	1p2n	$1.7 \times 10^4$
$^{48}\text{Mn}$	-1	0.150 s	$\beta$	1p3n	$1.8 \times 10^2$
$^{49}\text{Cr}$	+1/2	42.1 m	$\gamma$	2p1n	$1.5 \times 10^6$
$^{47}\text{Cr}$	-1/2	0.50 s	$\beta$	$\alpha\text{n} + 2\text{p}3\text{n}$	$2.1 \times 10^4$
$^{45}\text{Cr}$	-3/2	0.04 s	$\beta\text{p}$	$\alpha 3\text{n} + 2\text{p}5\text{n}$	$2 \times 10^0$ *)
$^{47}\text{V}$	+1/2	32.6 m	$\beta$	$\alpha\text{p} + 3\text{p}2\text{n}$	$7 \times 10^5$

\*) Obtained with 10.4-MeV/u  $^{40}\text{Ca}$  beam.

nuclei  $^{45}\text{Cr}$  and  $^{49}\text{Fe}$  with half-lives as short as 40 ms and 75 ms, respectively, are obtained as mass-separated samples with sufficient intensities for decay spectroscopy. Detailed decay studies should be possible for such very proton rich nuclei in the  $f_{7/2}2p_{5/2}$  shell region.

The study of the  $^{48}\text{Mn}$  decay has been done in collaboration with J.Cerny, R.Kirchner, O.Klepper, A.Plochocki, E.Roeckl, D.Schardt, and B.Sherrill (GSI Darmstadt).

#### References

- 1) J.C.Hardy et al.: "Instrumentation for Heavy Ion Nuclear Research (Nuclear Science Research Conference Series, Vol.7)," ed. by D.Shapira, Harwood Academic Publishers, New York (1985), p.209.
- 2) V.A.Karnaukhov et al.: Nucl. Instr. Meth. 120 (1974) 69.
- 3) S.Ichikawa et al.: The 29th Symposium on Radiochemistry in Funabashi, Oct. 1-3, 1985.
- 4) R.Kirchner and A.Piotrowski: Nucl. Instr. Meth. 153 (1978) 291.
- 5) R.Kirchner et al.: "An Ion Source with Storage Capability for Bunched Beam Release and Controlled Chemical Separation," GSI Preprint 86-2, submitted to Nucl. Instr. Meth. A.
- 6) J.Eberz et al.: Z. Phys. A323 (1986) 119.
- 7) V.T.Koslowsky et al.: "GSI Scientific Rep. 1984," GSI 85-1 (1985), p.90.
- 8) T.Sekine et al.: "GSI Scientific Rep. 1985," (in press).
- 9) R.Kirchner; "GSI Scientific Rep. 1984," GSI 85-1 (1985), p.282.

## 6. NOTE ON THE BACKBENDING

Mitsuo Sakai

Institute for Nuclear Study, University of Tokyo,  
Tokyo, Japan

The backbending phenomenon was discovered in a deformed nucleus  $^{160}_{64}\text{Dy}_{96}$  by A. Johnson et al. in 1971.<sup>1)</sup> This phenomenon was first thought of as evidence for the effect predicted by Mottelson and Valatin,<sup>2)</sup> namely, the collapse of neutron or proton core pairing due to Coriolis antipairing at high angular momentum. In other words, a phase transition occurs at this point and the nucleus changes from superfluid to normal nuclear matter. However, nowadays it is interpreted in terms of a crossing with an aligned band.<sup>3)</sup>

Recently the backbending phenomenon was investigated by many workers and observed not only in collective rotational bands in the rare-earth region but in quasi-rotational bands<sup>4)</sup> in various regions of the periodic table.

In following we will show with a systematic survey that the backbending phenomenon typical in the high-spin members of quasi-rotational and rotational bands can be understood in a unified framework. In view to obtain a comprehensive picture of this exciting phenomenon we studied the following three quantities. The first is concerned with the moment of inertia of the level after the backbending,  $J_0$ , the second with its excitation energy,  $E_0$  and the third with the threshold energy,  $E_c$ .  $J_0$  is defined as the arithmetic mean of the moment of inertia of all the levels after the backbending.  $E_0$  and  $E_c$  are defined as the excitation energies of the first and the last level after and before the backbending, respectively. In order to illustrate how to determine these quantities, we show an example for the case of  $^{108}\text{Gd}$ . Figure 1 presents a diagram of  $2J/\hbar^2$  vs.  $\hbar\omega$ . The levels with  $I = 10, 12, 14$  and  $16$  were considered as the levels after the backbending, so that  $J_0$  was calculated with use of the four moments of inertia of these levels.

According to the definition  $E_0$  and  $E_c$  are the excitation energies of the  $10^+$  and the  $8^+$  level, respectively. The definition of these quantities may not be completely adequate and may introduce some ambiguity. However, our concerns in this paper are to study the gross features of this phenomenon over a wide mass range. We expect that the above procedures are enough to provide significant materials to achieve our aim.

In Table I are listed these quantities for fifty nuclei; they were prepared with use of the recently compiled Table.<sup>5)</sup> (Table I is omitted in this paper.)

In order to study the dependence of  $J_0$  on  $A$ ,  $J_0$  are plotted against  $A$  in a log-log diagram as shown in Fig. 2. It turned out that the experimental points lie around a line of which the slope indicates the functional relation  $J_0 = aA^{1.49}$  near to  $aA^{3/5}$ . This functional form can be expected naturally from both the Mottelson and Valatin's and the band-crossing models because in both cases the moment of inertial approaches that of a rigid rotor,  $J_{\text{rig}}$  which has the following  $A^{5/3}$  dependence,

$$J_{\text{rig}} = 0.502 MA^{5/3} (1 + 3.84 A^{-2/3})(1 + 1/3 \delta), \quad (1)$$

where the nuclear radius is taken as

$$r_0 = 1.12 A^{1/3} \text{ (fm)}. \quad (2)$$

This formula was derived by the following consideration. The moment of inertia of a rigid rotor is described<sup>6)</sup> as

$$J_{\text{rig}} = 2/3 AM \langle r^2 \rangle (1 + 1/3 \delta) \quad (3)$$

and  $\langle r^2 \rangle$  is known<sup>7)</sup>:

$$\langle r^2 \rangle = 3/5 (1.12 A^{1/3})^2 (1 + 3.84 A^{-2/3} + \dots) \quad (4)$$

from the experimental scattering data and the measurements on  $\mu$ -mesic atoms. Introducing Eq. (4) into Eq. (3), we thus obtain Eq. (1) as the first order of approximation. In case of  $\delta = 0.3$  we obtain



$$J_{\text{rig}} = 0.552 MA^{5/3} (1 + 3.84 A^{-2/3}), \quad (5)$$

or

$$2J_{\text{rig}}/\hbar^2 = 0.0264 A^{5/3} (1 + 3.84 A^{-2/3}). \quad (\text{MeV}^{-1}) \quad (6)$$

Consequently it is of interest to see how near  $J_0$  is to  $J_{\text{rig}}$ . For this purpose the ratio of ( $J_0/J_{\text{rig}}$ ) was calculated for each nucleus with use of Eq. (6). They are listed in Table I and plotted in Fig. 3. We notice that, though the experimental points take a slightly decreasing trend with increasing  $A$ , they are roughly constant over all the nuclear regions except Xe, Ba and Os isotopes. The solid line in Fig. 3 was drawn by eye guide which can be expressed by the following equation:

$$R = 0.89 - 0.0004 A. \quad (7)$$

The averaged ratios between  $A = 60$  and  $180$  is  $0.84$ . The fact that  $J_0$  is  $0.84$  times smaller than  $J_{\text{rig}}$  can be explained in terms of the current models which predict that the pairing gap of the core decreases in the first backbending region, but does not fall to zero. For the extreme case, namely, for the case of the complete pairing collapse of neutron or proton core, the nucleus will take the following moment of inertia, respectively:

$$J_0 = J_{\text{rig}} \left\{ 1 - \left( 1 - \frac{J_s}{J_{\text{rig}}} \right) \frac{Z}{A} \right\} \text{ and } J_0 = J_{\text{rig}} \left\{ 1 - \left( 1 - \frac{J_s}{J_{\text{rig}}} \right) \frac{N}{A} \right\}, \quad (8)$$

where  $J_s$  is the moment of inertia of a nucleus in the superstate. If we introduce  $Z/A = 0.4$  and  $J_s/J_{\text{rig}} = 0.4$  into Eq. (8), we obtain  $J_0 = 0.76 J_{\text{rig}}$  and  $0.64 J_{\text{rig}}$ . Taking into account the ambiguity of the coefficient of nuclear radius and the deformation parameter and the values of  $Z/A$  and  $J_s/J_{\text{rig}}$ , we could say that this value is consistent with  $0.84$  deduced from the present systematic studies and may provide a support for the validity of the theoretical interpretation of this phenomenon. It is interesting to note that if we use  $\langle r^2 \rangle = 3/5(1.2 A^{1/3})^2$  instead of Eq. (4) the  $A$  dependence of ratio takes a sharper increasing trend with decreasing  $A$  as demonstrated by a dotted line in fig. 3. It shows the need of the last factor of Eq. (4), being consistent with recent

systematic study of charge density distribution.<sup>8)</sup> Another interesting observation lies in the smallness of  $J_0$  for Xe, Ba and Os isotopes which can be noticed in figs. 2 and 3 where they are presented by black points. As discussed above, this smallness can be understood with the assumption that in these isotopes the pairing collapse first occurs in proton core instead of in neutron core.

The  $E_0$  values are plotted against  $A$  with log-log representation in Fig. 4. We observed that  $E_0$  takes a decreasing trend with increasing  $A$ . As  $E_0$  is related with the appearance of two quasi-particle states, of which the least energy is  $2\Delta = 24 A^{-1/2}(\text{MeV})$ <sup>9)</sup>, we tried to fit it with the same mass dependence. It turned out that the gross feature can be reproduced with the following equation:

$$E_0 = 46.5 A^{-1/2} \text{ (MeV)}, \quad (9)$$

as shown a solid line in Fig. 4.

Finally, in Fig. 5 are plotted the ratios of  $E_C/E_0$ . The points scatter closely around a slightly upward line shown in the figure.

In conclusion, we presented in this paper several systematic trends which show that the current interpretation of the backbending in the deformed region can be applied to that in the other regions and its properties change smoothly over the wide mass range. This fact provides a proof for the validity of the quasi-band concept<sup>4)</sup> which claims a constitution of a new mode in the spherical and vibrational regions which tends smoothly through the transitional region to the collective mode.

#### References

- 1) A. Johnson, H. Ryde and J. Sztarkier, Phys. Lett. 34B (1971) 605
- 2) B. R. Mottelson and J. G. Valatin, Phys. Rev. Lett. 5 (1960) 511
- 3) F. S. Stephens and R. Simon, Nucl. Phys. A183 (1972) 257
- 4) M. Sakai, Nucl. Phys. A104 (1967) 301
- 5) M. Sakai, Quasi-Bands in Even-Even Nuclei, Atomic Data and Nucl. Data Tables 31 (1984) 399
- 6) A. Bohr and B. R. Mottelson, "Nuclear Structure", Vol. II, Chapter 4, (4-104), W. A. Benjamin, INC., Reading, Mass. (1975)
- 7) A. Bohr and B. R. Mottelson, "Nuclear Structure", Vol. I, Chapter 2, (2-71), W. A. Benjamin, INC., Reading, Mass. (1975)
- 8) J. Friedrich and N. Voegler, Nucl. Phys. A373 (1982) 192
- 9) A. Bohr and B. R. Mottelson, "Nuclear Structure", Vol. I, Chapter 2, (2-94), W. A. Benjamin, INC., Reading, Mass. (1975)

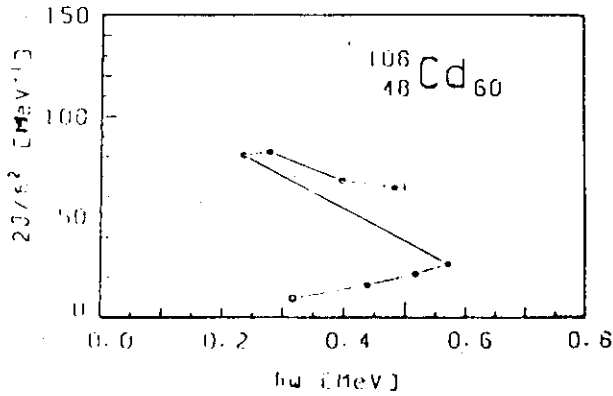


Fig. 1 Backbending in  $^{106}\text{Cd}_{60}$

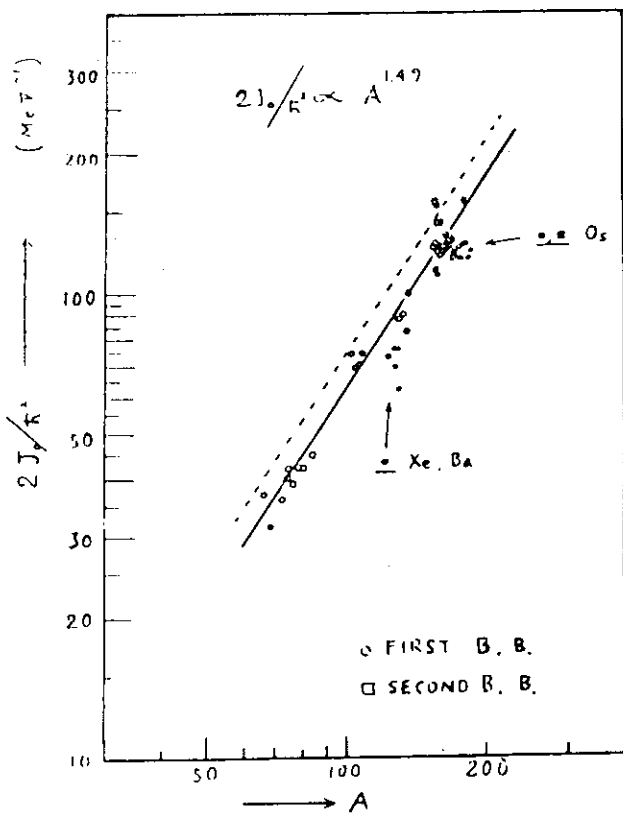


Fig. 2  $J_2$  against  $A$  in a log-log diagram

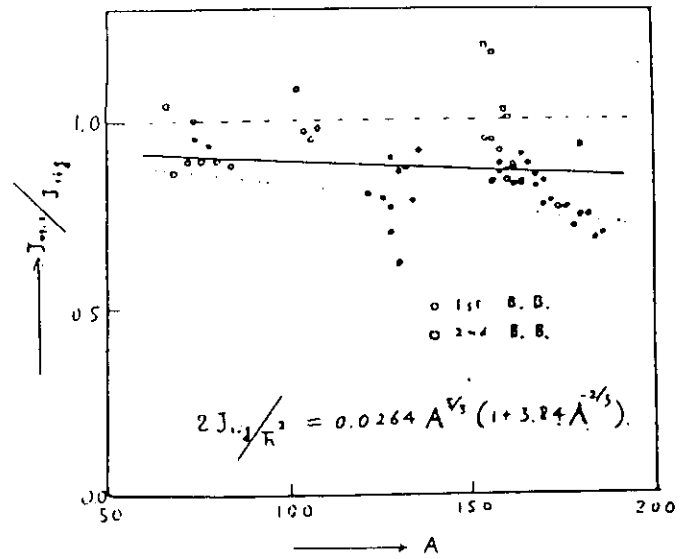


Fig. 3  $J_2/J_1q.$  against  $A$

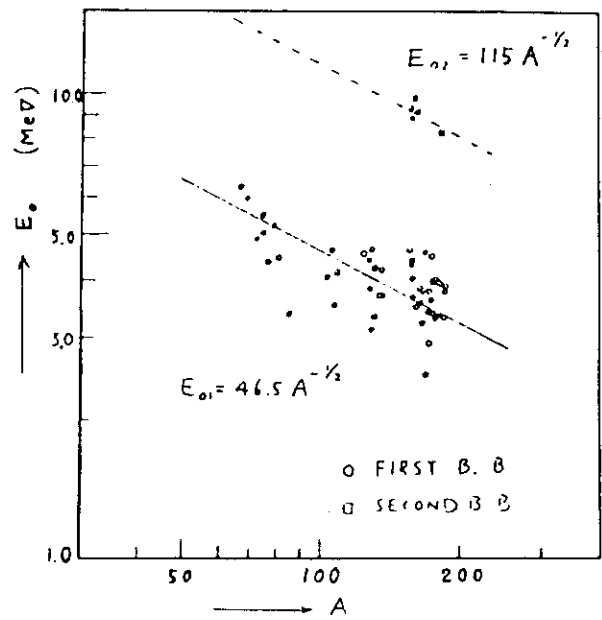


Fig. 4  $E_2$  against with log-log representation

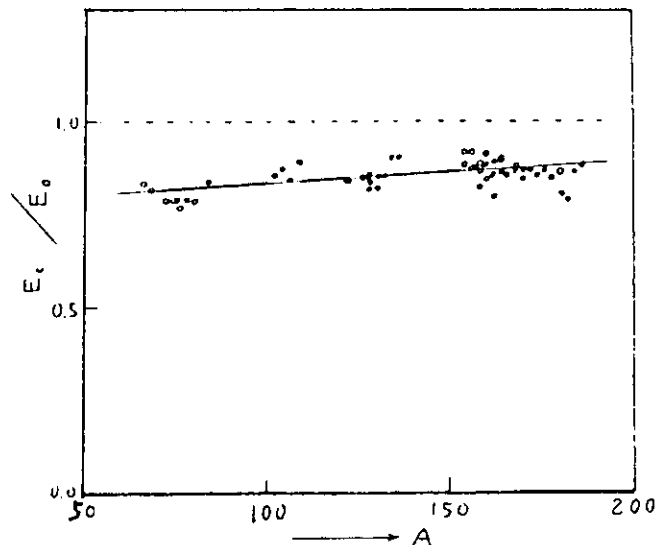


Fig. 5  $E_c/E_s$  plotted as a function of  $A$

## 7. EXISTENCE OF THE ODD-SPIN ROTATION-ALIGNED BAND AND ITS PROPERTIES

Akitsu IKEDA

Department of Physics, Tokyo Institute of Technology, Oh-okayama,  
Meguro, Tokyo

As is well known, the ground-state rotational band (g-band) of deformed even-even nuclides consists only of even-spin levels. This is a consequence of the invariance of the intrinsic state under  $180^\circ$  rotation around an axis perpendicular to the symmetry axis. As the nuclear spin-value increases, the g-band is crossed by a rotation-aligned (RAL) band. Up to the present only even-spin levels have been observed experimentally and identified with the RAL band. The RAL band thus seems to be understood as consisting only of even-spin levels. However there is actually no reason to exclude odd-spin levels out of an RAL band, and we can expect that odd-spin levels exist whose intrinsic structure is similar to that of an even-spin RAL band. We will investigate whether such odd-spin states really exist or not by carrying out numerical calculations in a theoretical model. It is essential for the present purpose to use a model which conserves the angular momentum correctly. In the cranking model it is difficult even to restore the above-mentioned invariance and to remove odd-spins out of a g-band. Thus an extended particle-rotor model will be used. Important ingredients for the description of the rotation-alignment are contained in this model. The model contains a few parameters such as the moment of inertia of the rotor, the pairing gap energy and the quadrupole deformation. These parameters are fixed to values appropriate to nuclides in the  $A \approx 160$  region. As high-j orbits  $h_{11/2}$  is selected, but the obtained results are not restricted only to  $h_{11/2}$  but should apply equally well to other high-j orbits such as  $i_{13/2}$ . The results are briefly summarized as follows:

- (1) The calculated energy spectra are shown in fig. 1 for various values of  $\epsilon_j - \lambda$ . Those levels marked with a circle have a large alignment of angular momentum. We notice that a series of odd-spin levels appears at low excitation energies as we expected. They and the even-spin RAL band do not constitute a regular rotational spectrum, but the odd-spin levels are shifted upwards.
- (2) The calculate E2 transition probabilities along the odd-spin levels are as strong as the ones along the ordinary even-spin RAL band. Thus

these odd-spin levels have a structure common to all of them and can be regarded as a band.

- (3) The odd-spin levels of interest have in common a large alignment of particles in high- $j$  orbits, which is comparable to that of the even-spin RAL band.
- (4) The odd-spin levels and the even-spin RAL band are found to be quite similar in wave-function structure. This makes it possible to regard these two bands as constituting a generalized RAL band.
- (5) Reduced probabilities of the magnetic dipole transition are found to be very characteristic:  $B(M1; I=\text{even} \rightarrow I-1=\text{odd})$  are quite strong, while  $B(M1; I=\text{odd} \rightarrow I-1=\text{even})$  are weak (fig. 2).

The strong  $B(M1)$ 's are of the order of unity when measured in units of  $(g_j - g_R)^2 u_N^2$ . The factor  $(g_j - g_R)^2$  is very much different for the neutron and for the proton when  $j$  is large. Thus these strong M1 transitions contain valuable information for clearly discriminating the rotation alignment of  $i_{13/2}$  neutrons from that of  $h_{11/2}$  protons.

In conclusion the odd-spin RAL levels are predicted in the present paper. Once they are found experimentally, they will provide us with important informations about rotation-alignment. Detailed description of the present study will be published elsewhere.<sup>1)</sup>

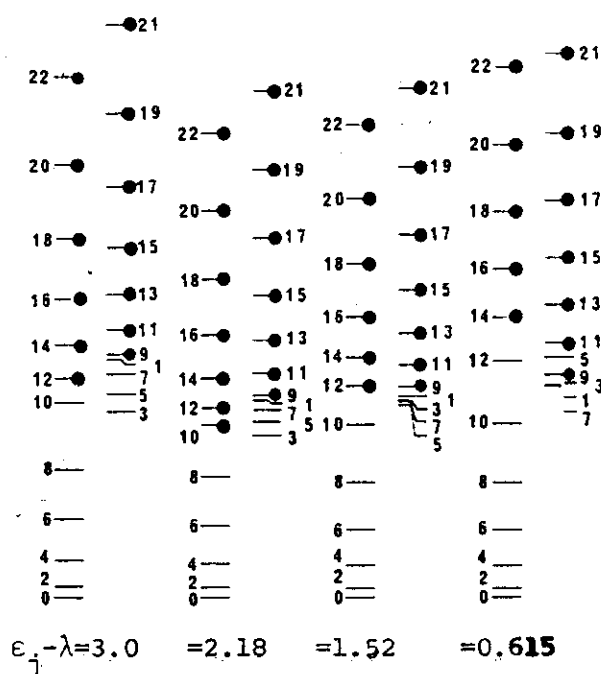


Fig. 1

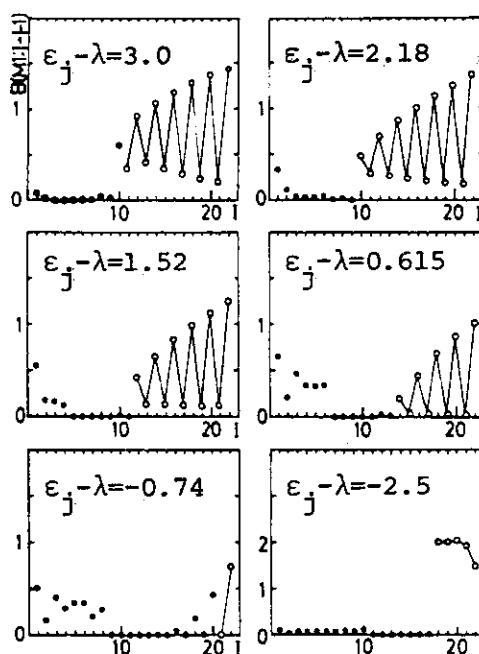


Fig. 2

#### Reference

- 1) A. Ikeda, to be published in Nucl. Phys. (in press)

## 8. Effects of Bandcrossings on M1-Transition Probabilities at High-Spin States

Masayuki Matsuzaki

Department of Physics, Kyoto University

In heavy-ion collisions including Coulomb excitation experiments with the use of tandem accelerators it is possible to measure electro-magnetic transition probabilities at high-spin states of odd-mass nuclei<sup>1)</sup>. These quantities give us valuable informations about nuclear shapes and quasi-particle orbitals. We are interested especially in  $\Delta I=1$  transitions which connect two rotational bands decoupled by the effect of Coriolis interaction. The ratios  $B(M1)/B(E2, \Delta I=2)$  of proton odd nuclei, <sup>155,157</sup>Ho, <sup>159</sup>Tm and <sup>165</sup>Lu were measured up to the rotational frequencies where 3-quasi-particle states became the yrast states, and different aspects were seen before- and after- the bandcrossings<sup>1)</sup>. We study this problem from two points of view; i.e., the signature-averaged magnitudes of these ratios and the signature dependence of them. We analyzed the experimental data by means of the microscopic model which was an extension of the rotating shell model and in which equilibrium deformations were selfconsistently determined<sup>2)</sup>. We found that the  $B(E2, \Delta I=2)$  values did not change drastically after the bandcrossings. Therefore we can ascribe the main origin of the enhancement of these ratios after the bandcrossings to that of the  $B(M1)$  values. The mechanism of this enhancement may be understood as follows.

We adopt the method to construct the transition operators in the intrinsic frame proposed by Marshalek<sup>3)</sup> with some modifications. M1 operators in the laboratory frame can be represented, aside from the factor  $\sqrt{3/4\pi}$ , in the RPA-order in terms of the normal modes  $X_n^\dagger$  and Nambu-Goldstone mode  $\tau^\dagger$  as,

$$\begin{aligned} \mu_{-1}^{(1)} = & \sum_n \left\{ [X_n, \mu_{-1}^{(1)}]_{\text{RPA}} X_n^\dagger - [X_n^\dagger, \mu_{-1}^{(1)}]_{\text{RPA}} X_n \right\} \\ & + [\tau, \mu_{-1}^{(1)}]_{\text{RPA}} \tau^\dagger - [\tau^\dagger, \mu_{-1}^{(1)}]_{\text{RPA}} \tau, \end{aligned} \quad (1)$$

where

$$[\tau, \mu_{-1}^{(1)}]_{\text{RPA}} = \frac{\langle \mu_x \rangle}{\sqrt{\langle J_x \rangle}}, \quad [\tau^\dagger, \mu_{-1}^{(1)}]_{\text{RPA}} = 0. \quad (2)$$

We evaluate the expectation values in the r.h.s. of eq.(2) in the even-even reference configurations. Since  $\mathcal{P}^\dagger$  is the mode corresponding to the collective rotation, we replace it as follows<sup>4)</sup>,

$$\mathcal{P}^\dagger \rightarrow \frac{1}{\sqrt{\langle J_x \rangle}} R_{-1} = \frac{1}{\sqrt{\langle J_x \rangle}} (I_{-1} - J_{-1}), \quad (3)$$

where  $\vec{R}$ ,  $\vec{I}$  and  $\vec{J}$  indicate the angular momenta of the rotor, the total system and the odd-particle, respectively. On the other hand, there is a relation (by definition) between the operators in the laboratory frame and the ones in the intrinsic frame,

$$\mu_{-1} = \sum_{\nu} D_{-1,\nu}' \mu_{\nu}'. \quad (4)$$

We expand the D-functions up to the RPA-order in this expression,

$$\mu_{-1}^{(1)} = \mu_{-1}^{(1)'} + \frac{\langle \mu_x \rangle}{\langle J_x \rangle} I_{-1}^{(1)}. \quad (5)$$

From the expressions (5) and (1) with (2) and (3), we obtain

$$\begin{aligned} \mu_{-1}' &= \mu_{-1}^{(1)'} + \mu_{-1}^{(2)} \\ &= \sum_n \left\{ [X_n, \mu_{-1}^{(1)'}]_{\text{RPA}} X_n^\dagger - [X_n^\dagger, \mu_{-1}^{(1)'}]_{\text{RPA}} X_n \right\} + \frac{\langle \mu_x \rangle}{\langle J_x \rangle} J_{-1} + \mu_{-1}^{(2)}, \quad (6) \end{aligned}$$

where  $\mu_{-1}^{(2)}$  is the "scattering" part which corresponds to the second order in the sense of the boson expansion theory. Since  $\langle \mu_x \rangle / \langle J_x \rangle$  in eq.(6) is the g-factor related to the yrast even-even configuration, we denote it by  $g_{\text{yr}}$ . Thus we get the final expression

$$\begin{aligned} \mu_{-1}' &= \sum_n \left\{ [X_n, \mu_{-1}^{(1)'}]_{\text{RPA}} X_n^\dagger - [X_n^\dagger, \mu_{-1}^{(1)'}]_{\text{RPA}} X_n \right\} \\ &\quad + (g_d - g_{\text{yr}}) L_{-1} + (g_s^{\text{eff}} - g_{\text{yr}}) S_{-1}. \quad (7) \end{aligned}$$

The second and third terms of this expression are of familiar form when the yrast configuration is the g-band (rotor) one. The  $g_{\text{yr}}$  means the g-factor of the  $\{\text{rotor} + (\nu i_{13/2})^2\}$  configuration when the nucleus is in the 3-quasiparticle states because we evaluate the expectation values for the remaining part of nucleus other than the odd-particle. Therefore  $g_{\text{yr}}$  decreases due to the effect of the  $(\nu i_{13/2})^2$  alignment. Consequently the matrix elements of  $\mu_{-1}'$  increase. We evaluate the  $g_{\text{yr}}$  after the bandcrossings by the same method with ref.5), except that we calculate  $g_{2n}$  and the alignments at  $\hbar\omega_{\text{crit}}$  microscopically.

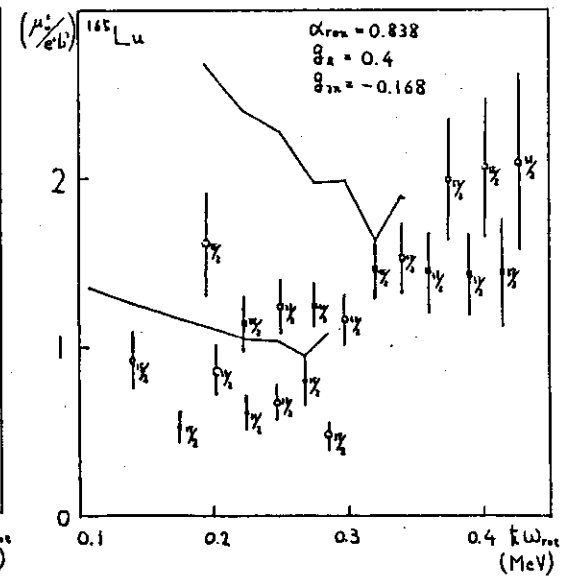
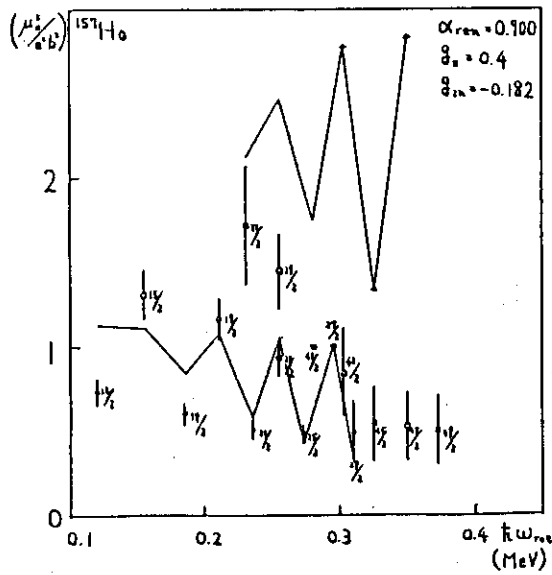
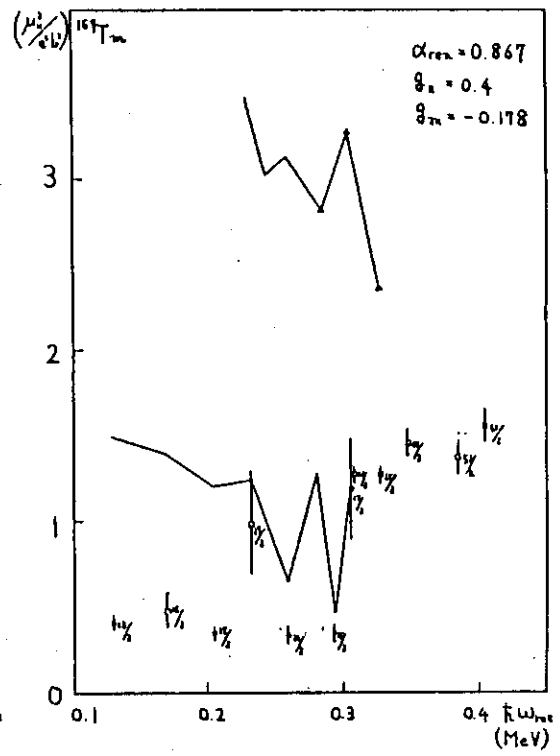
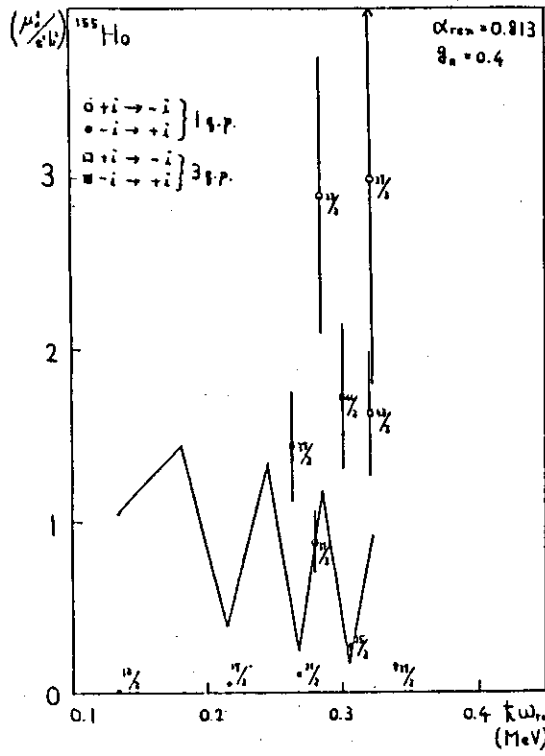
We can qualitatively explain the signature-averaged enhancement of  $B(M1)/B(E2, \Delta I=2)$  by the method described above. We show preliminary results of calculations for  $^{155,157}\text{Ho}$ ,  $^{159}\text{Tm}$  and  $^{165}\text{Lu}$  in the following. In

these calculations, we adopt the "core renormalization factor"  $\alpha_{\text{ren}}$ <sup>6)</sup> which reproduces the average  $Q_0^{(\text{exp})}$  of neighboring even-even nuclei at  $\hbar\omega_{\text{rot}}=0$ , and use average values of signature dependent deformations which are determined in odd-number configurations to take into account a part of tendency of odd-particle to drive nucleus towards triaxial shape<sup>7)</sup>. The resulting  $\gamma$ -values are positive for 1-quasiparticle states of these nuclei ( $^{155}\text{Ho}$  : 5 - 14°,  $^{157}\text{Ho}$  : 2 - 12°,  $^{159}\text{Tm}$  : 3 - 17° and  $^{165}\text{Lu}$  : 1 - 7°) and negative for 3-quasiparticle states except for  $^{165}\text{Lu}$ . ( $^{157}\text{Ho}$  : -3 - -7°,  $^{159}\text{Tm}$  : -4 - -8° and  $^{165}\text{Lu}$  : 6 - 10° --- the oblate isomers correspond to  $\gamma=-60^\circ$  in our convention.) Since neutron pairing-phase transitions occur at  $\hbar\omega_{\text{rot}}=0.302$ , 0.284 and 0.340 MeV for  $^{157}\text{Ho}$ ,  $^{159}\text{Tm}$  and  $^{165}\text{Lu}$  respectively in these calculations for the 3-quasiparticle states, the signature dependence of these ratios is relatively enhanced due to the reduction of  $B(E2, \Delta I=2)$  values associated with the increase of the triaxiality. We have not yet obtained calculated values for the 3-quasiparticle bands of  $^{155}\text{Ho}$  with the use of  $\alpha_{\text{ren}}$ , but the calculation without it gave qualitatively the same feature with the case of  $^{157}\text{Ho}$ . Open triangles in these figures indicate the values calculated without taking into account the particle-vibration couplings.

#### References

- 1) For example,  
 M. Ohshima et al., Nucl. Phys. A436 (1985), 518.  
 G. B. Hagemann et al., Nucl. Phys. A424 (1984), 365.  
 A. J. Larabee et al., Phys. Rev. C29 (1984), 1934.  
 P. Frandsen et al., private communication.
- 2) Y. R. Shimizu and K. Matsuyanagi, Prog. Theor. Phys. 71 (1984), 960.
- 3) E. R. Marshalek, Nucl. Phys. A275 (1977), 416.
- 4) K. Hara and S. Kusuno, Nucl. Phys. A245 (1975), 147.
- 5) I. Hamamoto and B. Mottelson, preprint (Lund-MPh-85/15).
- 6) Y. R. Shimizu and K. Matsuyanagi, Prog. Theor. Phys. 72 (1984), 799.
- 7) S. Frauendorf and F. R. May, Phys. Lett. 125B (1983), 245.





## 9. Multiple Coulomb Excitation of Deformed Odd Nuclei

M.Oshima, S.Kikuchi, S.Ichikawa<sup>\*</sup>, T.Aruga<sup>\*\*</sup>, T.Inamura<sup>\*\*\*</sup>,  
 A.Hashizume<sup>\*\*\*</sup> and H.Kusakari<sup>\*\*\*\*</sup>

Department of Physics, <sup>\*</sup>Department of Chemistry, <sup>\*\*</sup>Department of Fuels  
 and Materials Research, Japan Atomic Energy Research Institute,  
<sup>\*\*\*</sup>The Institute of Physical and Chemical Research, <sup>\*\*\*\*</sup>Faculty of  
 Education, Chiba University.

It is well known that high-j orbits such as  $i_{13/2}$  give rise to a large perturbation of the rotational levels of deformed nuclei. Recently, we have demonstrated such a rotational perturbation effect on M1 and E2 transitions in  $^{167}\text{Er}$  as well as on level energies.<sup>1)</sup> This perturbation effect is dependent on signature  $r$ , a quantum number classifying rotational spectra;  $r$  is defined as  $r = \exp(-i\pi\alpha)$ , where  $I = \alpha \bmod 2$ ,  $I$  being the spin value of the rotational state.<sup>2)</sup> However, more recent investigations on  $^{163}\text{Dy}$ <sup>3)</sup> and  $^{173}\text{Yb}$ <sup>4)</sup> have revealed that the effect is rather weak in these nuclei. The ground states of these nuclei originate from the  $f_{7/2}$  and  $h_{9/2}$  neutron orbits. Thus, this effect is expected to be much dependent on the single-particle orbits which characterize the bands. It would be interesting to study systematically how the single-particle orbits affect the rotational states.

The nucleus  $^{161}\text{Dy}$  is the one whose ground-state rotational band is built on the  $i_{13/2}$  neutron orbit as in the case of  $^{167}\text{Er}$ . Therefore we are interested in whether there is the same signature dependence in  $^{161}\text{Dy}$  as was observed for  $^{167}\text{Er}$ . The ground-state rotational band of  $^{161}\text{Dy}$  has well been established up to  $33/2^+$ ,<sup>5)</sup> and an energy plot such that  $(E(I) - E(I-1))/2I$  vs  $I^2$  shows a remarkable signature dependence as is the case of  $^{167}\text{Er}$ . However, nuclear lifetimes are not available for highly excited states with spins larger than  $9/2$ . In order to measure lifetimes of higher spin states, we are making multiple Coulomb excitation experiment on  $^{161}\text{Dy}$ . Here we present our preliminary results.

The nucleus  $^{161}\text{Dy}$  was multiply Coulomb-excited with a  $^{81}\text{Br}$  beam of 305 MeV from the JAERI tandem accelerator. The target was a self-supporting metallic foil of  $2.5 \text{ mg/cm}^2$  in thickness. Deexcitation  $\gamma$  rays were

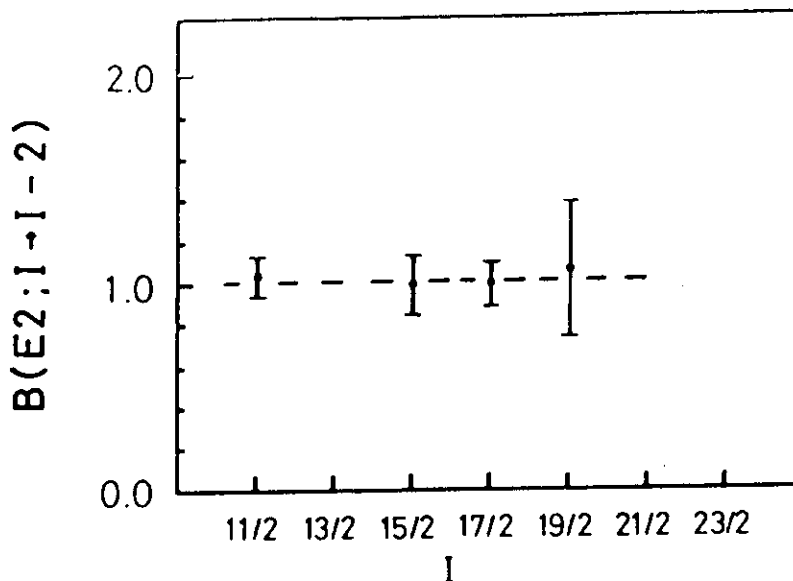


Fig. 1  $B(E2; I-1-2)$  values of  $^{161}\text{Dy}$  in unit of rigid-rotor values ( $Q_0 = 6.4 \text{ b}$ ).

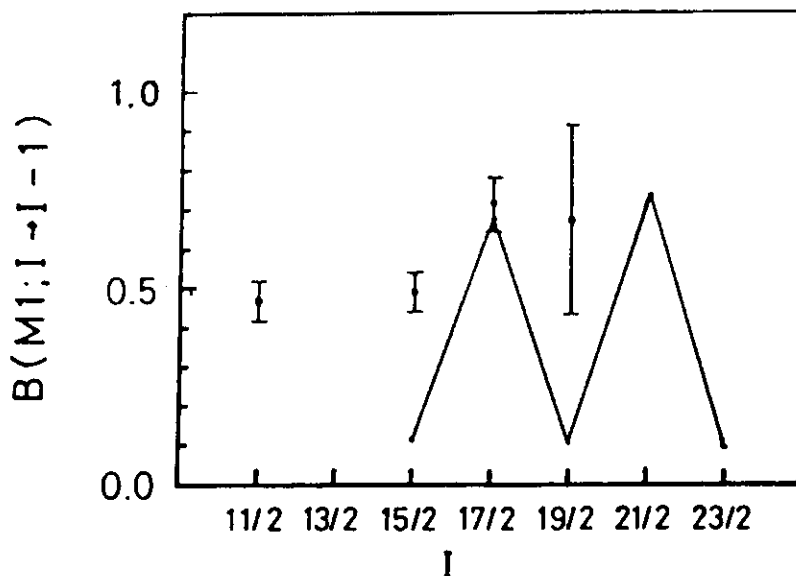


Fig. 2  $B(M1; I-1-1)$  values of  $^{161}\text{Dy}$  in unit of rigid-rotor values which are obtained by adopting  $g_K - g_R = -0.55$ .<sup>7)</sup> The solid line shows an extended particle-rotor model calculation<sup>8)</sup> performed by Hamamoto.

measured with a germanium detector placed at  $45^\circ$  to the beam in coincidence with backward scattered projectiles which were detected at  $\theta = 100^\circ - 150^\circ$  to the beam with a plastic scintillator ( $\Omega = 0.5 \text{ sr}$ ). Nuclear lifetimes were measured by the recoil distance method,<sup>6)</sup> i.e., lifetimes were deduced

from the ratio of the yield  $I_u$  of the unshifted  $\gamma$ -ray peak to the total ( $I_u + I_s$ ) that was plotted as a function of the recoil distance. The quantity  $I_s$  is the yield of the Doppler-shifted peak. Correction for the kinematical effect on the recoil velocity has been made in the analysis. It should be stated that the Doppler-shift attenuation method<sup>1,6)</sup> is inadequate for  $^{161}\text{Dy}$  because  $\gamma$  rays are too narrowly separated to make a lineshape analysis.

We have for the first time measured lifetimes of  $11/2^+$ ,  $15/2^+$ ,  $17/2^+$  and  $19/2^+$  states. (For  $13/2^+$  there are intruder  $\gamma$  rays which make it hard to deduce the true lifetime.) Preliminary results of stopover  $B(M1)$  and crossover  $B(E2)$  values are plotted in Fig. 1 and 2. It is obvious that crossover  $B(E2)$  values are close to the predictions of the Bohr-Mottelson model<sup>7)</sup> as seen in Fig. 1, when an intrinsic quadrupole moment of  $Q_0 = 6.4$  b was adopted. In  $B(M1)$  values, however, there appears to be some signature dependence, which is similar to that found earlier for  $^{167}\text{Er}$ . Qualitatively speaking, this trend is in agreement with extended particle-rotor model calculation<sup>8)</sup> performed by Hamamoto but the oscillation amplitude of experimental values is much smaller than hers. In order to clarify this point, higher spin states will be studied through multiple Coulomb excitation with beams of  $^{58}\text{Ni}$  or  $^{81}\text{Br}$ .

## References

- 1) M. Ohshima, E. Minehara, M. Ishii, T. Inamura, and A. Hashizume, Nucl. Phys. A436 (1985) 518.
- 2) M.J.A. de Voigt, J. Dudek, and Z. Szymanski, Rev. Mod. Phys. 55 (1983) 949.
- 3) M. Ohshima, E. Minehara, S. Kikuchi, T. Inamura, and A. Hashizume, Proc. of Intern. Conf. on Nuclear Physics Vol. 1 (Florence, 1983) 168.
- 4) A. Hashizume et al., priv. comm.
- 5) R.G. Helmer, Nuclear Data Sheets 43 (1984) 1.
- 6) for example, D.B. Fossan and E.K. Warburton, Nuclear Spectroscopy and Reactions, ed. J. Cerny, Part C (Academic Press, New York and London, 1974) p.307.
- 7) A. Bohr and B.R. Mottelson, Nuclear Structure Vol.2 (W.A.Benjamin, inc., 1975).
- 8) I. Hamamoto, Phys. Lett. 106B (1981) 281.

## 10. High Energy Gamma Rays

Emitted from Highly Excited States in the Continuum

T. Murakami<sup>\*</sup>, J. Kasagi<sup>\*</sup>, H. Harada<sup>\*</sup>, H. Tachibanaki<sup>\*</sup>,  
 K. Yoshida<sup>\*</sup>, S. Kubono<sup>\*\*</sup>, M. Yasue<sup>\*\*</sup>, M. H. Tanaka<sup>\*\*</sup>,  
 S. M. Lee<sup>\*\*\*</sup>, M. Ogiwara<sup>\*\*\*</sup>, H. Fujiwara<sup>\*\*\*</sup>, and S. C. Jeong<sup>\*\*\*</sup>

<sup>\*</sup>Department of Physics, Tokyo Institute of Technology, <sup>\*\*</sup>Institute for Nuclear Study, University of Tokyo and <sup>\*\*\*</sup>Institute of Physics and Tandem Accelerator Center, University of Tsukuba

It has been thought that there are two types of transition in unresolved  $\gamma$ -ray spectra. One is statistical transition and the other is stretched quadrupole transition parallel to the yrast line. However, it was discovered by Newton et al.<sup>1)</sup> that there are pronounced shoulders in the spectra of high energy  $\gamma$  rays ( $E_\gamma \geq 10$  MeV) from heavy-ion fusion reactions. Recently, similar results are also reported in other experiments.<sup>2)</sup> These high energy  $\gamma$  rays are interpreted as arising from giant dipole resonance (GDR) built on all excited levels.

It is assumed in this explanation that these high energy  $\gamma$  rays are emitted at early stages, for example, compound nuclei, in competition with the neutron evaporation process.<sup>3)</sup> Therefore, measurements of high energy  $\gamma$  rays open up the possibilities to study the characteristics of highly excited nuclei. Systematic data are very rare at present, and we directed our attention to mass and excitation-energy dependence of high energy  $\gamma$  rays.

Targets of  $^{165}\text{Ho}$ ,  $^{92}\text{Zr}$  and  $^{46}\text{Ti}$  were bombarded with  $\sim 15$  nA of 100 and 78 MeV  $^{16}\text{O}$  beams from the SF cyclotron at INS. High energy  $\gamma$  rays were detected by four 2"  $\phi \times 2$ " BGO scintillators at 30 cm from the targets. Optical fibers are attached to the BGO detectors and light pulses from LED irradiated the scintillators. These light pulses are calibrated to  $\gamma$ -ray energy up to 17 MeV and are used to check stability of the whole system during the experiment. Event rates were 5 kcps at most so that pile up effects can be neglected. Two NE213 scintillators with dimensions of 5"  $\phi \times 3$ " were placed up and down the target and subtended

about 75% of the total solid angle. Events detected by the BGO detectors were recorded in coincidence with  $\gamma$  rays detected by the NE213 detectors with pulse-shape-discriminators. The good timing of the NE213 detectors gave an excellent discrimination against neutrons by time of flight.

Figure 1 shows a  $\gamma$ -ray spectrum obtained in the  $^{165}\text{Ho} + ^{16}\text{O}$  reaction (open circles) at 100 MeV. Yields of  $\gamma$  rays exponentially decrease up to 8 MeV. However, the spectrum rises considerably higher than this exponential curve at energy above 8 MeV. The spectra obtained in other reactions also show similar enhancements. However, the  $\gamma$ -ray energy and strength of the enhancements are different in each reaction.

Analyses are now in progress. Statistical model calculations were carried out using the code "CASCADE".<sup>4)</sup> The calculated results are folded with response functions of the detector. A dashed line in Fig. 1 corresponds to the calculation including GDR with a resonance energy ( $E_g$ ) of 12.2 MeV and a width ( $\Gamma_g$ ) of 5 MeV. A solid line corresponds to the calculation without GDR. The calculation including GDR reproduces the overall feature of the experimental  $\gamma$ -ray spectrum, although strength of the enhancement is smaller than experimental one. Resonance parameters for ground state GDR estimated from the systematics are  $E_g = 14.2$  MeV and  $\Gamma_g = 5$  MeV. Thus the resonance energy employed here is 2 MeV lower than that of

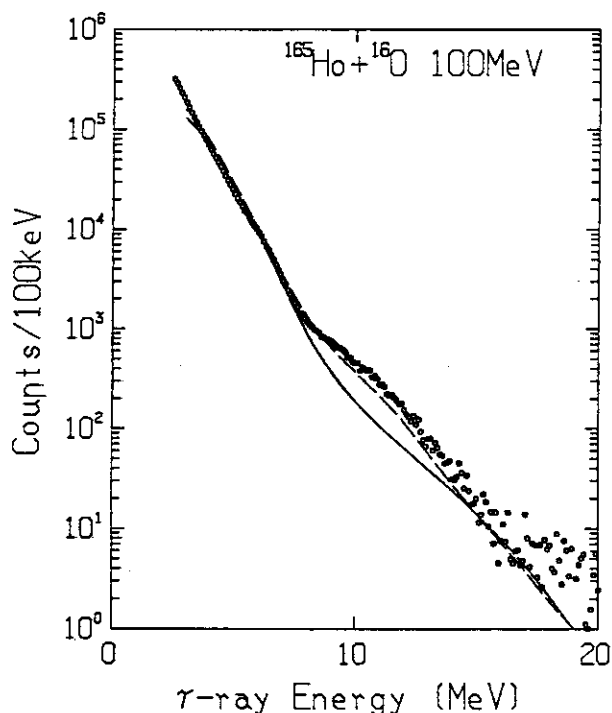


Fig. 1. Experimental and calculated  $\gamma$ -ray spectra for the  $^{165}\text{Ho} + ^{16}\text{O}$  reaction at 100 MeV.

ground state GDR. The calculation using the parameters for ground state GDR gives worse fitting to the data.

In conclusion, the enhancements of high energy  $\gamma$  rays were observed in the  $^{165}\text{Ho}$ ,  $^{92}\text{Zr}$  and  $^{46}\text{Ti}+^{16}\text{O}$  reactions at 100 and 78 MeV. Although the statistical calculation using the code "CASCADE" reproduces the overall feature of the experimental spectrum for the  $^{165}\text{Ho}+^{16}\text{O}$  reaction at 100 MeV, the parameters are different from those of ground state GDR.

#### References

- 1) J. O. Newton et al., Phys. Rev. Lett. 46 (1981) 1383.
- 2) C. A. Gosset et al., Phys. Rev. Lett. 54 (1985) 1486.  
And references therein.
- 3) A. Lazzarini et al., Phys. Rev. Lett. 53 (1984) 1045.
- 4) F. Pulhofer, Nucl. Phys. A280 (1977) 267.

# 11. STUDY OF IN-BEAM GAMMA-RAY SPECTROSCOPY BY $^{58,60}\text{Ni} + ^{28}\text{Si}$ REACTIONS

K. Kuroyanagi, S. Mitarai, Y. Onizuka\*, S. Suematsu,

Y. Ishikawa, K. Heiguchi, B. J. Min, J. Taguchi and H. Tomura

Department of Physics, Kyushu University, Fukuoka, 812 JAPAN and

\*Radiotherapy Center, Kurume Medical University School of Medicine,  
Kurume, 813 JAPAN

## 1. Introduction

Structure of highly excited high-spin states of transitional odd nuclei has been a matter of interest in recent years. As the neutron number goes down toward  $N=40$ , effective quadrupole deformation increases in the  $Z=36$  and  $Z=38$  nuclei. In the case of  $Z=40$ , informations as to location and property of the excited levels of  $^{85}\text{Zr}$  and the lighter odd Zr isotopes are almost lacking. With regard to the  $^{85}\text{Zr}$ , only an isomeric state at 292.2 keV has been reported. In the case of  $^{83}\text{Zr}$ , there has been known only the  $\beta$ -decay of the ground state.

This work presents the in-beam spectroscopic studies of  $^{83}\text{Zr}$  and  $^{85}\text{Zr}$  from the reaction of  $^{58,60}\text{Ni} (^{28}\text{Si}, 2pn)$  as a part of our systematic study of highly excited high-spin states in Zr isotopes.

## 2. Experimental procedure

The  $^{28}\text{Si}$  beam was supplied by the Tandem accelerator in Kyushu University and focussed onto  $2 \text{ mg/cm}^2$   $^{58,60}\text{Ni}$  targets (isotopic enrichment: 98%) electroplated onto a metallic backing of Au (20  $\mu\text{m}$ ). A coaxial intrinsic Ge detector of 16.7% efficiency and 1.9 keV energy resolution at 1.33 MeV ( $^{60}\text{Co}$ ) served to detect gamma rays.

In order to establish level scheme and decay properties of high-spin states in residual nuclei, following measurements of the reaction of  $^{58,60}\text{Ni} + ^{28}\text{Si}$  were performed: (a) gamma ray excitation function gated by neutrons, (b) charged particle-gamma ray coincidence, (c) gamma-gamma coincidence and (d) gamma ray angular distribution gated by neutrons.



Because of complex nature of the gamma rays from the  $^{58,60}\text{Ni} + ^{28}\text{Si}$  reactions involving many residual nuclei, neutron gating method was required so as to clean the spectra and to measure gamma rays with good statistics from the neutron evaporation reaction. Three liquid (NE213) scintillators were used for the neutron detection.

(a) The neutron gated gamma-ray excitation functions for the  $^{58,60}\text{Ni} + ^{28}\text{Si}$  reactions were observed at the 85, 90, 95 and 100 MeV incident energies with the intrinsic Ge detector positioned at  $90^\circ$  to the beam axis (Table 1,2). Neutrons were detected by the two liquid scintillators positioned at  $0^\circ$  to the beam axis and 5 cm from the target. Integrated beam charge accumulated at each energy determined relative normalization. Classification of shape of the excitation function was helpful for preliminary isotropic assignments of the gamma rays.

(b) To distinguish reaction channels, proton and alpha-gamma ray coincidences were carried out at incident energy of 95 MeV. Number of charged particle emitted from a reaction was identified by using a six-segmented Si(Au) detector positioned at  $0^\circ$  to the beam axis and covered the solid angle of 2.76 sr. Intensity ratios of the gamma rays in the 2-fold proton gated and 1-fold proton gated spectra allow clear discrimination between one and two proton emission channels.

(c) Gamma-gamma coincidence experiments were performed at incident energy of 95 MeV by using conventional gamma-gamma techniques with neutron gating. A total of more than  $2.6 \times 10^6$  coincidence events were accumulated. Analysis of gated spectra sorted from the coincident data allowed to identify the gamma ray cascade in the excited levels of  $^{83,85}\text{Zr}$  and to construct the level schemes.

(d) To obtain informations on spins of the levels and gamma ray multipolarities in these nuclei, the gamma ray angular distributions in the  $^{60}\text{Ni} + ^{28}\text{Si}$  reaction were measured in coincidence with neutrons at the 95 MeV beam energy and the angles of  $\theta = 0^\circ, 30^\circ, 45^\circ, 60^\circ$  and  $90^\circ$  to the beam axis. Areas of the gamma peaks were extracted and normalized with respect to the Coulomb excitation line of the target observed at each angles. These intensities were corrected for angular dependent gamma ray absorption and for the difference between beam position on the target and rotation-center of a goniometer of the gamma detector. The corrected intensities were fitted with the function

$$W(\theta) = A_0 + A_2 P_2(\cos\theta) + A_4 P_4(\cos\theta)$$

by least-square analysis, considering the appropriate solid angle correction of the detector. Experimental values of  $A_2/A_0$  and  $A_4/A_0$  coefficients of angular distribution function are given for  $^{85}\text{Zr}$  in Table 2.

### 3. Summary

The level schemes of  $^{83,85}\text{Zr}$  built on the basis of this experiment are shown in Fig.1 and Fig.2, respectively. The two bands in  $^{83}\text{Zr}$  are identified. In the  $^{85}\text{Zr}$  nucleus, a cascade of essentially quadrupole transitions with energies 823.9, 1013.9 and 1191.1 keV is proposed tentatively, and it is considered that the cascade lead to  $9/2^+$  state decayed by 49.3 keV transition to the ground state which is assumed<sup>2)</sup> to have spin and parity of  $7/2^+$ . The positive-parity yrast levels up to  $(21/2^+)$  in  $^{85}\text{Zr}$  are deduced.

### References

- 1) S. D. Negra, H. Gauvin, D. Jacquet, and Y. L. Beyec :Z. Phys. A Atoms-Nuclei 307,305(1982)
- 2) R. Iafigliola and J.K.P. Lee :Phys. Rev. C13,2075(1976)

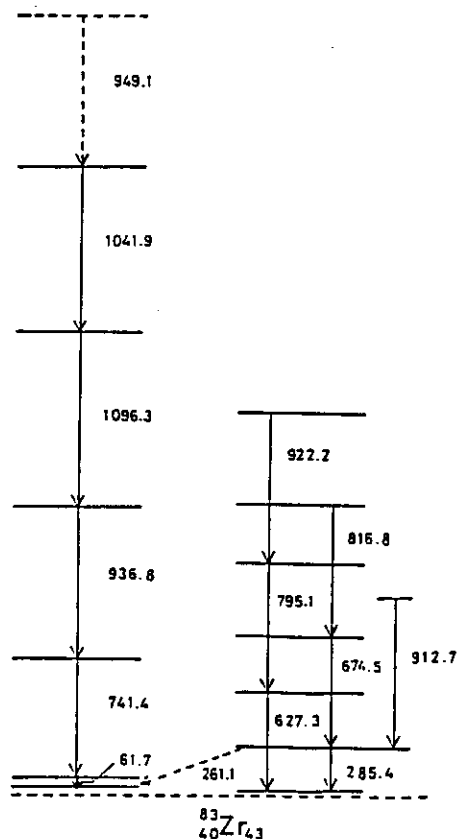


Fig.1

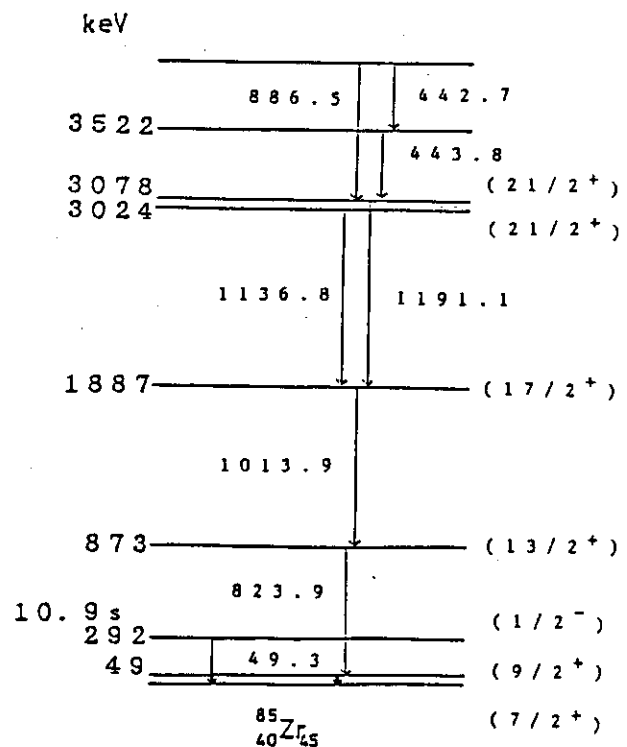
THE LEVEL SCHEME OF  $^{83}\text{Zr}$ .

Fig.2

THE LEVEL SCHEME OF  $^{85}\text{Zr}$ .

Er(KeV)	INTENSITY n-gated (E=95 MeV)	2P/1P RATIO (E=95 MeV)
61.7		0.11 $\pm$ 0.05
129.3	19.7 $\pm$ 1.0	0.12 $\pm$ 0.07
143		
205	7.0 $\pm$ 1.3	
210.2	11.0 $\pm$ 0.9	
238.5	3.3 $\pm$ 0.9	
243.6	14.0 $\pm$ 0.9	
261.1	7.2 $\pm$ 1.0	
285.4	39.1 $\pm$ 1.1	0.23 $\pm$ 0.07
322.6	4.0 $\pm$ 0.9	
372.5	8.6 $\pm$ 1.1	
453.3	13.3 $\pm$ 1.0	
627.3	27.9 $\pm$ 1.8	
630.0	21.1 $\pm$ 1.8	
674.5	36.7 $\pm$ 2.1	
679.8	14.3 $\pm$ 2.0	
741.4	100 $\pm$ 2.4	0.18 $\pm$ 0.05
767.6	13.8 $\pm$ 1.5	
795.0	27.5 $\pm$ 1.6	
816.8	31.2 $\pm$ 1.7	
912.7	23.2 $\pm$ 2.5	
922.3	20.9 $\pm$ 1.7	
936.8	64.4 $\pm$ 2.2	
949.1	5.4 $\pm$ 1.7	
987.2	10.6 $\pm$ 1.8	
1041.9	22.6 $\pm$ 1.8	
1096.3	37.6 $\pm$ 3.0	

Table 1  
SUMMARY OF GAMMA-RAY ENERGIES, RELATIVE INTENSITIES  
AND 2P/1P RATIO FOR  $^{83}\text{Zr}$ .

Er(KeV)	INTENSITY n - gated (E=90 MeV)	2P/1P RATIO (E=95 MeV)	ANGULAR DISTRIBUTION	
			$A_2 / A_0$	$A_4 / A_0$
49.3			-0.067 $\pm$ 0.114	0.504 $\pm$ 0.178
234.4	5.79 $\pm$ 0.64	0.166 $\pm$ 0.022	-0.687 $\pm$ 0.035	-0.210 $\pm$ 0.036
333.8	18.9 $\pm$ 1.1	0.157 $\pm$ 0.016	-0.485 $\pm$ 0.008	0.304 $\pm$ 0.011
429.1	15.5 $\pm$ 1.1	0.148 $\pm$ 0.022	-0.805 $\pm$ 0.019	0.397 $\pm$ 0.027
443.0	13.9 $\pm$ 1.3	0.169 $\pm$ 0.020	-0.637 $\pm$ 0.009	0.542 $\pm$ 0.012
451.1	8.21 $\pm$ 1.07	0.133 $\pm$ 0.023	-0.504 $\pm$ 0.032	0.485 $\pm$ 0.044
547.8	10.9 $\pm$ 1.5	0.142 $\pm$ 0.035	0.608 $\pm$ 0.108	0.439 $\pm$ 0.162
686.7	14.0 $\pm$ 1.5	0.194 $\pm$ 0.041	-0.217 $\pm$ 0.08	0.421 $\pm$ 0.162
806.2	23.1 $\pm$ 1.8	0.153 $\pm$ 0.022	-1.062 $\pm$ 0.028	0.245 $\pm$ 0.035
823.9	100	0.157 $\pm$ 0.011	0.454 $\pm$ 0.003	0.101 $\pm$ 0.004
886.5	7.60 $\pm$ 0.99	0.197 $\pm$ 0.035	-0.738 $\pm$ 0.062	0.192 $\pm$ 0.100
1013.9	100.6 $\pm$ 7.7	0.176 $\pm$ 0.012	0.455 $\pm$ 0.008	0.038 $\pm$ 0.012
1136.8	14.2 $\pm$ 1.8	0.209 $\pm$ 0.038	0.217 $\pm$ 0.072	0.016 $\pm$ 0.102
1190.9	5.18 $\pm$ 2.12	0.164 $\pm$ 0.028	0.445 $\pm$ 0.036	0.006 $\pm$ 0.054
1226.3	7.43 $\pm$ 2.08	0.165 $\pm$ 0.062		

Table 2  
SUMMARY OF GAMMA-RAY ENERGIES, RELATIVE INTENSITIES,  
2P/1P RATIO AND ANGULAR DISTRIBUTION RESULTS FOR  $^{85}\text{Zr}$ .

## 12. Electromagnetic Properties of High-Spin Isomers

Hiroshi Taketani

Department of Applied Physics, Tokyo Institute of  
Technology, Oh-okayama, Meguro, Tokyo 152

The purpose of this research is to investigate quantitatively "Yrast Trap" proposed by Bohr and Mottelson<sup>1)</sup>. At high angular momenta, some nuclei may become oblate and high-spin isomeric states are expected to occur along the yrast line. These yrast isomers occur where the angular momentum is generated by a few nucleons in high-spin orbitals rotating in the same direction around the nuclear symmetry axis. The detailed structures of the isomers are obtained by comparing the measured g-factors with the predictions of the shell-model, since the g-factors depend sensitively on the coupling scheme of individual particles, particularly on the relative contribution of protons and neutrons to the total angular momenta.

We have measured g-factors of some isomers in nuclei of the rare earth and Ra regions. Specifically, the g-factors of isomers in  $^{149}\text{Tb}$ ,  $^{152}\text{Er}$  and  $^{216}\text{Ra}$  were measured by the TIPAD<sup>2)</sup>, those in  $^{216}\text{Ra}$  were measured by the TDPAD<sup>3)</sup>, and those in  $^{212}\text{Ra}$  were measured by the stroboscopic method<sup>4)</sup>.

From the measured g-factors in  $^{216}\text{Ra}$ (TDPAD) and  $^{212}\text{Ra}$ (stroboscopic method), unambiguous shell-model configurations of the isomers in these nuclei have been obtained<sup>3), 4)</sup>.

- 1) A. Bohr and B. Mottelson, Phys. Scr. 10A (1974) 13
- 2) M. Adachi, H. Taketani, T. Kohno, A. Makishima, T. Suzuki, N. Yamada and S. Fukuda, Proc. Int. Symp. on Electromagnetic Properties of Atomic Nuclei (Nov. 1983, Tokyo) p.155
- 3) M. Adachi, T. Kohno, A. Makishima, S. Fukuda, M. Fukuda, M. Taya and H. Taketani, Nucl. Phys. A442 (1985) 361
- 4) T. Kohno, M. Adachi, S. Fukuda, M. Taya, M. Fukuda and H. Taketani, Phys. Rev. C33 (1986) 392

## 13. B(E2) ANOMALY IN GROUND-STATE BANDS IN CE-126 AND -124

Mitsuhiko Ishii<sup>\*</sup>, Masakatsu Hoshi<sup>\*\*</sup>, Tetsuro Ishii<sup>\*</sup> and Masao Ogawa<sup>\*\*</sup>

<sup>\*</sup>Department of Physics, JAERI, Tokai, Ibaraki-ken

<sup>\*\*</sup>Graduate School, Tokyo Institute of Technology, Midori-ku, Yokohama

We have studied nuclei Ce-126 and -124 in-beam spectroscopically through heavy-ion fusion reactions Mo-92(C1-37 or -35, xp yn). The experiments on the gamma-gamma coincidences, the gamma-ray angular distribution and the Doppler effect on gamma-rays have been done with the help of SILICON BOX: a charged-particle multiplicity filter which discriminates between reaction channels by taking count of emitted charged particles [1,2,3].

The level schemes are shown in fig.1 together with the half lifetimes of some excited states. In the following the experimental results are summarized with brief discussions:

- (1) Ce-124 is one of the most well-deformed nuclei that have ever been observed in the very light rare-earth region. The ratio of the excitation energies of the  $4^+$  to the  $2^+$  states  $E(4^+)/E(2^+)$  is 3.14, which is very close to the rotational limit  $10/3$ .
- (2) The ground-state bands backbend in Ce-126 and -124. On the other hand no backbending was found up to the  $12^+$  state in Sm-134 and up to the  $14^+$  state in Nd-132 [2,3].

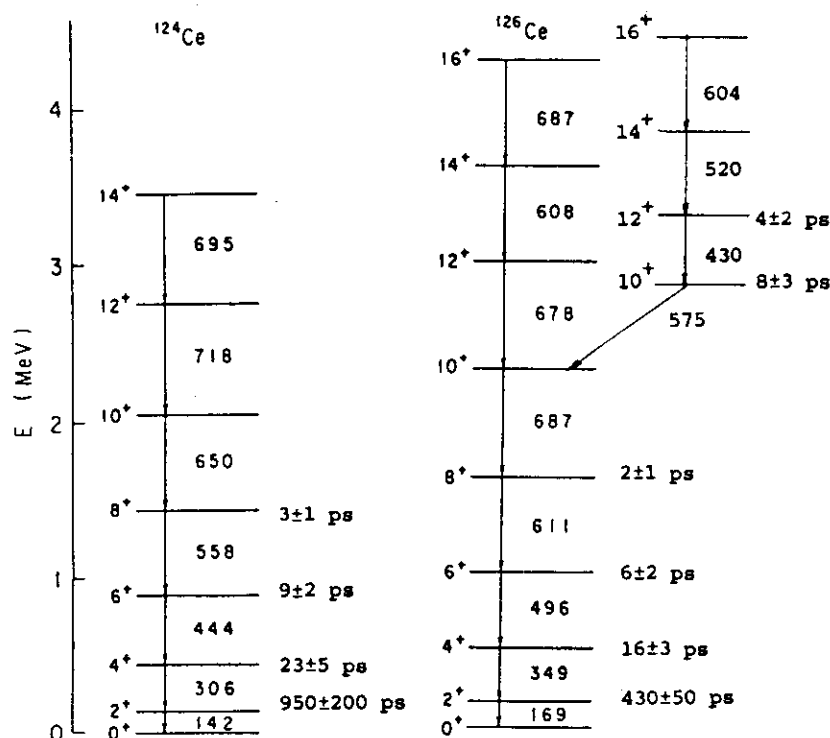


Fig.1. Level schemes of Ce-126 and -124. The half lifetimes are given in units of ps.

- (3) An anomaly in  $B(E2)$  values takes place in the ground-state bands in Ce-126 and -124: the  $4^+$ ,  $6^+$  and  $8^+$  states in Ce-126 have longer lifetimes than ones predicted by the IBM-2 [4], and so do the  $6^+$  and  $8^+$  states in Ce-124. The fact that the experimental  $B(E2;4 \rightarrow 2)$  agrees with the theory in Ce-126 is due to a large deformation. See fig.2.
- (4) A side band was found in Ce-126. In Sm-138 a band of bosons coupled with a two-quasi-particle state  $(h_{11/2})^2; 10^+$  follows the  $8^+$  state in the yrast band [2]. The  $B(E2; 12^+ \rightarrow 10^+)$  and the transition energies seem to indicate that this band is based on two quasi-protons. It is an interesting problem whether the side band in Ce-126 is proton-like or neutron-like. A crucial test for their nature is to measure the  $g$ -factors of their excited states involved.

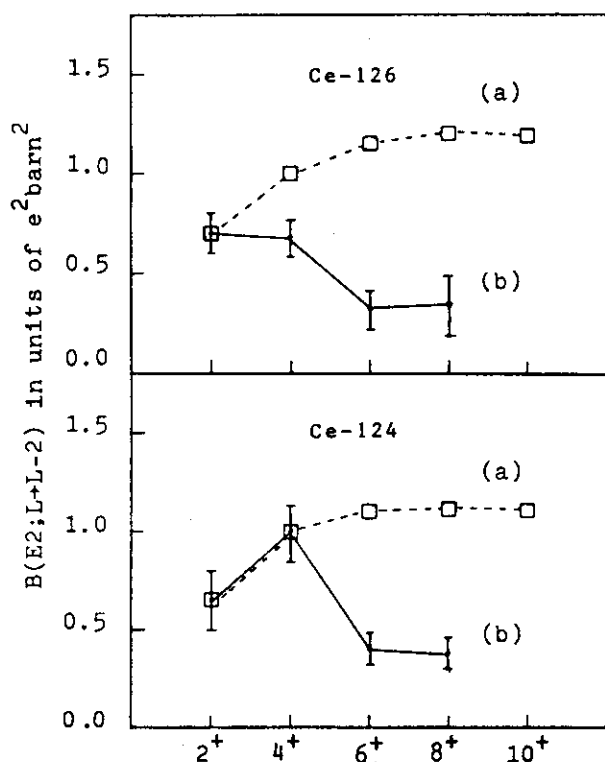


Fig.2. Experimental and theoretical  $B(E2)$  values for the ground-state bands in Ce-126 and -124. (a) the IBM-2 calculation and (b) the present results.

#### References:

- [1] M. Ishii and A. Makishima, ed. K. Harada et al., REPORT OF THE JOINT SEMINOR ON HEAVY-ION NUCLEAR PHYSICS AND CHEMISTRY IN THE ENERGY REGION OF TANDEM ACCELERATORS, JAERI-M 84-085 (1984) p.75.
- [2] A. Makishima, Ph.D Theses of Tokyo Institute of Technology (1985).
- [3] M. Ishii et al., A SILICON BOX: a contribution to the symposium on RECENT ADVANCES IN THE STUDY OF NUCLEI OFF THE LINE OF THE STABILITY held in Chicago in 1985 by American Chemical Society.
- [4] T. Otsuka et al., Phys. Lett. 76B(1978)139 and Report JAERI-M 85-094 (1985).

14. High spin states in  $^{110,112}\text{Sn}$ 

H. Harada\*, J. Kasagi\*, T. Murakami\*, H. Tachibanaki\*,  
K. Yoshida\*, Y. Shibata\*, T. Inamura\*\*, T. Kubo\*\*

\*Department of Physics, Tokyo Institute of Technology,

\*\* RIKEN

The yrast states of even Sn isotopes ( $Z=50$ ) have been well reproduced by neutron two quasiparticle model up to  $9^-$  and  $10^+$  states.<sup>1)</sup> In addition to these quasiparticle states, rotation-like collective bands have been known in  $^{112-118}\text{Sn}$  up to  $12^+$  states.<sup>2)</sup> However, high spin states of the nuclei which show spherical-deformed shape coexistence phenomenon have not yet been investigated. So we have investigated high spin states of  $^{110,112}\text{Sn}$  to study the role of non-collective and collective states in high spin structures.

High spin states of  $^{110}\text{Sn}$  and  $^{112}\text{Sn}$  were excited by the  $^{98,100}\text{Mo}(^{16}\text{O},4n)^{110,112}\text{Sn}$  reactions with beam energies of 72 and 76 MeV. The beam was extracted from 160 cm cyclotron at RIKEN. The targets used were isotopically enriched foils backed with lead. Gamma-gamma coincidence measurements were performed by using five Ge(Li) detectors with BGOACS.<sup>3)</sup> For  $^{110}\text{Sn}$  and  $^{112}\text{Sn}$ ,  $3 \times 10^7$  and  $5 \times 10^7$  events were stored on magnetic tape, respectively. In order to obtain spin-parity assignments, n-gamma angular correlation measurements with neutron multiplicity filter<sup>4)</sup> and life time measurements by recoil distance method were also performed.

The level scheme of  $^{112}\text{Sn}$  deduced from our experimental data is shown in fig.1. Tentative spin-parity assignments are also shown. It was found the  $12^+$  state of the previously known band in  $^{112}\text{Sn}$  whose members are connected with 468 keV( $6^+ \rightarrow 4^+$ ), 663 keV( $8^+ \rightarrow 6^+$ ), 741 keV( $10^+ \rightarrow 8^+$ ), and 864 keV( $12^+ \rightarrow 10^+$ )

transitions to be depopulated by two gamma-rays (799keV and 1057keV). This fact suggests the termination of the band at spin  $12^+$ . Another rotation-like band was assigned up to spin  $20^+$ . The  $12^+$  states of this band is connected with  $10^+$  states of the previously known band through the 744 keV ( $12^+ \rightarrow 10^+$ ) transition. The level scheme of  $^{110}\text{Sn}$  is shown in fig.2. Similar rotation-like band was also observed in  $^{110}\text{Sn}$ . These bands are considered to form yrast states because of large gamma-rays intensities. These bands feed  $10^+$  states at 5.225MeV and 4.678MeV in  $^{110}\text{Sn}$  and  $^{112}\text{Sn}$ , respectively. The  $10^+$  states are considered to have mainly neutron two quasi-particle  $(h11/2)_{10^+}^2$  configurations from energy systematics of  $h11/2$  state. Furthermore, another rotation-like band in  $^{112}\text{Sn}$  was assigned on  $11^-$  state.

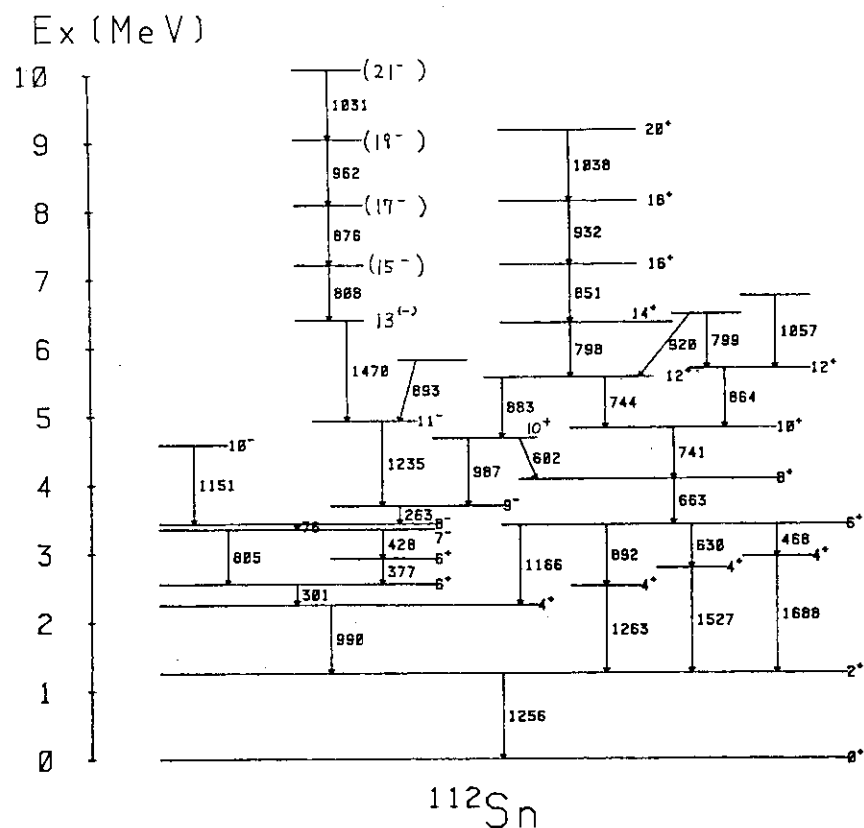
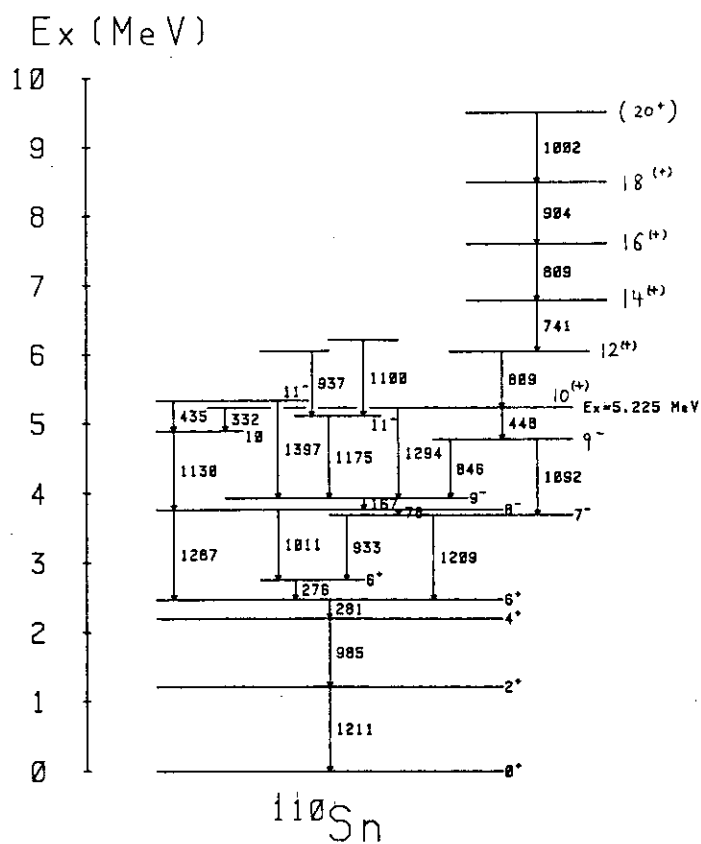
The plots of energy vs  $I(I+1)$  for  $^{110}\text{Sn}$  and  $^{112}\text{Sn}$  were shown in fig.3. From this figure, one can see that the excitation energies of the members ( $J \geq 12$ ) of rotation-like bands in  $^{110}, ^{112}\text{Sn}$  increase proportional to  $I(I+1)$ . The moment of inertia is about  $38 (\hbar^2/\text{MeV})$  for the bands in  $^{110}, ^{112}\text{Sn}$ . This value is almost equal to the calculated one with an assumption of rigid spherical rotor.

In conclusion, yrast states above spin 12 in  $^{110}, ^{112}\text{Sn}$  have been found to be members of the rotation-like bands, although neutron two quasaiparticle states are yrast states below spin 10. The previously known band in  $^{112}\text{Sn}$  was indicated to terminate at spin  $12^+$ . The analysis of spherical states at high spin is in progress.

#### References

- 1) A. Van Poelgeest et al., Nucl. Phys. A346 (1980) 70
- 2) J. Bron et al., Nucl. Phys. A318 (1979) 335
- 3) M. Fukuda et al., RIKEN Accel. Prog. Rep. 18 (1984) 152
- 4) T. Murakami et al., Nucl. Instr. and Meth. A241 (1985) 172



Fig.1 Proposed level scheme of  $^{112}\text{Sn}$ Fig.2 Proposed level scheme of  $^{110}\text{Sn}$

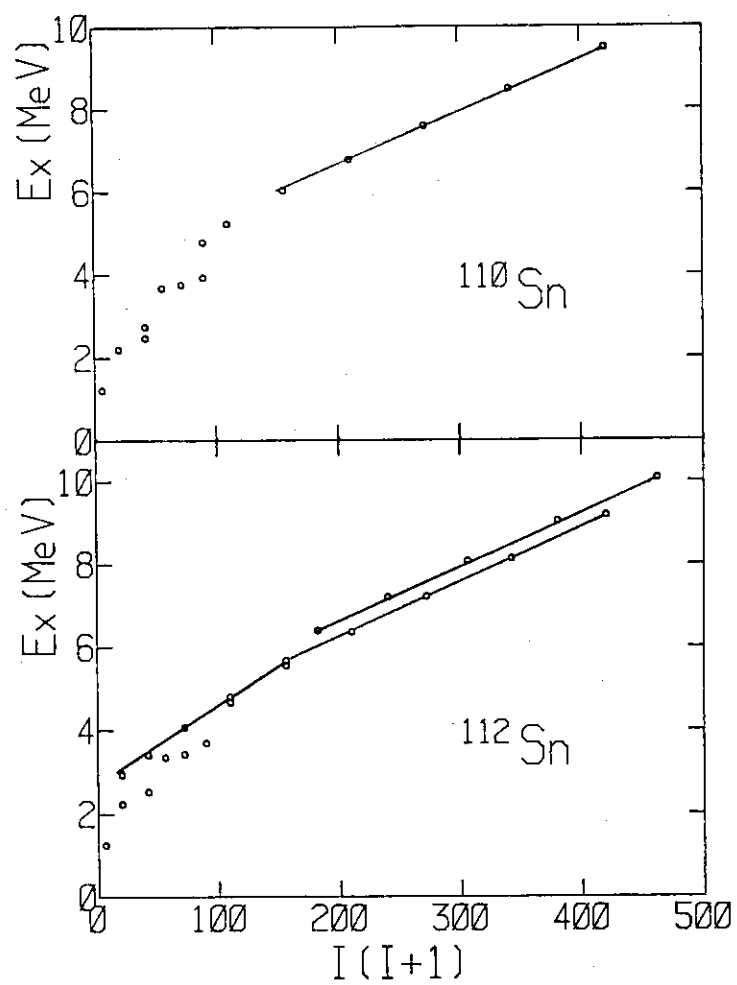


Fig.3 Plot of excitation energy vs  $I(I+1)$  for  $^{110}\text{Sn}$ (upper) and  $^{112}\text{Sn}$ (lower)

## 15. Description of High-Spin States Using the Interacting Boson Model

Nobuaki Yoshida\* and Akito Arima\*\*

\*Department of Information Science, University of Tokyo, \*Department of Physics, University of Tokyo.

Energy levels,  $B(E2)$  values and  $g$ -factors of high-spin states in the Ge isotopes are calculated using the interacting boson model (IBM) coupled with a fermion pair in the  $g_{9/2}$  orbital.<sup>1)</sup>

The model space consists of i) states of bosons only, ii) states with a proton pair in  $g_{9/2}$ , and iii) states with a neutron pair in  $g_{9/2}$ . The hamiltonian consists of a boson hamiltonian  $H^B$ , a hamiltonian of fermions in  $g_{9/2}$   $H^F$ , and a boson-fermion interaction  $V^{BF}$ . The boson hamiltonian  $H^B$  is the one fitted to low-lying levels. The fermion hamiltonian  $H^F$  consists of single-particle energy and the delta interaction. The single-fermion energies are taken as being close to the quasiparticle energies. The delta interaction has the intensity which corresponds to the lowering of a zero-coupled pair by 2 MeV. As the interaction between bosons and fermions  $V^{BF}$ , we assume the quadrupole-quadrupole interaction. The quadrupole operator includes the terms which allow a boson to change into a pair of fermions. We determine the parameters in  $V^{BF}$  for  $^{68}\text{Ge}$  so that the locations and  $B(E2)$  values of the three  $8^+$  states are reproduced. The variation of these parameters with mass number is estimated considering the microscopic theory of the IBM by Scholten who took into account the mass number dependence by using the  $u$  and  $v$  factors of the BCS theory.<sup>2)</sup> For the calculation of  $B(E2)$  values, we determine them from experimental  $B(E2; 2_1^+ \rightarrow 0_g^+)$  values for each isotope assuming same effective charges for proton and neutron bosons. We assume fermion effective charges to be  $1.5e$  for protons and  $0.5e$  for neutrons. In the  $M1$  operator, we assume  $1 \mu_N$  and  $0$  for the  $g$ -factors of proton bosons and neutron bosons, respectively. As for the  $g$ -factors of the fermions in  $g_{9/2}$ , we assume  $1.16 \mu_N$  and  $-0.21 \mu_N$  for protons and neutrons, respectively, which are determined from  $g$ -factors of  $9/2^+$  levels of neighboring nuclei.

The calculated and observed energy levels and  $B(E2)$  values are compared in Fig. 1, which shows good overall agreement. The excitation energy of the first  $8^+$  state is lowered as the mass number increases. This

trend is reproduced by the calculation. In  $^{66}\text{Ge}$ , the IBM calculation reproduces the odd-even staggering like 2, (3, 4), (5, 6), ... observed in the  $\gamma$ -band. In  $^{68}\text{Ge}$ , the calculation suggests that the first and the second  $8^+$  states are both mixed states of the zero- and the two-neutron-mixed states. By this mixing, we are able to reproduce appreciable amount of E2 transitions to the first  $6^+$  state from both of the first and the second  $8^+$  states, although they are still smaller than the observed values. In  $^{70}\text{Ge}$  and  $^{72}\text{Ge}$ , the lowest  $8^+$  states from calculation seem to be of neutron nature, and the second boson states. The above arguments about the nature of these bands, however, are all dependent largely on the choice of parameters. As is well known, one of the experimental methods to determine the character of bands is the measurement of g-factors. By the calculation, the states with an aligned  $g_{9/2}$  proton pair are expected to have positive g-factors, and the states with an aligned  $g_{9/2}$  neutron pair to have negative g-factors.

## References

- 1) N. Yoshida and A. Arima: Phys. Lett. 164B (1985) 231.
- 2) O. Scholten: Ph. D. Thesis, Univ. of Groningen (1980).

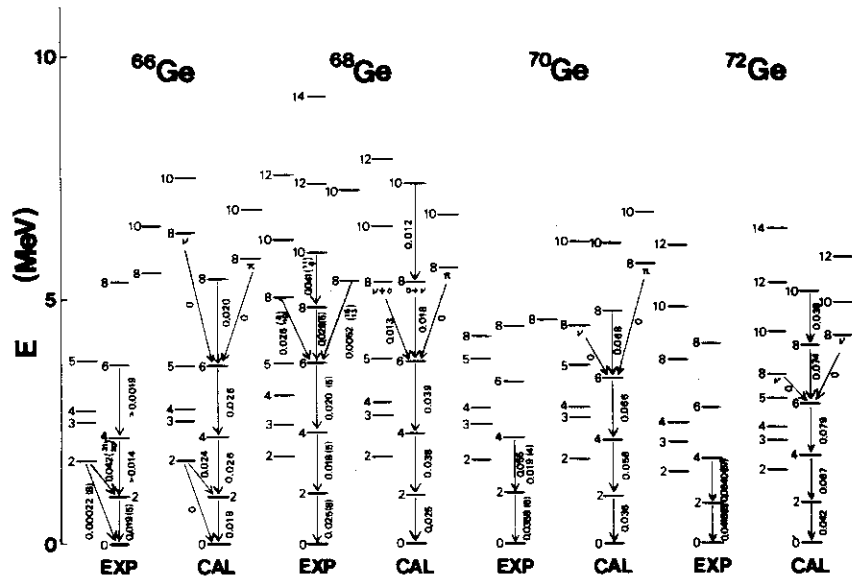


Fig. 1. Energy levels and B(E2) values in  $^{66,68,70,72}\text{Ge}$ . Bands with  $\pi$  and  $\nu$  in the figure are proton- and neutron-aligned bands, respectively. B(E2) values are given in units of  $e^2 b^2$ .

## 16. Heavy-Ion Spectroscopy viewed from the IBM

Takaharu Otsuka

Department of physics, Japan Atomic Energy Research Institute,  
Tokai, Ibaraki, 319-11, Japan

I will briefly talk about the following three subjects;

- (1) Isovector  $K=0^+$  band in deformed nuclei,
- (2) M1 transition from the isovector  $2^+$  state,
- (3) Exchange Interaction in the IBFM and the Anomalous Coupling State.

The first subject has been discussed in Ref. 1. I therefore mention only that the isovector or mixed-symmetry  $K=0^+$  band in deformed nuclei shows large deformation comparable with the ground band. This subject can be studied experimentally from this point of view.

The second subject is discussed in Ref. 2. The isovector or mixed-symmetry state can decay to the first  $2^+$  state via a relatively strong M1 transition. An experimental attempt is desired along this direction.

The third subject has been developed quite recently. The shell model origin of the exchange term in the Interacting Boson-Fermion Hamiltonian is studied first. The quadrupole pairing interaction is shown to be the dominant source in and near spherical regions of the periodic table. The strength of this term calculated for the  $0g_{9/2}$  orbit turns out to be in good agreement with the phenomenological fit. Fig. 1 shows experimental and IBFM spectra of  $^{93}\text{Tc}$ . The exchange effect on the E2 transition is also clarified. The relative  $B(E2)$  values from various excited states to the ground state are shown in Fig. 2, where large exchange effects are noticed. See details in Ref. 3.

### References

- 1) O. Scholten, K. Heyde, P. Van Isacker, and T. Otsuka, Phys. Rev. **C32**, 1729 (1985).
- 2) T. Otsuka and J.N. Ginocchio, Phys. Rev. Lett. **54**, 777 (1985).
- 3) T. Otsuka, N. Yoshida, P. Van Isacker, A. Arima, and O. Scholten, to be published in Phys. Rev. Lett. (1986).

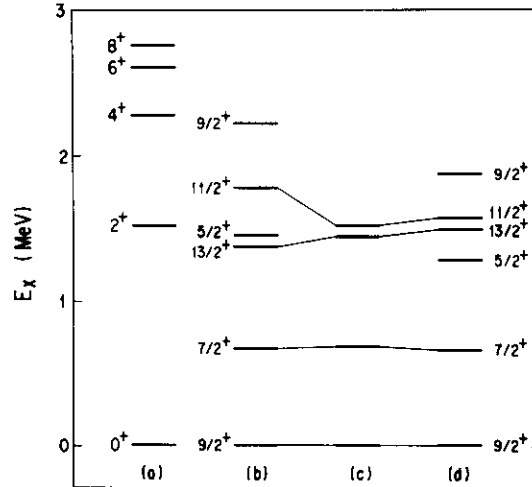


Fig. 1. Experimental energy levels of proton  $g_{9/2}$  states in (a)  $^{92}_{42}\text{Mo}$  and (c)  $^{93}_{43}\text{Tc}$ , compared with IBFM calculations, (b) and (d), where Hamiltonians are derived from shell model Hamiltonians determined empirically from the experimental levels of  $^{92}\text{Mo}$ . All terms in the shell model Hamiltonian are included in (d), while only monopole and quadrupole pairing interactions are taken in (b).

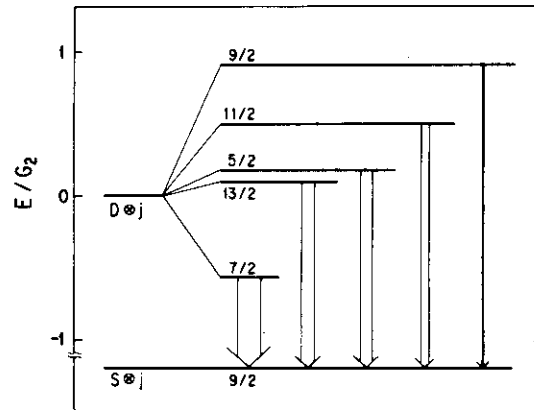


Fig. 2. Energy splitting of  $[Dj;J]$  three-nucleon states in  $j=9/2$  due to the quadrupole pairing interaction in the unit of its strength ( $G_2$ ). The total angular momentum  $J$  is indicated at each split level. Relative  $B(E2)$ 's to the ground state are shown by widths of arrows.

17. Highly excited and high-spin states in  $^{16}\text{O}$   
populated by ( $^{12}\text{C}, ^8\text{Be}_{g.s.}$ ) reaction

Kasuaki Ekuni, Susumu Shimoura, Kiyohiko Takimoto, Atsushi Sakaguchi,  
Nobuo Ikeda, Akihiko Nakamura and Mamoru Fukada\*

Department of Physics, Kyoto University, \*Department of Education,  
Kyoto Pharmaceutical University.

The  $\alpha$ -cluster states which have  $\alpha$  particle like configuration have been well investigated theoretically and experimentally. In  $^{16}\text{O}$ , it is well known that the members of the  $K=0^+$  band whose band head is the 2nd  $0^+$  (Ex. energy 6.05 MeV) and the  $K=0^-$  band whose band head is the 1st  $1^-$  (Ex. energy 9.63 MeV) are well definite  $\alpha$ -cluster states and large  $\alpha$  reduced width. But the members of each band have been well identified only up to  $6^+$  (Ex. energy 16.3 MeV) and  $7^-$  (Ex. energy 20.9 MeV). So, it is necessary to understand the band structure more completely that the members with higher spin and excitation energy would be investigated.

To probe such  $\alpha$ -cluster states,  $\alpha$ -nucleus scattering and  $\alpha$ -transfer reactions [ ( $^6\text{Li}, d$ ), ( $^7\text{Li}, t$ ), ( $^{12}\text{C}, ^8\text{Be}$ ) and ( $^{16}\text{O}, ^{12}\text{C}$ ) etc.] have been investigated. We chose ( $^{12}\text{C}, ^8\text{Be}$ ) reaction, since in  $\alpha$ -nucleus scattering it would be disadvantage that due to low relative angular momentums contributing to the reaction, low spin states could overlap with the high-spin states, and in various  $\alpha$ -transfer reaction, ( $^{12}\text{C}, ^8\text{Be}$ ) reaction has advantage that (i) the particles except the residual nucleus have spin 0, (ii)  $^8\text{Be}$  decay to two  $\alpha$ 's with relative energy 92 keV. From (i), detecting  $^8\text{Be}$  at  $0^\circ$  and the coincident  $\alpha$  particles from the residual

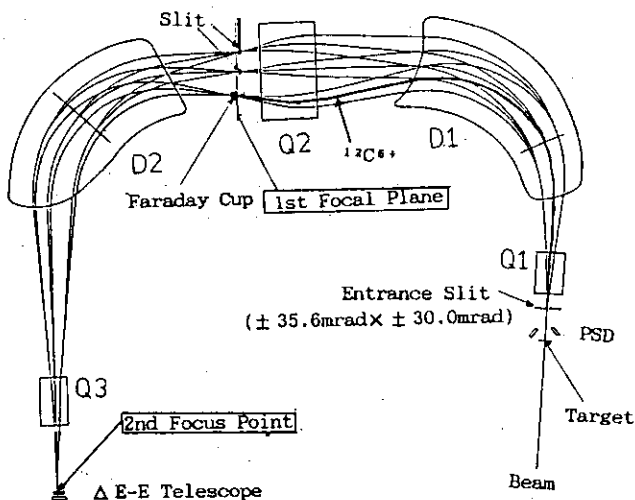


FIG. 1. Experimental Apparatus for  $^8\text{Be}$  detection using DUMAS and coincidence detectors (two PSD's). The two  $\alpha$ 's from  $^8\text{Be}$  are refocused by DUMAS and detected by  $\Delta E-E$  counter telescope.

nucleus can give the unique spin parity assignment. From (ii), by selective detecting coincident two  $\alpha$ 's from  $^8\text{Be}$  with relatively low relative energy, only the ground state can be observed.

The experiment was performed at RCNP using  $^{12}\text{C}^{4+}$  (energy = 160 MeV) beam from AVF cyclotron. The target was natural C foil (thickness  $200 \mu\text{g}/\text{cm}^2$ ). The spectrograph 'DUMAS' was used for  $^8\text{Be}$  detection (fig. 1). 'DUMAS' has the large angular acceptance and the 2nd focal point which has the achromatical focusing. The two  $\alpha$ 's from  $^8\text{Be}_{g.s.}$  were refocused at the 2nd focal point with high efficiency and were detected by  $\Delta E$ -E counter telescope. Beam was stopped at the low momentum side on the 1st focal plane which has the momentum dispersive focusing. Due to the limit of the acceptance of momentum of the 1st focal plane, two  $\alpha$ 's from the excited states of  $^8\text{Be}$  can not be refocused at the 2nd focus point. Unfortunately  $^{15}\text{N}^{5+}$  (energy = 198 MeV) was mixed to the main beam with the mixing ratio about 1/1000. To prevent  $^{15}\text{N}$  beams, the narrow slit was placed on the 1st focal plane. The  $\alpha$  decayed from  $^{16}\text{O}^*$  was detected by two PSD (position sensitive solid state detector) placed in the scattering chamber. The particle identification for these counter was performed kinematically.

In fig. 2, the singles spectrum of  $^8\text{Be}_{g.s.}$  and the effective solid angle for  $^8\text{Be}$  are shown. The  $6^+$  and  $7^-$  states are clearly observed on little background. The background mainly comes from the process of breakup of  $^{12}\text{C}(3^-_1(9.64), 4^+_1(14.08)$  and continuum) populated by inelastic scattering. Due to

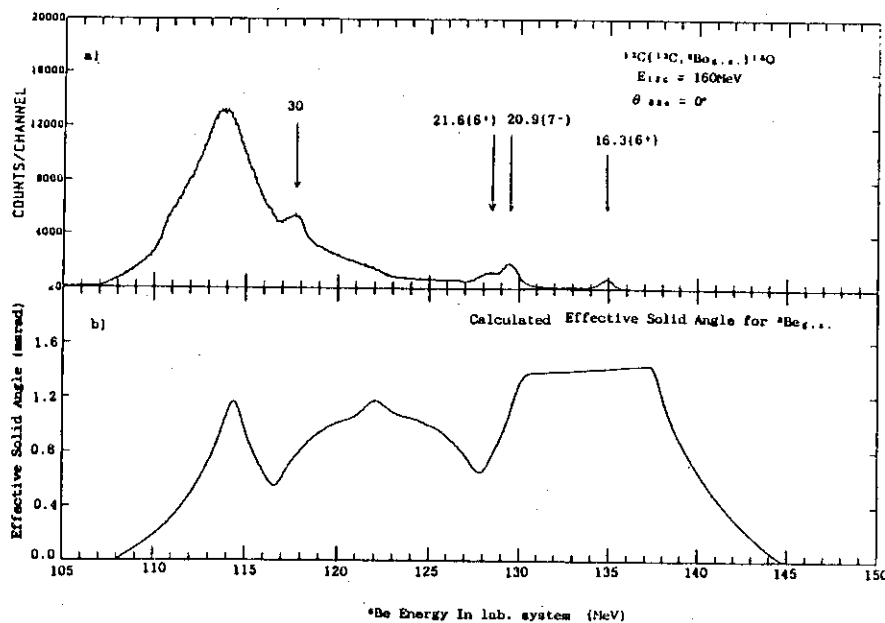


FIG. 2. a)  $^8\text{Be}$  energy spectrum measured at  $\theta = 0^\circ$  for  $^{12}\text{C}(^{12}\text{C}, ^8\text{Be}_{g.s.})^{16}\text{O}$  reaction at a bombarding energy of 160 MeV. b) Calculated effective solid angle for  $^8\text{Be}_{g.s.}$ . The two hollow places at about 117 MeV and 128 MeV are due to the narrow slit by which  $^{15}\text{N}$  beam was stopped.



the high incident energy, these background overlap the populated states (excitation energy below about 25MeV) by  $\alpha$ -transfer process less than those in lower incident energy<sup>1)</sup>. The gross structure at  ${}^8\text{Be}$  energy 113MeV is almost due to breakup process and effective solid angle. Besides these states, a state with little higher excitation energy than  $7^-$  and a state with excitation energy 30MeV are populated. This state has been recently observed in  ${}^{12}\text{C}({}^{12}\text{C}, \alpha {}^{12}\text{C}) {}^8\text{Be}_{g.s.}$  [ $E_{12\text{C}} = 120 \text{ MeV}$ ]<sup>2)</sup>.

The angular correlation function  $W(\theta ({}^8\text{Be}) = 0^\circ, \theta_{\text{decay}})$  for the  $7^-$  and the state with little higher excitation energy are shown in fig. 3. The distribution for  $7^-$  is well fit to  $|P_7|^2$ . And that of the state with little higher excitation energy is also fit to  $|P_6|^2$  and this state could be assigned to  $6^+$  and the excitation energy is 21.6MeV<sup>3)</sup>. Compared with coincident spectrums for  $\alpha_1$ , it could be observed that this state has the width decaying to  $\alpha - {}^{12}\text{C}_{2+}$  which is comparable with the width to  $\alpha - {}^{12}\text{C}_{g.s.}$ . The correlation function for the state with excitation energy 30 MeV has oscillatory structure, but the background from breakup of continuum states overlap. This state may be  $9^-$  state which is the member of  $K=0^-$  band. The detailed analysis is now being progressed. This oscillatory structure mainly comes from  $L=9$  component.

#### Reference

- 1) S.J. Sanders, L.M. Martz and P.D. Parker: Phys. Rev. C20 (1979) 1743
- 2) W.D.M. Rae et al.: Phys. Lett. 156B (1985) 167
- 3) F. Ajzenberg-Selove: Nucl. Phys. A375 (1982) 1

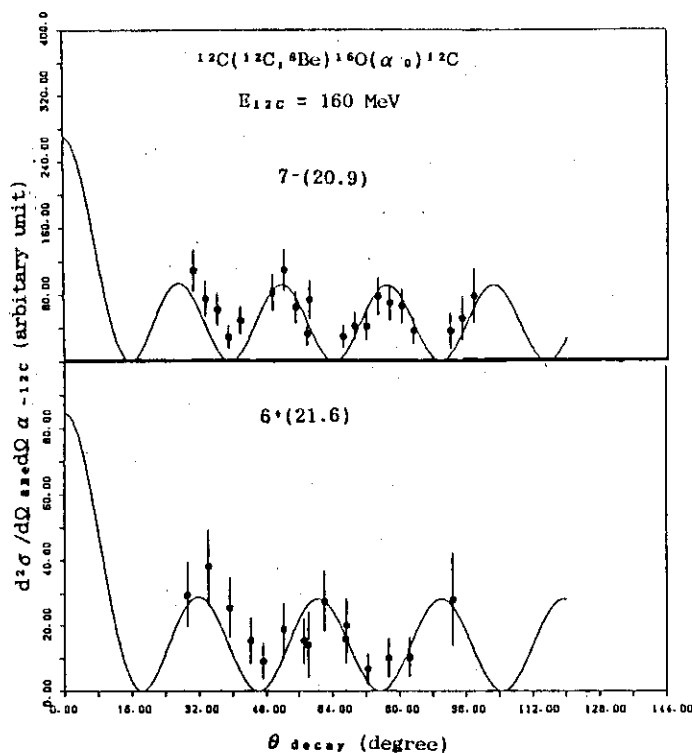


FIG. 3. Measured angular correlations for the  ${}^{12}\text{C}({}^{12}\text{C}, {}^8\text{Be}) {}^{16}\text{O}(\alpha_0) {}^{12}\text{C}$  reaction. The solid curves show  $|P_j(\theta_{\text{decay}})|^2$  angular distributions which are the best fit to the data.

## 18. Giant Resonances in Hot and Rotating Nuclei

Kosai Tanabe\* and Kazuko Sugawara-Tanabe\*\*

\*Department of Physics, Saitama University, Urawa, Saitama 338 and

\*\*Department of Physics, University of Tokyo, Tokyo 113.

Great progress has been made in theoretical understanding of the evolution of nuclear structure along the yrast line and also in the yrast region in terms of the microscopic mean field theory — the cranked Hartree-Fock-Bogoliubov (HFB) theory and the random phase approximation (RPA) [for reviews, see Ref. 1)]. To describe the highly excited states far above the yrast region, one of the available theoretical methods is the statistical extension of the cranked HFB theory with temperature  $T$ . Then, the cranked thermal HFB (THFB) equation takes into account both the excitation (temperature) effect due to many particle-many hole configurations and the Coriolis effect due to rapid rotation, and its self-consistent solution provides single particle levels as the basis for statistical ensemble. Detailed account of the THFB formalism and the application to realistic case have been presented in the series of our work<sup>1, 2)</sup>. Recent measurements have assessed the Lorentzian peaks in the spectra of high energy  $\gamma$ -rays emitted from highly excited compound nuclei formed by heavy ion collisions<sup>3-5)</sup>. Such structures in the  $\gamma$ -ray spectra can be interpreted as the collective vibrational states like giant dipole resonances (GDR) built on the ensemble of nuclear levels at high temperature and high spin.

Our purpose here is to propose a self-consistent formalism of the thermal RPA (TRPA) and also to investigate whether the numerical analysis based on the TRPA equation can reproduce some characteristics of the GDR found in experiments. In existing formalism the RPA equation is derived from the *linearization ansatz*,  $[H', Q^\dagger] = \hbar\omega Q^\dagger$ , where  $H'$  is the cranked Hamiltonian, whose form is determined after solving the THFB equation. However, such RPA equation fails to take into account some important correlations arising from the thermal effect. Therefore, we variate the model grand potential

$$\begin{aligned}\Delta F &= \text{Tr}(\tilde{W}H') - kT \text{Tr}(\tilde{W} \ln \tilde{W}) - F \\ &= i\langle [H', R] \rangle + \frac{1}{2} \langle [R, [H', R]] \rangle\end{aligned}\quad (1)$$

with respect to the variational parameters  $X_{\mu\nu}$ ,  $Y_{\mu\nu}$ ,  $Z_{\mu\nu}$  and their complex conjugates introduced through the unitary transformation for the density matrix, i. e.

$$W \longrightarrow \tilde{W} = \exp(iR) W \exp(iR) \quad (2)$$

with

$$R \equiv Q^\dagger + Q, \quad Q^\dagger = \sum_{\mu > \nu} (X_{\mu\nu} \alpha_\mu^\dagger \alpha_\nu^\dagger - Y_{\mu\nu} \alpha_\nu \alpha_\mu) + \sum_{\mu\nu} Z_{\mu\nu} \alpha_\mu^\dagger \alpha_\nu, \quad (3)$$

where the bracket  $\langle \rangle$  stands for the ensemble average. Minimizing  $\Delta F$  under the constraints

$$\langle [Q, Q^\dagger] \rangle = 1, \quad \langle [Q, [H', Q]] \rangle = \langle [Q^\dagger, [H', Q^\dagger]] \rangle = 0, \quad (4)$$

we obtain the TRPA equation<sup>6)</sup>

$$\Omega \mathbf{M} \mathbf{X}^{(n)} = \hbar \omega_n \mathbf{X}^{(n)}, \quad (5)$$

where the TRPA matrix  $\Omega$  and the metric matrix  $\mathbf{M}$  are given by

$$\Omega_{\mu\nu, \rho\sigma} \equiv \begin{pmatrix} A_{\mu\nu\rho\sigma} & B_{\mu\nu\rho\sigma} & C_{\mu\nu\rho\sigma} \\ B_{\mu\nu\rho\sigma}^* & A_{\mu\nu\rho\sigma}^* & -C_{\mu\nu\rho\sigma}^* \\ C_{\rho\sigma\mu\nu}^* & -C_{\rho\sigma\mu\nu} & \mathcal{D}_{\mu\nu\rho\sigma} \end{pmatrix} \quad (6)$$

especially with

$$C_{\mu\nu\rho\sigma} \equiv 6 (H_{31})_{\mu\nu\rho\sigma} \quad (7)$$

and

$$\mathbf{M}_{\mu\nu} = \begin{pmatrix} 1 - f_\mu - f_\nu & 0 & 0 \\ 0 & -(1 - f_\mu - f_\nu) & 0 \\ 0 & 0 & f_\nu - f_\mu \end{pmatrix}. \quad (8)$$

Since no reference is made to the operator relation like the linearization ansatz in our derivation of the TRPA equation, the inclusion of  $Z$  term in (3) does not cause any theoretical inconsistency. Because of this term the correlations caused by  $H_{31}$  term in the Hamiltonian is taken into account as shown in (7). The second order variation of  $F$  with respect to the THFB variational parameters gives the stability condition for the THFB solution. It generalizes the stability condition for the HFB equation at  $T = 0$ , and only the submatrix of the whole stability matrix corresponds to the TRPA matrix<sup>6)</sup>.

The thermal extension of the absolute square of the transition matrix for the emission or the absorption of  $\gamma$ -ray of energy  $\hbar\omega$  is given by

$$\begin{aligned} M(\omega l \mu; a) &= \frac{1}{2\pi} \int_{-\infty}^{\infty} dt \exp(i\omega t) \sum_{ijkl} \langle c_i^\dagger(t) c_j(t) c_k^\dagger(0) c_l(0) \rangle \\ &\quad \times \Omega_{ij}^\dagger(\omega l \mu; a) \Omega_{kl}(\omega l \mu; a) \\ &\equiv \sum_{n>0} \{ A(\omega_n l \mu; a) \delta(\omega - \omega_n) + B(\omega_n l \mu; a) \delta(\omega + \omega_n) \}, \end{aligned} \quad (9)$$

where  $\Omega_{ij}(\omega l \mu; a)$  is the single-particle electromagnetic  $l$ -pole transition matrix element specified by the polarization component  $\mu$  and the character

of electric or magnetic a. Only the first term  $A(\omega_n \ell \mu; a)$ , which we call the *dynamical strength function*, contributes to the emission of  $\gamma$ -ray ( $\omega > 0$ ) from the decay of compound states, and the second term  $B(-\omega_n \ell \mu; a)$  corresponding to the absorption of  $\gamma$ -ray ( $\omega < 0$ ) does not contribute to the physical process. In contrast to the dynamical strength function, the *kinematical strength function* which appears in the thermal extension of the energy weighted sum rule formula is given by

$$\begin{aligned} M'(\omega \ell \mu; a) &= \frac{1}{2\pi} \int_{-\infty}^{\infty} dt \exp(i\omega t) \sum_{ijkl} \langle [c_i^\dagger(t) c_j(t), c_k^\dagger(0) c_l(0)] \rangle \\ &\quad \times \Omega_{ij}^\dagger(\omega \ell \mu; a) \Omega_{kl}(\omega \ell \mu; a) \\ &\equiv \sum_{n>0} \{A(\omega \ell \mu; a) - B(\omega \ell \mu; a)\} \{\delta(\omega - \omega_n) - \delta(\omega + \omega_n)\}. \end{aligned} \quad (10)$$

This expression contains the contribution from the B term even for  $\omega > 0$ , which corresponds to the transition from one of the high-lying ensemble levels to the compound level, and should be excluded from the physical process. By this reason we propose the dynamical strength function as the quantity comparable with the experimental decay process at high temperature. It is also noticed that the cancellation takes place in the combination (A-B) appearing in (10), so that the thermal (temperature) effect is less pronounced in the kinematical strength function.

We performed numerical analysis for the GDR in Er isotopes at high temperature and high spin based on the TRPA equation (5) and the strength function (9)<sup>7)</sup>. Our Hamiltonian includes the dipole-dipole interaction  $\chi_D/2 \vec{D}^\dagger \cdot \vec{D}$  in addition to the pairing-plus-quadrupole interaction. We adopted large single-particle space covering almost three major shells. The result shows slow decrease of resonance energy with increasing temperature and with increasing angular momentum, and increase of spreading width of the GDR with increasing temperature. These agree with the observed trends. The dynamical strength function shows more marked temperature dependences of resonance energy and width than the kinematical one does. Splitting of resonance peak is also well reproduced by the calculation. In Figs. 1 and 2 our results are compared with experimental  $\gamma$ -ray spectra for  $^{166}\text{Er}$ . Since the size of our single-particle space is still not large enough to reproduce the absolute strength, theoretical curves (solid lines) are properly normalised. In both diagrams we observe that resonance energies and widths are in quite good agreement with experiments. Theory assumes the temperature  $kT = 1.5$  MeV and the angular momenta  $12^+$  (Fig. 1) and  $26^+$  (Fig. 2). Corresponding excitation energies are both 38 MeV above the  $\gamma$ -ray line, and the energies of the initial compound states measured from

the ground states become 53.8 MeV for the  $12^+$  state [Cf. the experimental energy 49.2 MeV for  $I \approx 15^{(4)}$ ] and 58.5 MeV for the  $26^+$  state [Cf. the experimental energy 61.5 MeV for  $I \approx 22^{(5)}$ ]. The theoretical deformation parameters  $\delta = 0.34$  for the  $12^+$  state and 0.30 for the  $26^+$  state are very close to the experimental value 0.3 in both cases.

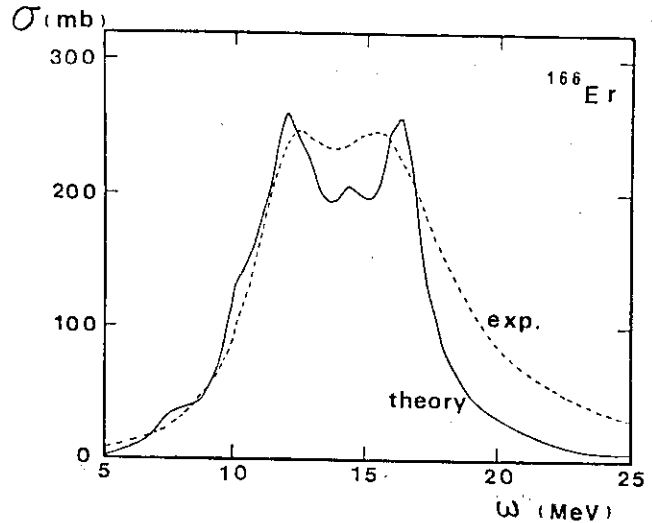


Fig. 1

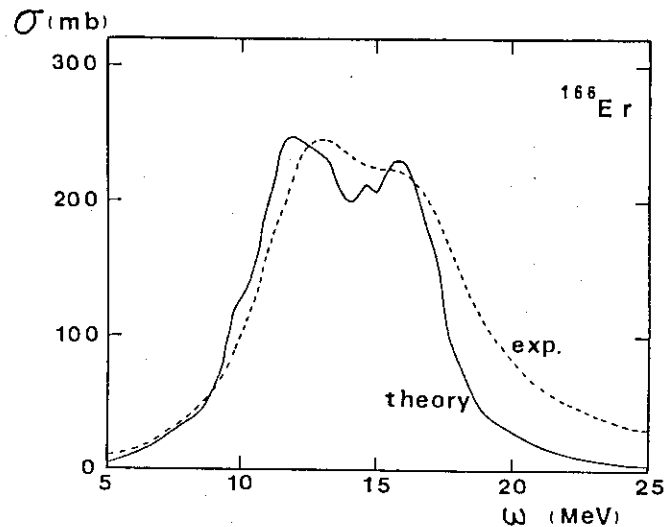


Fig. 2

## References:

- 1) K. Tanabe, Mean field theory of nuclear collective motion, J. Saitama Univ., Liberal Arts 2(1983) 43.
- 2) K. Tanabe and K. Sugawara-Tanabe, Phys. Lett. 97B(1980) 337; Nucl. Phys. A390(1982) 385.
- 3) J. O. Newton et al., Phys. Rev. Lett. 46(1981) 1383.
- 4) C. A. Gossett et al., Phys. Rev. Lett. 54(1985) 1486.
- 5) J. J. Gaardhøje et al., Phys. Rev. Lett. 53(1984) 148.
- 6) K. Tanabe and K. Sugawara-Tanabe, The thermal linear response theory for the dissipative high spin quantum states (preprint, 1985); On the variational derivation of the thermal RPA equation (preprint, 1986).
- 7) K. Sugawara-Tanabe and K. Tanabe, Thermal and rotational effect on giant dipole resonances in rotating nuclei at high temperature (preprint, 1985).

## 19. Hartree-Fock Approach for Thermal Nuclei

H. Sagawa

Department of Physics, University of Tokyo  
Bunkyo, Hongo 7-3-1, Tokyo 113

Recently, intermediate energy heavy-ion collisions have been studied intensively, looking for phase transitions under various thermodynamical circumstances. There are many open questions concerning the reaction mechanism during the early stages of the time evolution of hot nuclei which should be answered by studies based on microscopic theory. One of the fundamental questions is whether the global thermalization is really established or not in the initial stage of the head-on collision. Even if the nuclear matter is thermalized, the next question is whether this equilibrium lasts long enough to establish a first-order phase transition. Under these circumstances, it is not clear that the critical point behavior of the phase transition can be observed in thermalized nuclei created by heavy-ion collisions[1]. However, in this note, I assume that the presence of two phases may be taken for granted.

The dynamical constraints on the system might be determined by physical situation as follows. First, the nucleus might expand or shrink depending on the initial conditions. This situation might be taken care of by a constraint  $\lambda_1 r^2$  (or equivalently  $\lambda_1 \rho(r)$ ). Secondly, the nucleus might move collectively in a certain direction due to its expansion. We need another constraint for this collective motion, namely,  $\lambda_2 (\vec{p} \cdot \vec{r} + \vec{r} \cdot \vec{p})$ . Thus, our model hamiltonian is described as a double-constrained one,

$$h'' = h_{H-F} - \lambda_1 r^2 - \lambda_2 (\vec{p} \cdot \vec{r} + \vec{r} \cdot \vec{p}) \quad (1)$$

where  $\lambda_1$  and  $\lambda_2$  are independent lagrange multipliers.

Hereafter I will summarize briefly some formulas of H-F theory at finite temperature. The variational method should apply for the thermodynamical potential

$$\Omega = \langle H \rangle - T \cdot S - \mu \langle N \rangle \quad (2)$$

with respect to the grand canonical partition function instead of the hamiltonian  $\langle H \rangle$ , as in the zero-temperature case. The H-F equations to be solved are obtained as

$$h(\rho)\phi_i = \varepsilon_i \phi_i$$

$$\sum_i f_i(T) = \sum_i \{1 + \exp[(\varepsilon_i - \mu)/T]\}^{-1} = A \quad (3)$$

where the density  $\rho$  is defined by

$$\rho(r, T) = \text{Tr}\{D\rho\} = \sum_i f_i(T) \phi_i^* \phi_i$$

I will now introduce the dynamical equations of motion based on the quantum mechanical commutators. The time dependences of the expectation values of the operators  $r^2$  and  $\vec{p} \cdot \vec{r}$  are given by

$$\begin{aligned} i d\langle r^2 \rangle / dt &= \langle [r^2, h_{H-F}] \rangle = \langle [r^2, h'' + \lambda_1 r^2 + \lambda_2 \vec{p} \cdot \vec{r}] \rangle \\ i d\langle \vec{p} \cdot \vec{r} \rangle / dt &= \langle [\vec{p} \cdot \vec{r}, h_{H-F}] \rangle = \langle [\vec{p} \cdot \vec{r}, h'' + \lambda_1 r^2 + \lambda_2 \vec{p} \cdot \vec{r}] \rangle \end{aligned} \quad (4)$$

where the expectation value implies

$$\begin{aligned} \langle O \rangle &= \sum_i f_i(T) \langle \phi_i | O | \phi_i \rangle \\ h'' \phi_i(\lambda_1, \lambda_2) &= \varepsilon_i(\lambda_1, \lambda_2) \phi_i(\lambda_1, \lambda_2) \end{aligned} \quad (5)$$

Since the wave function  $\phi_i$  is an eigenstate of the constrained hamiltonian, we can rewrite eq.(4) as simple dynamical equations

$$d\langle r^2 \rangle / dt = 2\lambda_2 \langle r^2 \rangle, \quad d\langle \vec{p} \cdot \vec{r} \rangle / dt = -2\lambda_1 \langle r^2 \rangle \quad (6)$$

These coupled equations describe essentially a harmonic vibration mode (the breathing mode as the first sound) in the small amplitude limit. Some numerical results are given in ref.(2).

- References 1) C. B. Chitwood et al., Phys. Lett. 131B (1983) 289  
2) H. Sagawa and G. F. Bertsch, Phys. Lett. 155B (1985) 11

## 20. Self-Consistent Transport Coefficients for Damped Large Scale Collective Motion

S.Yamaji\*, H.Hofmann\*\* and R.Samhammer\*\*

\*Cyclotron Laboratory, the Institute of Physical and Chemical Research

\*\*Physik-Department der Technischen Universität München

The microscopic expressions for the transport coefficients are derived by exploiting locally generalized RPA-type dispersion relation<sup>1)</sup>. These expressions are evaluated for the dynamics of fission around and behind the barrier by applying the two-center shell model<sup>2)</sup> at finite temperature and a finite coupling of one particle-one hole excitations to more complicated configurations<sup>3)</sup>.

The actual microscopic computations were performed for the symmetric fission of a  $^{212}\text{Po}$  nucleus. From the parametrization of mean field introduced in Ref.2, the center-separation  $z_0$  is taken as a macroscopic variable. The other variables such as neck-parameter  $\varepsilon$  and deformation  $\delta$  are fixed to be 0.35 and 0.0, respectively. We calculated the potential energy  $V(z_0)$  as the sum of Coulomb energy and nuclear macroscopic energy<sup>4)</sup>.

In Fig.1, the solution  $\Omega_0$  of the RPA-type dispersion relation is shown as a function of  $z_0$ . The phonon energy  $\Omega_0$  is strongly related to the stiffness coefficient  $C(0) = \partial^2 V(z_0) / \partial z_0^2$  shown by the dashed curve in Fig.2. The effect of phonon on the coefficients of inertia  $M$ , friction  $\gamma$  and stiffness  $C$  was studied. It was found to be very important behind the barrier where the phonon frequency is appreciably large. For example, in Fig.2, the stiffness coefficient  $C(\Omega_0)$  with the phonon effect shown by the solid curve is compared with  $C(0)$  without the phonon effect shown by the dashed curve.



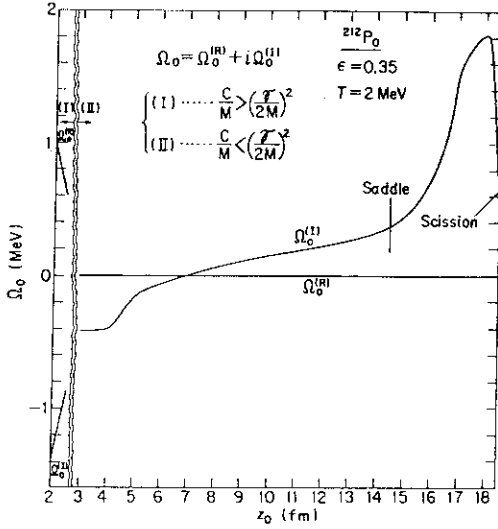


Fig.1

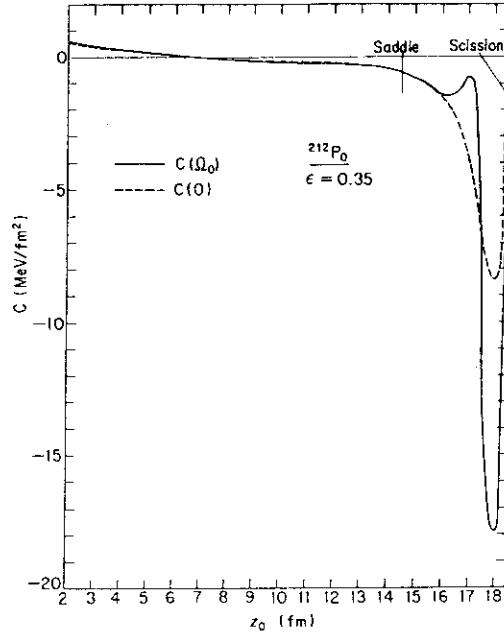


Fig.2

The dimensionless quantity  $q = \gamma / 2\sqrt{M|C|}$  is shown as a function of  $z_0$  in Fig.3. This parameter  $q$  governs the solution of transport equation and is often used as a phenomenological parameter<sup>5)</sup>. The analysis of the mean saddle-to-scission time, mean kinetic energy at scission and variance in kinetic energy for 120 MeV  $\alpha + {}^{209}\text{Bi} \rightarrow {}^{213}\text{At} \rightarrow$  fission yields the empirical value of order 1 for the parameter  $q$ <sup>5)</sup>. The solid and dashed lines correspond to the local frequency  $\Omega_0$  determined by RPA-dispersion relation and the Markoff-limit  $\Omega_0 \rightarrow 0$ <sup>6)</sup>, respectively.

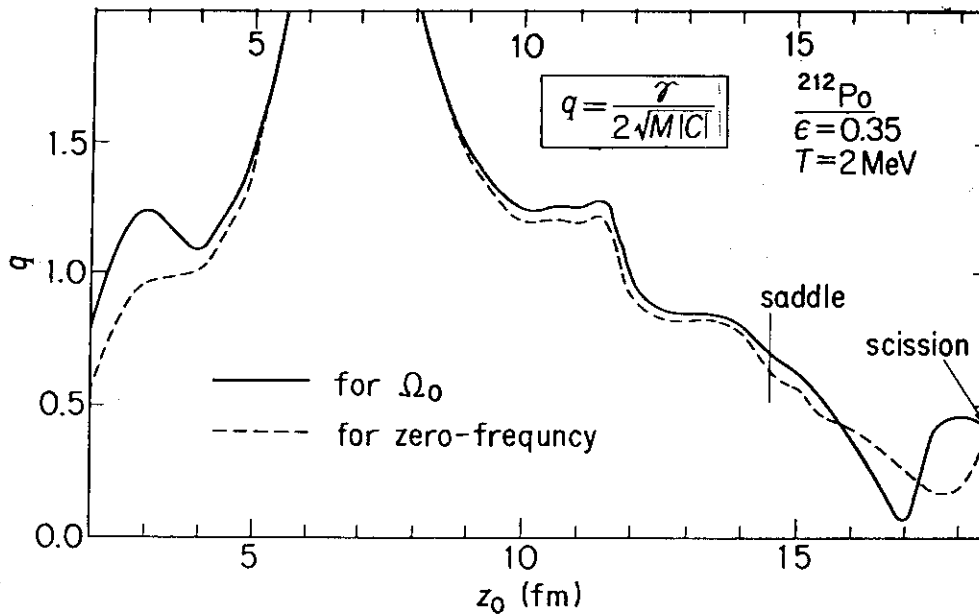


Fig.3

From the present microscopic calculation of transport coefficients, we have found that the effect of the local phonon on the parameter  $q$  is large, especially, for large value of stiffness  $C_0$  in the region between barrier and scission, although the parameter  $q$  for zero-frequency reproduces the order of magnitude of the empirical value of  $q$ . This indicates that we have to solve the transport equation which is improved by taking into account the effect of the local phonon on the coefficients in order to study the collective motion of fission.

#### References

- 1) H.Hofmann, and A.S.Jensen: Nucl.Phys.A428,1c(1984).
- 2) A.Iwamoto,S.Yamaji,S.Suekane,and K.Harada: Prog.Theor.Phys.,55,115 (1976).
- 3) P.J.Siemens, A.S.Jensen, and H.Hofmann: Nucl.Phys.,A441,410 (1985).
- 4)H.J.Krappe,J.R.Nix, and A.J.Sierk: Phys.Rev.,C20,992(1979).
- 5)J.R.Nix,A.J.Sierk,H.Hofmann,F.Scheuter,and D.Vautherin:Nucl.Phys.,  
A424,239(1984).
- 6)H.Hofmann, and P.J.Siemens: Nucl.Phys.A275,464(1977).

## 21. Neutron Emission from High Temperature Region Formed in Heavy Ion Reactions

J. Kasagi

Department of Physics, Tokyo Institute of Technology

We have studied  $^{14}\text{N}+^{165}\text{Ho}$  and  $^{14}\text{N}+\text{Ni}$  collisions at 35 MeV/nucleon by detecting neutrons at ten angles from  $10^\circ$  to  $160^\circ$  in coincidence with light fragments at six angles between  $7^\circ$  and  $30^\circ$ . The fragment energy and angular distributions show a rather clear division into quasi-elastic processes leading to high energy fragments and strongly damped reactions leading to low energy fragments. We set gates across high energy and low energy fragments and examined the coincident neutron spectra. The neutron spectra consisted of three components: The projectile-like fragment (PLF) and the target-like source (TLS), and a preequilibrium component ascribed to an intermediate-rapidity source (IRS). For the present work we neglected the PLF contribution and focused on the TLS and IRS components. Each source was described by four parameters (temperature, speed, direction and multiplicity) to be determined by fitting the neutron spectra. In fig. 1 shown are the neutron energy spectra from the  $^{14}\text{N}+\text{Ni}$  reaction in coincidence with C and Li fragments. Solid and dashed lines in the figure are the results of the fit.

The fit parameters describing the TLS were compared with a two-body kinematics, with the observation that there was considerable missing momentum in the forward direction, especially for highly damped collisions. We have concluded that part of the missing momentum is due to preequilibrium particle emission.

The TLS temperature is about 2.5 MeV with the Ho target and about 3.5 MeV with the Ni target. In spite of the fact that the temperature is independent of fragment angle, the number of TLS neutrons per fragment increases with fragment angle. Comparison

of this TLS associated multiplicity with predictions from the statistical code CASCADE<sup>1)</sup> indicates that many collisions resulting in a detected fragment do not excite the target fragment to energies above the neutron emission threshold.

The speed of the IRS, about one-half the projectile speed, is an order of magnitude greater than the speed of the TLS. In peripheral collisions the IRS is described to the side of the beam opposite the coincident fragment, and its high speed then produces a left/right asymmetry of its emitted neutrons, as can be seen in fig.1. The neutron multiplicity of the IRS is about 1/4 the multiplicity of the TLS. The temperature of the IRS is about 8.5 MeV when the target is Ho and about 10 MeV when it is Ni.

The mass number of the IRS in central collisions was estimated by using the energy-momentum conservation with final three body products. When the target is Ni, all four fragment species, Li, Be, B and C, are associated with the same mass numbers about 10-15. Only a fraction of the 14 projectile nucleons are forming an IRS with target nucleons. When the target is Ho the values are larger.

Examination of the IRS fit parameters shows that neither temperature nor speed exhibits a clear trend with fragment energy or angle. We interpret this as an indication that preequilibrium neutrons are emitted in the very early stages of the interaction before the "final fate" of the fragment has been determined. The IRS may be an evolving localization of high excitation energy with neutrons emitted early after its formation when the IRS is "hot and small".

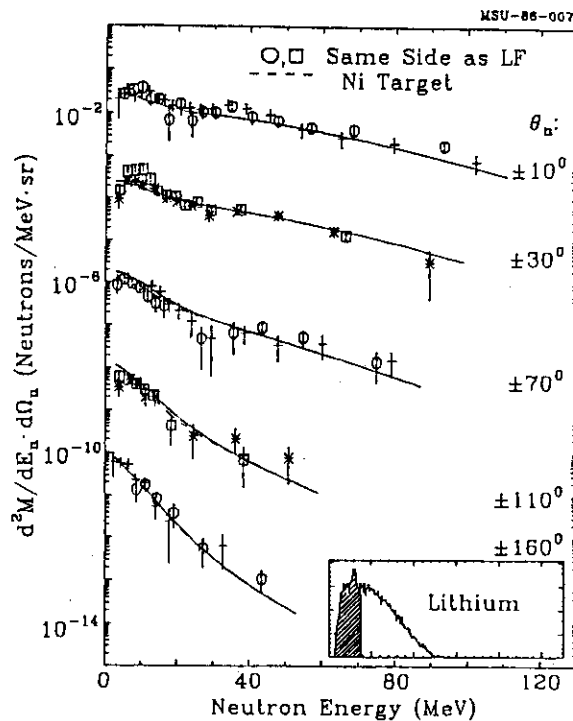
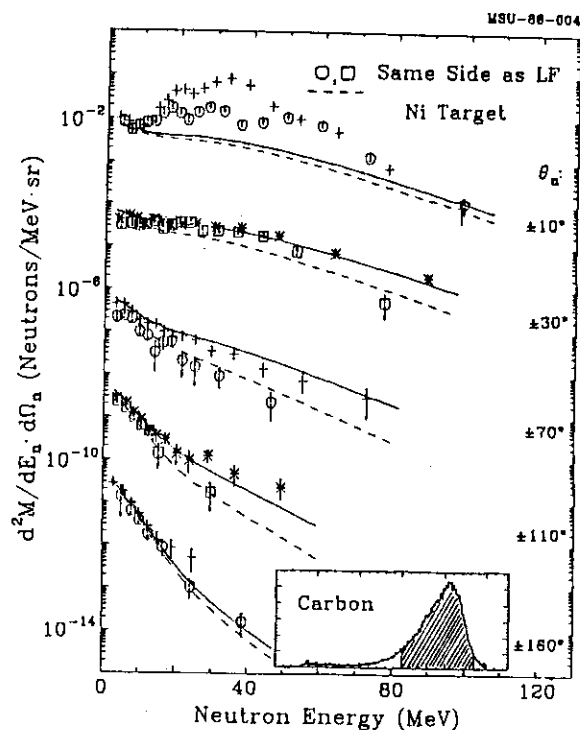
The experiment was performed at cyclotron laboratory of Michigan State University with B.A. Remington, G. Caskey, A. Galonsky, M.B. Tsang, C.K. Gelbke, A. Kiss, F. Deak, Z. Seres and J.J. Kolata.

## Reference

- 1). F. Puhlhofer, Nucl. Phys. A280, 267(1977).

## Figure caption.

Fig. 1. Neutron energy spectra for coincident fragments of high energy carbon (left figure) and low energy lithium (right figure). The spectra are plotted in symmetric angle pairs, each offset from the next by a factor of 100, with the spectra at the top having the scale indicated.



## 22. Phase Anomaly for Elastic and Inelastic Scattering of the $^{19}\text{F}+^{16}\text{O}$ System

H.Fujita<sup>\*</sup>, N.Kato<sup>\*\*</sup>, T.Tachikawa<sup>\*\*\*</sup>, T.Sugimitsu<sup>\*\*</sup>, K.Kimura<sup>\*\*</sup>,  
Y.Ikeda<sup>\*\*\*</sup>, H.Yamaguchi<sup>\*\*</sup>, Y.Nakajima<sup>\*\*\*</sup>, Y.Sugiyama<sup>+</sup>, Y.Tomita<sup>+</sup>,  
H.Ikezoe<sup>+</sup>, K.Ideno<sup>+</sup>, N.Shikazono<sup>+</sup>, S.Kubono<sup>++</sup> and M.Tanaka<sup>++</sup>

\*Daichi College of Pharmaceutical Sciences, \*\*Department of Physics,  
Kyushu University, \*\*\*Sumitomo Heavy Industrial Co., +Department of  
Physics, Japan Atomic Energy Research Institute and ++Institute for  
Nuclear Study, University of Tokyo

In the  $^{19}\text{F} + ^{12}\text{C}$  system, it has found that the inelastic angular distributions for  $L=2$  transitions to the lowest  $5/2+$  and  $3/2+$  states are almost in phase with the elastic one in the wide energy range of 30 to 60 MeV<sup>1)</sup>. This phenomenon can not be explained by the DWBA or CC calculations using macroscopic rotational model<sup>1)</sup>. But, it has recently been shown that the CC calculations introducing a spin-orbit (SO) potential with  $V_{\text{so}} = -0.3$  MeV reproduced fairly well at all the energies<sup>2)</sup>. However this SO potential used in the calculation could not be simply thought due to bare SO interaction but may reflect various channel coupling effects. One of the possible origins may be the influence of the excitation of  $^{12}\text{C}$  because it is a strongly deformed nucleus and easily excited. Therefore to avoid the influence of the  $^{12}\text{C}$  excitation, we performed the experiment changed the projectile to a spherical nucleus  $^{16}\text{O}$ , for which the coupling effect is expected to be much less than for  $^{12}\text{C}$ . The angular distributions are measured for the elastic and inelastic scattering on  $^{19}\text{F}$  leading to the

Table 1. Optical potential parameters used in the CC calculations and deformation parameters of  $^{19}\text{F}$ .

Pot.	Set	V	r <sub>R</sub>	a <sub>R</sub>	W	r <sub>I</sub>	a <sub>I</sub>	V <sub>so</sub>	r <sub>so</sub>	a <sub>so</sub>	beta2	beta4
60MeV	No SO	28.02	1.18	0.71	8.99	1.34	0.592	-	-	-	0.18	0.07
	SO	28.02	1.227	0.667	8.99	1.34	0.592	-0.6	1.18	0.71	0.18	0.07
80MeV	No SO	28.02	1.18	0.71	8.99	1.34	0.580	-	-	-	0.19	0.07
	SO	28.02	1.227	0.667	8.99	1.34	0.580	-0.6	1.18	0.71	0.19	0.07

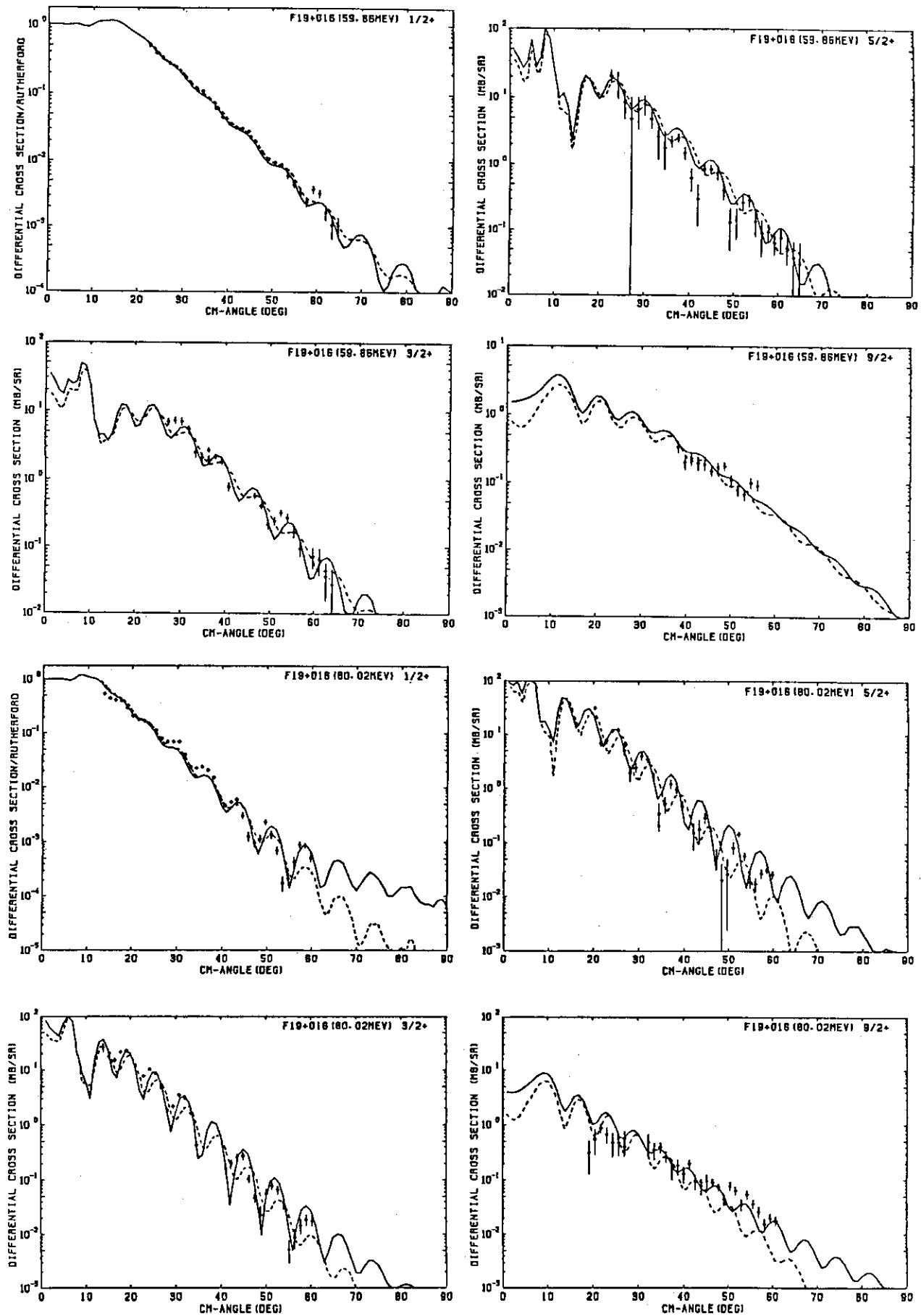


Fig.1. The angular distributions of the elastic and inelastic scattering for  $^{19}\text{F} + ^{16}\text{O}$  at 60 and 80 MeV. See text.

$1/2+(g.s.)$ ,  $5/2+(0.197\text{MeV})$ ,  $3/2+(1.554\text{MeV})$  and  $9/2+(2.780\text{MeV})$  states. The 60 and 80 MeV  $^{16}\text{O}$  beams were obtained from the JAERI tandem accelerator and the ejectiles were analyzed using the heavy-ion magnetic spectrograph "ENMA".

Fig.1 shows the experimental data and the theoretical curves obtained by the CC calculations not including the SO potential (dashed line) and including (solid line) at both energies. The inelastic data of the  $5/2+$  and  $3/2+$  states can not be reproduced by the CC calculations not including the SO potential at both energies. This situation is almost similar to the  $^{19}\text{F}+^{12}\text{C}$  case, although the oscillations of the inelastic data are not in phase with the elastic one. Then the CC calculations including the SO potential were performed. We used the SO potential had the standard form:

$$U_{\text{so}}(r) = 2 \left( \frac{\hbar}{m_{\pi}c} \right)^2 \frac{V_{\text{so}}}{r} \frac{df(r)}{dr} \vec{L} \cdot \vec{I} = V_{\text{ls}}(r) \vec{L} \cdot \vec{I}.$$

The sign and magnitude of  $V_{\text{so}}$  were changed and for each  $V_{\text{so}}$  the optical potential parameters (especially  $r_R$  and  $a_R$ ) were searched so that the calculations reproduced the elastic data. As shown in fig.1, the CC calculations including the SO potential with  $V_{\text{so}} = -0.6\text{MeV}$  reproduce well the inelastic data at both energies. The potential parameters are listed in table 1.

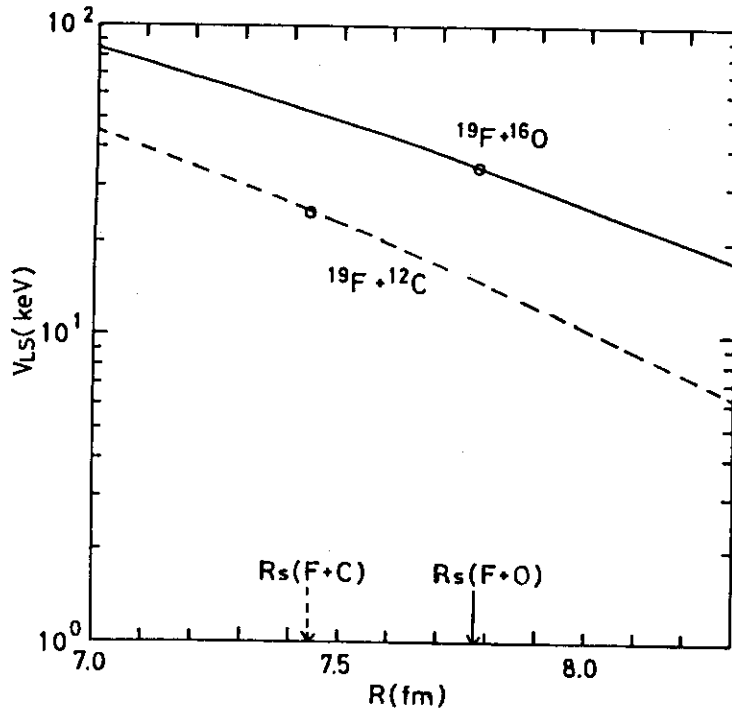


Fig.2. The spin-orbit potentials for  $^{19}\text{F}+^{16}\text{O}$  and  $^{19}\text{F}+^{12}\text{C}$  in the vicinity of the strong absorption radius.

The behavior of the SO potential  $V_{\text{ls}}(r)$  for  $^{19}\text{F}+^{16}\text{O}$  in the vicinity of the strong absorption radius  $R_s = 1.5 \times (A_t^{1/3} + A_p^{1/3})$  is shown in fig.2 together with the  $^{19}\text{F}+^{12}\text{C}$  case. Both systems have nearly equal value  $V_{\text{ls}} = 30\text{keV}$  at the strong absorption radii. This may indicate that the present phase anomaly is a common phenomenon for both systems and due to the property of  $^{19}\text{F}$ .



Recently Ohkubo and Kamimura<sup>3)</sup> have investigated the dynamically induced SO interaction of  $^{19}\text{F}$  scattering from  $^{28}\text{Si}$  at  $E_L = 60\text{MeV}$  with the CC method including the excitation of the  $t+^{16}\text{O}$  cluster states of  $^{19}\text{F}$ . For this system, Kubono et al.<sup>4)</sup> reported a strong SO potential to explain a marked  $j$ -dependence of the cross section of the  $^{28}\text{Si}(^{19}\text{F}, ^{16}\text{O})^{31}\text{P}$  reaction. This SO potential has negative  $V_{1s}(r)$  and is more than one or two orders of magnitude larger than the single-particle or cluster folding model estimates (which have also negative  $V_{1s}(r)$ )<sup>3,5)</sup>. It is noticed that the signs of the SO potentials for  $^{19}\text{F}+^{12}\text{C}$  and  $^{19}\text{F}+^{16}\text{O}$  are opposite to the one suggested empirically and theoretically for  $^{19}\text{F}+^{28}\text{Si}$ . The results in ref.3) are as follow: The effective SO potential induced by the  $1/2+ - 5/2+$  coupling is attractive, but the one by the  $1/2+ - 3/2+$  coupling is repulsive; in the coupling of  $1/2+ - 5/2+ - 3/2+$  is induced the attractive SO potential weakened by the cancellation of preceding two potentials. The CC calculations is now in progress including the excitation of the  $t+^{16}\text{O}$  cluster states abovementioned for  $^{19}\text{F}+^{12}\text{C}$  and  $^{19}\text{F}+^{16}\text{O}$  as the next step.

#### References

- 1) T.Tachikawa et al., Phys. Lett. 139B (1984) 267.
- 2) T.Tachikawa et al., to be published; T.Tachikawa, Ph.D Thesis, Kyushu University (1984).
- 3) S.Ohkubo and M.Kamimura, Phys. Lett. 150B (1985) 25.
- 4) S.Kubono et al., Nucl. Phys. A334 (1980) 336.
- 5) M.B.Golin and S.Kubono, Phys. Rev. C20 (1979) 1347.

## 23. Examination of Spin-Orbit Term in the Optical Potential for Light Heavy Ions

Takashi Yamaya<sup>\*</sup>, Osamu Satoh<sup>\*</sup>, Kyuya Kotajima<sup>\*\*</sup>, Kazuo Hasegawa<sup>\*\*</sup>,  
Tsutomu Shinozuka<sup>\*\*\*</sup> and Manabu Fujioka<sup>\*\*\*</sup>

<sup>\*</sup>Department of Physics, Faculty of Science, Tohoku University, <sup>\*\*</sup>Department of Nuclear engineering, Tohoku University and <sup>\*\*\*</sup>Cyclotron and Radioisotope Center, Tohoku University.

There has been considerable recent interest in the spin-orbit term in the heavy-ion optical potential. In heavy-ion elastic scattering data at relating low bombarding energies ( $< 10$  MeV per nucleon) which often are not very far above the Coulomb barrier, the scattering is sensitive to the potential in the vicinity of the strong absorption radius. In the general spin-orbit coupling interaction picture  $V_{ls}(r) < 0$  for  $j = l+s$  and  $V_{ls}(r) >$

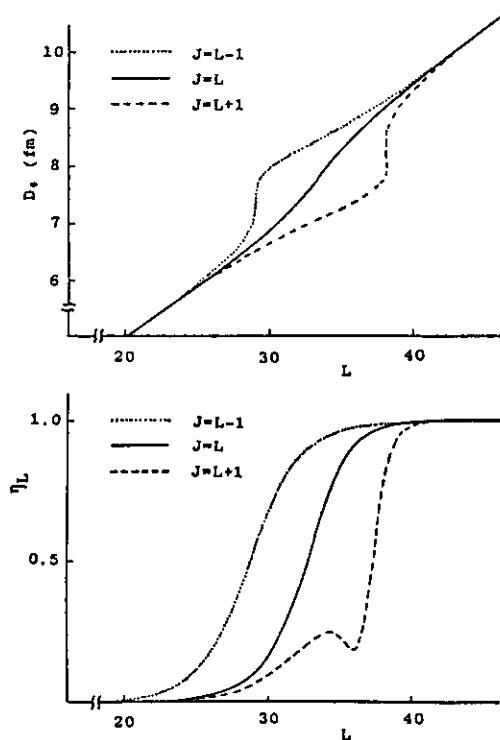


Fig. 1. Location of the closest approach points  $D_0$  (top) and the scattering reflection coefficient  $\eta_L$  (bottom) as a function of the orbital angular momentum  $L$ .

$0$  for  $j = l-s$ . It is important to note the difference in sign between the spin-orbit coupling interactions in the region of the strong absorption radius. Projectiles distorted to be nearing the target nuclei by the negative spin-orbit interaction are more strongly absorbed, and on the contrary projectiles distorted to be far from the target nuclei by the positive spin-orbit interaction weaken the effect of absorption. A qualitative description is shown the results of the optical model calculation for  $^{28}\text{Si}+^{14}\text{N}$  system at  $E = 84$  MeV in Fig. 1.

In order to obtain information of the angular distribution dependent on the projectile spin for the heavy-ion elastic scattering, we have measured the differential cross sections for the system  $^{12}\text{C}+^{28}\text{Si}$ ,  $^{13}\text{C}+^{28}\text{Si}$ ,  $^{14}\text{N}+^{28}\text{Si}$  and  $^{16}\text{O}+^{28}\text{Si}$  at 65, 60, 84 and 75 MeV, respectively.

The beams of  $^{12}\text{C}^{4+}$ ,  $^{13}\text{C}^{4+}$ ,  $^{14}\text{N}^{5+}$  and  $^{16}\text{O}^{5+1)}$  were provided from the Tohoku University 680-cyclotron. The angular distributions were measured in a range of  $\theta_{\text{cm}} = 6^\circ - 70^\circ$  in step of about  $1^\circ$ . Scattered heavy ions were detected with a counter system of two telescopes which consist of two  $\Delta E$  surface barrier detectors and a position sensitive surface barrier detector. In this counter system, two  $\Delta E$  detectors were placed in a row along a surface of a position sensitive detector. Each telescope has three slits and the spectra at six angles can be measured at the same time.

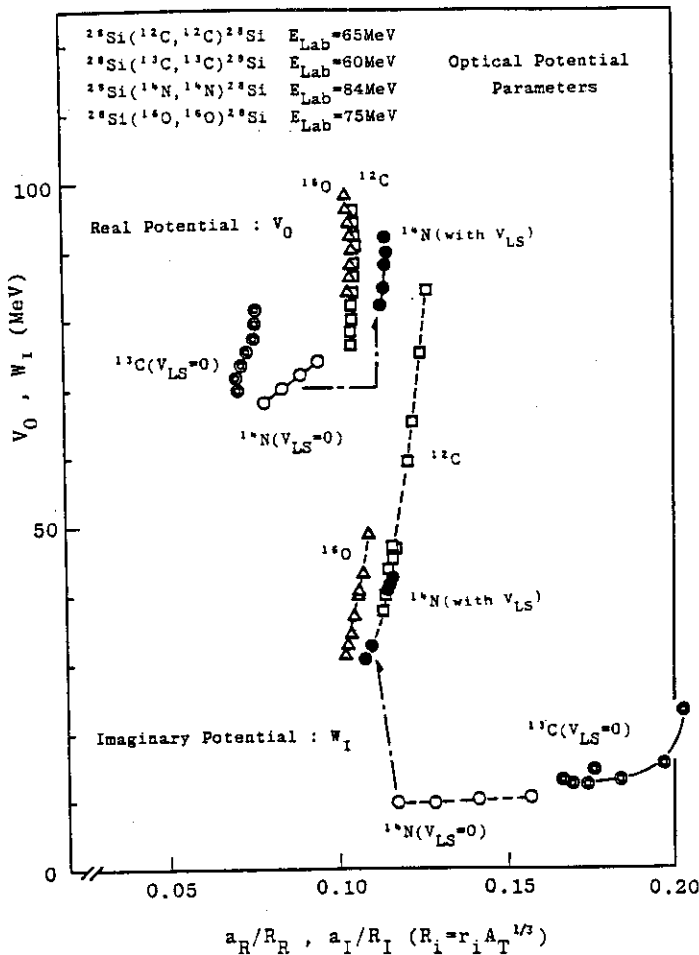
The ratio of the experimental differential cross sections to Rutherford scattering were analyzed in a framework of the optical model distorted wave approximation method. The optical model potential search code ELAST2<sup>2)</sup> was used to fit the data. The potentials studied by Cramer et al.<sup>3)</sup> and by Satchler<sup>4)</sup> have been applied for fitting the present data, however, the parameters were adjusted so as to get best fit to the present data. The typical parameters obtained from the present analysis are shown in Table 1. As seen in Table 1, the optical model parameters for  $^{12}\text{C}$  and  $^{16}\text{O}$  projectiles with spin 0 were consistent. But the optical model parameters without the

Table 1 Optical Potential Parameters

	$V_0(\text{MeV})$	$r_R(\text{fm})$	$a_R(\text{fm})$	$W_0(\text{MeV})$	$r_I(\text{fm})$	$a_I(\text{fm})$	$V_{SO}(\text{MeV})$	$r_{SO}(\text{fm})$	$a_{SO}(\text{fm})$	$r_C(\text{fm})$	$\chi^2/N$
$^{12}\text{C}+^{28}\text{Si}$	88.00	1.868	0.579	39.87	1.845	0.639	-	-	-	2.280	36.6
$^{13}\text{C}+^{28}\text{Si}$	76.00	2.058	0.464	12.24	2.048	1.048	-	-	-	2.307	3.22
$^{14}\text{N}+^{28}\text{Si}$	70.00	2.063	0.527	10.08	2.152	0.920	-	-	-	2.332	6.29
	88.00	1.912	0.665	41.07	1.901	0.665	0.162	3.189	0.679	2.332	10.9
$^{16}\text{O}+^{28}\text{Si}$	90.00	1.951	0.621	31.07	2.048	0.635	-	-	-	2.379	7.04

$$R_i = r_i A_T^{1/3}$$

spin-orbital term for  $^{13}\text{C}$  and  $^{14}\text{N}$  projectiles with spin 1/2 and 1, respectively, were markedly different from those for spin 0 projectiles. The quality of the fits was appraised by minimum values of the reduced chi-square  $\chi^2$  divided by the number of degrees of freedom. These values were in the range 3 - 10, and the errors having been calculated from the statistics only. Sets of the best fit potential parameters without the spin-orbital term for the  $^{12}\text{C}$ ,  $^{13}\text{C}$ ,  $^{14}\text{N}$  and  $^{16}\text{O}$  projectiles are plotted in the Fig. 2 for the real and imaginary term separately. The quality of these overall fits is characterized by a  $\chi^2$  with 5 % uncertainty of the individual  $\chi^2$ -minimum values. As seen in Fig. 1, the values of  $a_0/R$  for the projectiles with spin 0 i.e  $^{12}\text{C}$ ,  $^{16}\text{O}$ , are constant for the variety of the potential depth, and



both parameters sets of  $^{12}\text{C}$  and  $^{16}\text{O}$  are almost consistent. In a contrary those of the projectiles with spin 1/2 and 1 i.e.  $^{13}\text{C}$  and  $^{14}\text{N}$ , are not constant for the variety of the potential depth. For  $^{14}\text{N}$  projectile, the analysis using the optical model potential with the spin-orbit term has been done. The best fit of optical potential parameters sets are plotted with the solid circles in the Fig. 2. This result shows that the values of  $a_0/R$  for the real and the imaginary potential are almost constant and the central terms of the optical potential are improved into the central potential parameters of  $^{12}\text{C}$  and  $^{16}\text{O}$  projectiles. It is suggested that the spin-orbit term of the optical model potential cannot be negligible for the elastic scattering of the light composite projectiles with spin.

#### References

- 1) T. Yamaya et al., Nucl. Instr. & Meth. 203 (1982) 7, and Nucl. Instr. & Meth. 226 (1984) 219
- 2) M. Igarashi, private communication.
- 3) J.G. Cramer et al., Phys. Rev. C14 (1976) 2158
- 4) G.R. Satchler, Nucl. Phys. A279 (1977) 493

24. Coupled-Channel Study of ( ${}^6\text{Li}, \alpha d$ ) and ( ${}^7\text{Li}, \alpha t$ ) Reactions

Yukinori Sakuragi

Institute for Nuclear Study, University of Tokyo, Tanashi, Tokyo, 188

1. Introduction and Method

In nuclear reactions induced by loosely-bound projectiles such as deuteron and lithium isotopes, projectile breakup processes are known to play significant roles in the reaction mechanism. Among theoretical approaches to the processes, the method of coupled discretized continuum channels (CDCC) <sup>1)</sup> has been recognized as suited and powerful for a comprehensive study of deuteron-induced nuclear reactions, such as (d,d), (d,d'), (d,p) and (d,pn) breakup reaction itself. <sup>2)</sup> Recently, the method has been successfully applied also to the elastic scattering of lithium isotopes; <sup>3)</sup> the breakup process has been found to have significant effects on the scattering. In the present report, we show an recent successful application of the method to the lithium-induced breakup reactions themselves, i.e. ( ${}^6\text{Li}, \alpha d$ ) and ( ${}^7\text{Li}, \alpha t$ ) reactions.

In the CDCC framework, an effective model space is truncated out from the breakup continua in the three-body wave function and discretized into a finite number of momentum bins; hence, each of the bins can be treated as if discrete excited states of the projectile nucleus. The internal states (both bound and unbound-continuum states) of  ${}^6\text{Li}$  ( ${}^7\text{Li}$ ) nucleus are described by an microscopic  $\alpha$ -d ( $\alpha$ -t) cluster model; the wave functions of the states are successfully examined by electron-scattering form factors, r.m.s. radii, B(E2) strength and  $\alpha$ -d ( $\alpha$ -t) scattering phase shifts. The lithium-target real potentials (both diagonal and transition potentials) are provided by the double-folding of the M3Y effective N-N interaction <sup>4)</sup> with the nucleon densities of both nuclei. The imaginary part of the potentials is assumed to have the same geometry as that of the real folding potentials, the strength of which being the only adjustable parameter in the present framework. The breakup cross sections for bins are given as the solution of the coupled-channel (CC) equations with the potentials; since the breakup continuum is discretized into bins, an interpolation is made in the comparison with the observed breakup cross sections. In contrast to the case of deuteron, there exist resonances in the continua for lithium isotopes; analyses are made of the breakup via the resonances as well as that via non-resonant continua.

## 2. ( ${}^7\text{Li}, \alpha t$ ) breakup reactions by ${}^{12}\text{C}$ and ${}^{120}\text{Sn}$

First, we analyze  ${}^7\text{Li} \rightarrow \alpha + t$  breakup reaction by  ${}^{12}\text{C}$  and  ${}^{120}\text{Sn}$  targets at  $E_{\text{lab}} = 70$  MeV.<sup>5,6)</sup> As the model space, we take  $\alpha$ - $t$  breakup continua in P-wave ( $\ell=1$ ) and F-wave ( $\ell=3$ ) up to  $k=1.0$  fm $^{-1}$  ( $k$  and  $\ell$  are the  $\alpha$ - $t$  relative momentum and angular momentum, respectively), as well as the  $3/2^-$  ground state and  $1/2^-$  first excited state at  $E_x = 0.48$  MeV. Note that in F-wave there exist  $7/2^-$  and  $5/2^-$  resonance states at  $E_x = 4.63$  and  $6.68$  MeV, respectively. The continua are discretized as shown in Fig.1.

Figure 2 shows the observed<sup>5)</sup> and calculated breakup cross sections via the  $7/2^-$  resonance in the case of  ${}^{12}\text{C}$  target, which is shown with respect to the scattering angle of the c.m. of breakup fragments ( $\alpha$  and  $t$ ). The parameter for the imaginary-potential strength, say  $N_I$ , has been determined in such a way that the calculation reproduces the elastic scattering at  $E_{\text{lab}} = 63$  and  $79$  MeV and an interpolation is made to deduce the value for  $70$  MeV, which gives  $N_I = 0.45$ . It should be noted that, once we determine the value of  $N_I$  as above, no free parameter is left in the prediction of the breakup cross sections. Thus, an agreement of the CDCC prediction with the experimental data would be satisfactory, in both absolute magnitude and angular distribution.

Similar analysis is made in the case of  ${}^{120}\text{Sn}$  target. The results are shown in Figs.3a and 3b for the breakup via the  $7/2^-$  resonance and via the non-resonant continuum with  $0.29 \leq E_r \leq 3.0$  MeV, respectively ( $E_r$  is the  $\alpha$ - $t$

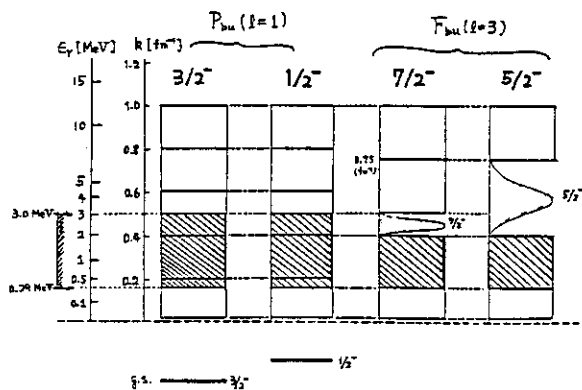


Fig.1 Truncation and discretization of the  $\alpha$ - $t$  breakup continua. There exist  $7/2^-$  and  $5/2^-$  resonances in F-wave ( $\ell=3$ ). The hatched region shows the non-resonant continua corresponding to the observed data in Fig.3b.

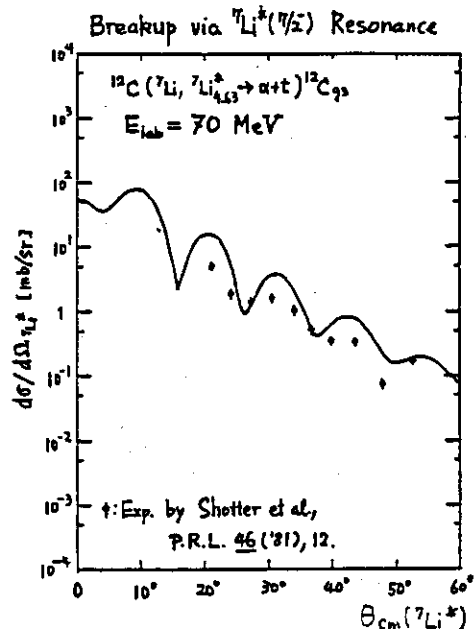


Fig.2 Observed<sup>5)</sup> and calculated breakup cross sections via the  $7/2^-$  resonance for  ${}^{12}\text{C}$  target at  $E_{\text{lab}} = 70$  MeV.

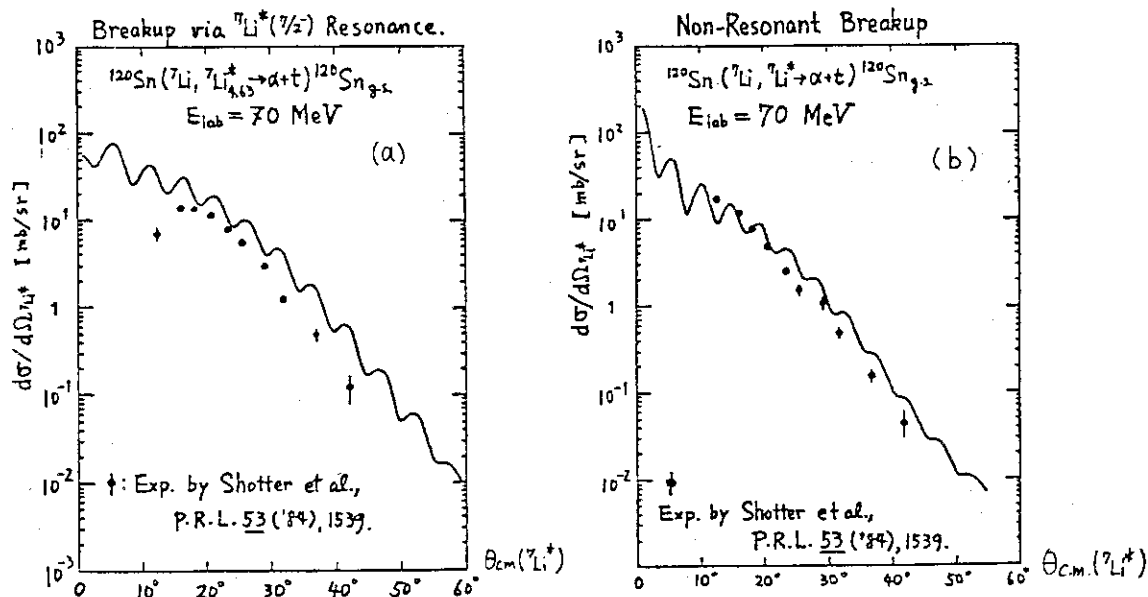


Fig.3 Observed<sup>6)</sup> and calculated breakup cross sections (a) via the  $7/2^-$  resonance and (b) via the non-resonant continua with  $0.29 \leq \epsilon_r \leq 3.0$  MeV for  $^{120}\text{Sn}$  target at  $E_{lab} = 70$  MeV.

c.m. energy); the continuum is indicated by the hatched region in Fig.1. The CDCC prediction satisfactorily reproduces the observed data;<sup>6)</sup> the value of  $N_I$  has been chosen as 0.45. The calculation includes the breakup process in the field of nuclear interaction; the Coulomb breakup has been found to play minor roles except at forward angles ( $\theta_{cm} \leq 20^\circ$ ) where the inclusion of it improves the fit in Fig.3a.

### 3. $(^6\text{Li}, \alpha d)$ breakup reactions by $^{12}\text{C}$ and $^{208}\text{Pb}$

Next, we analyze  $^6\text{Li} \rightarrow \alpha + d$  breakup reactions by  $^{12}\text{C}$  and  $^{208}\text{Pb}$  targets at  $E_{lab} = 178$  MeV.<sup>7)</sup> The model space adopted is shown in Fig.4; there exist  $3^+$ ,  $2^+$  and  $1^+$  resonances in D-wave ( $\ell=2$ ) at  $E_x = 2.19$ , 4.31 and 5.65 MeV, respectively. The observation has been made of the breakup via the continuum with  $0.0 \leq \epsilon_r \leq 1.0$  MeV (region I) and that with  $1.0 \leq \epsilon_r \leq 4.0$  MeV (region II); the  $3^+$  and the  $2^+$  resonance are included in the region I and II, respectively. In Fig.5a, the CDCC prediction for  $^{12}\text{C}$  target is shown together with the experimental data; the dashed and dotted curves indicate respectively the contributions of the resonance and the non-resonance part for each region, and the solid one shows the sum of them. In the region I, the breakup occurs chiefly via the  $3^+$  resonance, while, in the region II, the non-resonant breakup is as important as the  $2^+$  resonance. Similar result is obtained for  $^{208}\text{Pb}$  target (Fig.5b); the contribution of the non-resonant yield in the region II is more prominent than for  $^{12}\text{C}$  target. For both

Figure 1 shows the angular distribution of the differential cross section for the reaction  $^{12}\text{C}(^6\text{Li}, ^6\text{Li}^*)^{12}\text{C}_{\text{g.s.}}$  at  $E(^6\text{Li}) = 178 \text{ MeV}$ . The plot is divided into two energy regions for the target nucleus  $^{12}\text{C}$ :

- Top Panel:**  $0.0 \leq E_T \leq 1.0 \text{ MeV}$ . The y-axis ranges from  $10^1$  to  $10^3 \text{ mb/sr}$ . Theoretical curves are shown for  $3^*(2.91 \text{ MeV}) \text{ Res.}$  (dashed line),  $\text{Non-res.}$  (dotted line), and  $\text{Sum.}$  (solid line). Experimental data points with error bars are plotted.
- Bottom Panel:**  $1.0 \leq E_T \leq 4.0 \text{ MeV}$ . The y-axis ranges from  $10^{-1}$  to  $10^1 \text{ mb/sr}$ . Theoretical curves are shown for  $2^*(2.91 \text{ MeV}) \text{ Res.}$  (dashed line),  $\text{Non-res.}$  (dotted line), and  $\text{Sum.}$  (solid line). Experimental data points with error bars are plotted.

The x-axis for both panels is the angle  $\theta$  in degrees, ranging from  $0^\circ$  to  $60^\circ$ . The curves show a general decrease in cross section with increasing angle, with some oscillatory behavior at lower angles.

targets, the agreement between the prediction and the data is satisfactory. As in the case of  ${}^7\text{Li}$  breakup, further inclusion of the Coulomb-breakup process may not affect so much the present result in Figs.5a and 5b.

## References



25. Intermediate resonances observed in the  $^{12}\text{C} + ^{16}\text{O}$  fusion channels

Tsuyoshi Sugimitsu, Kikuo Kimura, Norihisa Kato, Hiroshi Fujita,  
Yuichi Ikeda and Yutaka Nakajima

Department of Physics, Faculty of Science, Kyushu University

It has been observed that in many cases the intermediate resonance has a certain correlated strength in the fusion channels<sup>1)</sup>. But it is not clear if it is coming via the formation of a compound nucleus or from some pre-equilibrium stages of the multistep processes. To investigate it in more detail the measurement of fusion excitation function was made at  $E_{\text{cm}} = 19$  to 24 MeV, remembering two groups of resonances are known in this region. Reaction products from the  $^{12}\text{C}(^{16}\text{O}, \text{X})$  reaction were detected at  $\theta_{\text{L}} = 8$  deg with a TOF- $\Delta E$ -E system. The resulting excitation function for each isotope is shown in fig. 1. Here the total  $^{20}\text{Ne}$  yields are divided into a two-body component ( $^{20}\text{NeDI}$ ) and a evaporation one ( $^{20}\text{NeCN}$ ) from its energy spectrum. For each resonance reported previously in the  $^{12}\text{C}(^{16}\text{O}, ^8\text{Be})^{20}\text{Ne}$  channels, resonant yields are found to be present strongly in  $^{20}\text{NeCN}$  and weakly in  $^{23}\text{Na}$  or  $^{24}\text{Mg}$ .

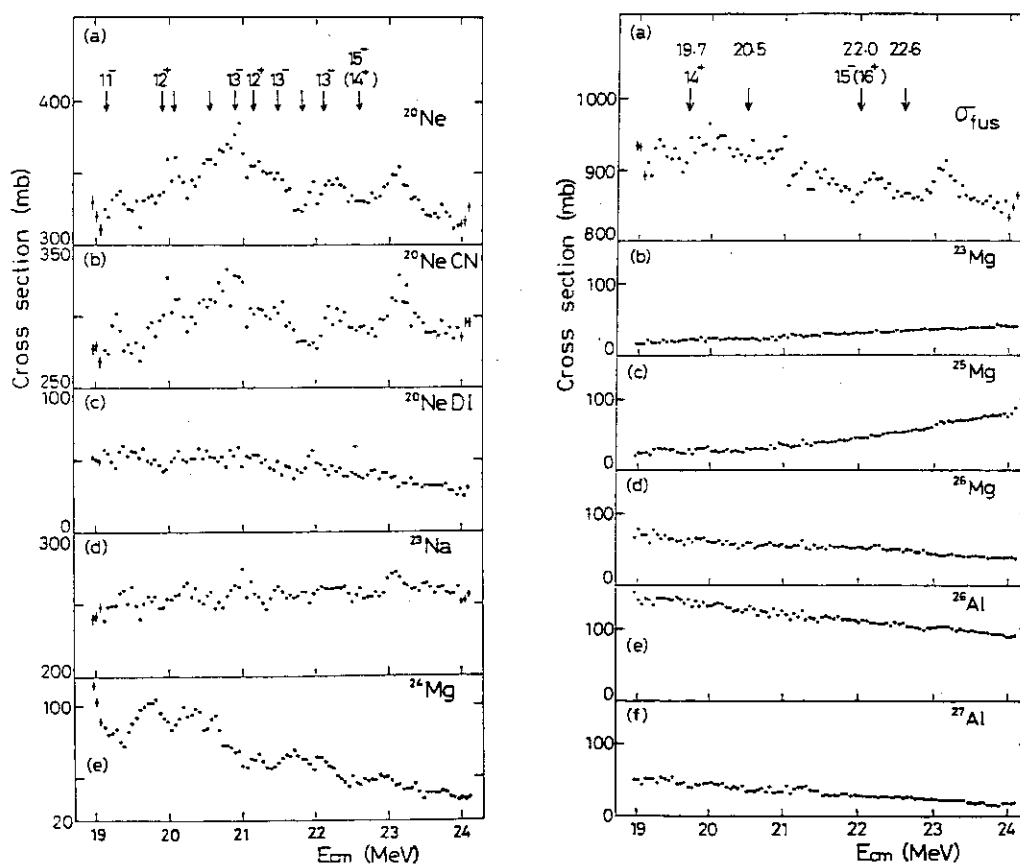


Fig. 1. Excitation function for evaporation residues.

If these resonant cross sections are resulting via the equilibrium processes, their relative intensity will be predicted by the compound nucleus theory. In fig. 2 are compared the observed resonant cross sections with the prediction of CASCADE. For each mass two predictions (blank columns) are given. Those at the right-hand side are calculated by increasing 10 % all the radius parameters used in the optical potentials to simulate the deformation of the compound nucleus, while those at the left-hand side are obtained by using the original radius parameters given in CASCADE. The sum of the theoretical cross sections are adjusted equal to that of the experimental ones. The experimental data at  $E_{cm} = 14.7$  MeV are taken from ref. 2. A fairly good agreement indicates that these resonant yields are coming via the equilibration processes and corresponds to the fact that these resonances have a large width to fusion ( $\Gamma_{CN}/\Gamma = 0.8-0.9$ ). Elastic partial widths are estimated from the total resonant cross sections and their reduced widths are about 1 % of the Wigner limit.

However for three resonances at  $E_{cm} = 19.7$ , 22.0 and 22.6 MeV which were observed to be strongly excited in inelastic channels, the corresponding width to fusion seems negligible. Resonant yields are seen in some reaction products but their relative intensity is not in accord with the theoretical prediction. So they are coming from the preequilibrium stages. The reduced widths of the elastic

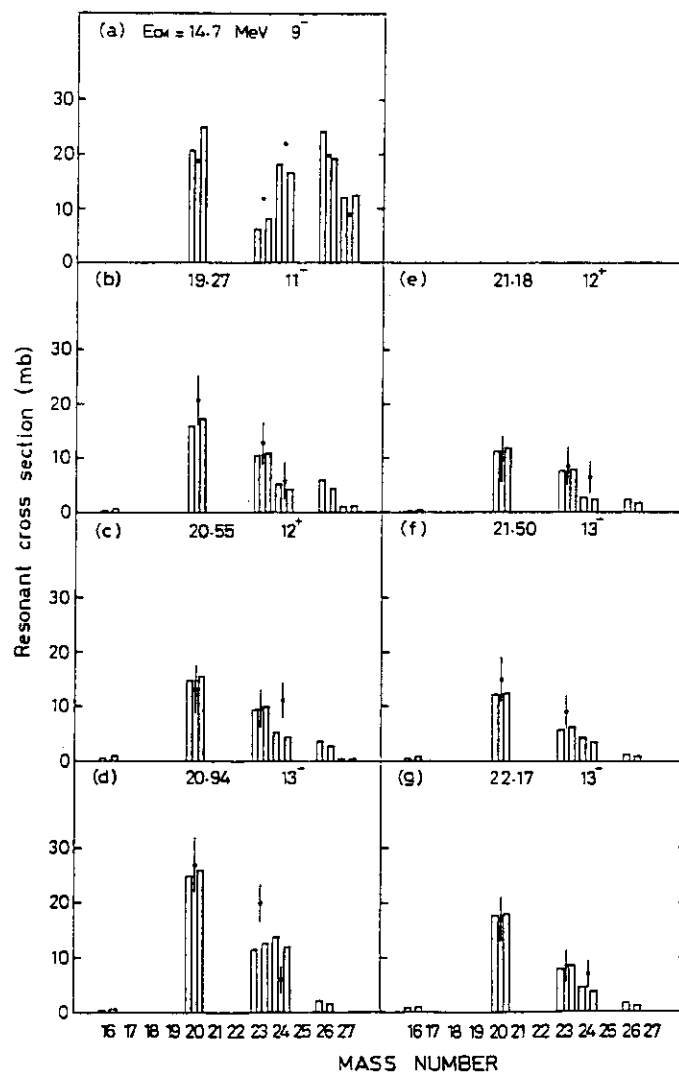


Fig. 2. Comparison of the resonant cross sections with the prediction of CASCADE.

channel are known to be larger.

The contrasting character for these two groups of resonances may be attributed to the structure of the doorway state or to the nuclear level density. The latter seems to play a dominant role, considering that the trajectory of the critical angular momentum is lying between the two groups on the  $E_{\text{cm}}$  vs.  $J(J+1)$  plane as seen in fig. 3. A recent measurement of the fusion cross sections at  $E_{\text{cm}} = 26$  to  $64$  MeV has resulted in an anomalous increase of the critical angular momentum and suggested that it might be due to superdeformation of the compound nucleus<sup>3)</sup>. Detailed studies of elastic partial widths as well as fusion and reaction channel widths for resonances in this energy region are important to clarify this postulate.

#### References

- 1) P. Taras et al., Phys. Rev. Letts. 41 (1978) 840  
A. D. Frawley et al., Phys. Rev. C25 (1982) 860
- 2) A. D. Frawley et al., Phys. Rev Letts. 44 (1980) 1377
- 3) C. Beck et al., Nucl. Phys. A442 (1985) 320

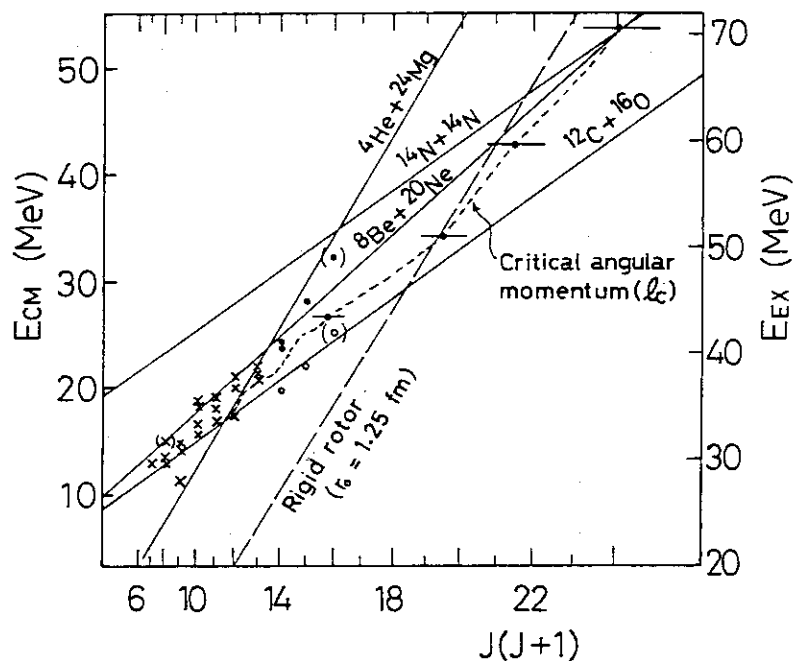


Fig. 3. Plot of the resonances reported and the critical angular momentum on the  $E_{\text{cm}}$  vs.  $J(J+1)$  plane.

## 26. Measurements of Evaporation Residues to Investigate Lower Limiting Angular Momenta in Fusion Reaction

Hiroshi Ikezoe, Naomoto Shikazono, Yoshiaki Tomita, Kazumi Ideno, Yasuharu Sugiyama, Eiko Takekoshi, Toshiki Tachikawa\* and Tohru Nomura\*\*

Department of Physics, Japan Atomic Energy Research Institute,  
\*Industrial Machinery Design Department, Sumitomo Heavy Industries LTD, \*\*Institute for Nuclear Study, University of Tokyo.

Time-dependent Hartree-Fock calculations (TDHF)<sup>1-4)</sup> for low-energy heavy-ion reactions predict that low- $l$  partial waves do not contribute to the formation of the compound nucleus at incident energies above a certain critical value. In order to test the existence of the low- $l$  cutoff experimentally, it is essential to measure such quantities that are very sensitive to the low angular momentum of the entrance channel. Statistical model calculations show that high-spin states in a highly excited light nucleus preferentially decay by the emission of  $\alpha$ -particles, and that low-spin states deexcite mainly by the emission of nucleons. This is a consequence of the fact that an angular momentum carried away by the nucleon emission is small compared with that by the  $\alpha$ -particle emission. It turns out that yields of evaporation residues (ER) resulting from only nucleon emissions are extremely sensitive to the possible existence of the low- $l$  cutoff. Taking into account this property of the compound nucleus decay we investigated the possible low- $l$  cutoff of the  $^{16}\text{O} + ^{12}\text{C}$  and  $^{16}\text{O} + ^{16}\text{O}$  systems by measuring cross sections of their ERs.

Figure 1 and fig.2 show the measured cross sections of ERs which are mainly produced via only nucleon emissions in the  $^{16}\text{O} + ^{12}\text{C}$  and the  $^{16}\text{O} + ^{16}\text{O}$  reactions, respectively, together with the statistical model calculation CASCADE. Solid curves show

the calculated results without the low- $Q$  cutoff, while dash-dotted curves show the calculated results assuming the threshold energy  $E_{th} = 33.4 \text{ MeV}^{5)}$  and  $27 \text{ MeV}^{5)}$  for the low- $Q$  cutoff in the  $^{16}\text{O} + ^{12}\text{C}$  and the  $^{16}\text{O} + ^{16}\text{O}$  systems, respectively. It is clear that the calculated curves without the low- $Q$  cutoff agree fairly well with the experimental data, whereas those assuming the low- $Q$  cutoff predicted by the TDHF calculation differ completely from the observed excitation functions.

However, it is quite natural that the threshold energy predicted by the TDHF calculation should be considered to have some uncertainty due to various approximations included in the theory. We have therefore carried out the similar calculations for various values of  $E_{th}$ . The examples are shown by dashed curves in fig.1 and fig.2, where they correspond to  $E_{th} = 48 \text{ MeV}$  in the  $^{16}\text{O} + ^{12}\text{C}$  system and  $E_{th} = 57.4 \text{ MeV}$  in the  $^{16}\text{O} + ^{16}\text{O}$  system. In the case of the  $^{16}\text{O} + ^{12}\text{C}$  system the results calculated in this way show better agreement with the experimental data for  $^{24}\text{Mg}$ , but the agreement becomes worse for the case of  $^{25}\text{Al}$  and  $^{25}\text{Mg}$ . In the case of the  $^{16}\text{O} + ^{16}\text{O}$  system, the calculated results (dashed curves) differ slightly from those without the low- $Q$  cutoff assumption (solid curves) for  $^{28}\text{Si}$  and  $^{28}\text{Al}$  and agreements with the data of  $^{27}\text{Si}$  and  $^{27}\text{Al}$  become good.

From the present experimental results, it seems reasonable to say that no remarkable effect of the low- $Q$  cutoff does not exist in the measured excitation functions. At the same time, however, we can not completely deny that the smaller yields seen in the excitation function of  $^{24}\text{Mg}$  in the  $^{16}\text{O} + ^{12}\text{C}$  system and the better agreements with the data of  $^{27}\text{Si}$  and  $^{27}\text{Al}$  assuming the threshold energy  $E_{th} = 57.4 \text{ MeV}$  in the  $^{16}\text{O} + ^{16}\text{O}$  system are the possible evidences of the low- $Q$  cutoff.

#### References

- 1) P.Bonche et al., Phys. Rev. C17 (1978) 1700.
- 2) P.Bonche et al., Phys. Rev. C20 (1979) 20.

3) K.R.S.Devi et al., Phys. Rev. C23 (1981) 2062.

4) J.W.Negele, Rev. Mod. Phys. 54 (1982) 913.

5) K.T.R.Davies et al., Phys. Rev. C23 (1981) 2042 .

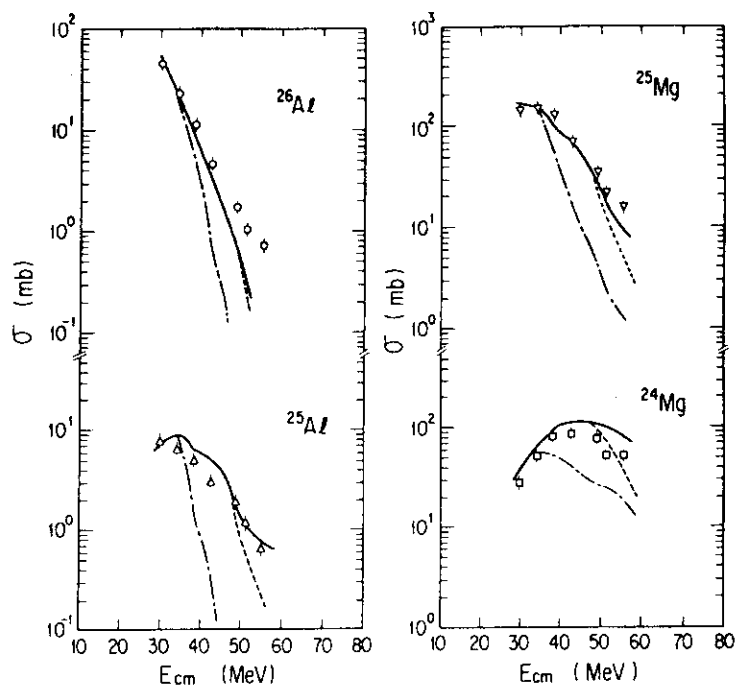


Fig.1 Cross sections measured in the  $^{16}\text{O} + ^{12}\text{C}$  reaction.

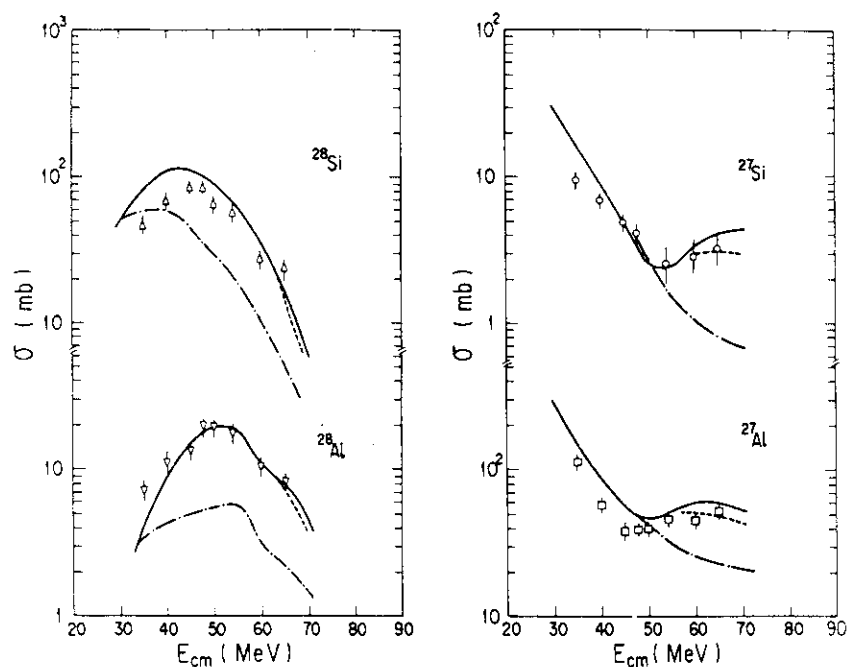


Fig.2 Cross sections measured in the  $^{16}\text{O} + ^{16}\text{O}$  reaction.

## 27. Angular and mass distribution of fission fragments

Takahide NAKAGAWA

Institut of Physics, University of Tsukuba, Ibaraki, Japan

We have already reported on the existence of critical angular momentum  $J_{ER}^{1)2)}$  which distinguished between fusion-fission and fusion-evaporation. In this paper we report on the anisotropy of angular distribution and mass distribution of fission fragments.

Usually the anisotropy (0 degree to 90 degree ratio) of angular distribution of fission fragments increases with increasing incident energy. Fig.1 shows the anisotropy for  $^{16}O + ^{170}Yb$  and  $^{32}S + ^{144,154}Sm$  as a function of  $(\langle J^2 \rangle / T)^{1/2}$  where  $\langle J^2 \rangle$  and  $T$  are mean squared angular momentum and temperature of compound nucleus, respectively. the  $\langle J^2 \rangle$  is defined as follows.

$$\langle J^2 \rangle = \frac{\int_{J_{ER}}^{J_{cr}} (2J + 1) J^2 dJ}{\int_{J_{ER}}^{J_{cr}} (2J + 1) dJ}$$

In Fig.1, the anisotropy of the two systems, which make same compound nucleus  $^{186}Pt$ , give a same straight line and slope of the line for  $^{32}S + ^{154}Sm$  is larger than that for  $^{32}S + ^{144}Sm$ . From these results the anisotropy is strongly dependent on the effects of compound nucleus as a function of  $(\langle J^2 \rangle / T)^{1/2}$ . Fig.2 shows values of slope of the line for various systems. In Fig.2 the value for  $^{16}O + ^{238}U$  (open circle)<sup>3)</sup> deviates from this systematics. In Ref.3, it was reported that the sequential fission cross section was included in fission cross section at higher incident energy. So we have to consider the effect of sequential fission on the angular distribution of fission fragments  $(d\sigma/d\Omega)_{FF}$ . The angular distribution of complete fusion fission  $(d\sigma/d\Omega)_{CFF}$  can be written as follows.

$$(d\sigma/d\Omega)_{CFF} = (d\sigma/d\Omega)_{FF} - (d\sigma/d\Omega)_{SF}$$

where  $(d\sigma/d\Omega)_{SF}$  is a angular distribution of sequential fission. Assuming that the  $(d\sigma/d\Omega)_{SF}$  is isotropic, we can obtain the value of  $(d\sigma/d\Omega)_{CFF}$ . The closed square is the values for complete fusion

fission of  $^{16}\text{O} + ^{238}\text{U}$  in Fig.2. In this figure it is clear that the slope for  $^{16}\text{O} + ^{238}\text{U}$  is almost same as that for  $^{32}\text{S} + ^{208}\text{Pb}$ .

We observed the stronger correlation of mass distribution with averaged angular momentum  $\langle J \rangle$  than excitation energy.  $\langle J \rangle$  is defined as follows

$$\langle J \rangle = \frac{\int_{J_{\text{ER}}}^{J_{\text{cr}}} (2J + 1) J \, dJ}{\int_{J_{\text{ER}}}^{J_{\text{cr}}} (2J + 1) \, dJ}$$

Fig.3 shows the FWHM (Full Width Half Maximum) of mass distribution as a function of  $\langle J \rangle$  for  $^{16}\text{O} + ^{170}\text{Yb}$  and  $^{32}\text{S} + ^{154}\text{Sm}$ <sup>5)</sup>. The FWHM of mass distribution for these two system take same value at the same  $\langle J \rangle$ . So the mass distribution is strongly dependent on the angular momentum of compound nucleus. The other systems are shown in Fig. 4.

#### References

- 1) S.M.Lee and T.Matsuse, Proceeding of International Symposium on Heavy Ion Physics, Mt. Fuji, August 27-31,1984,p272
- 2) T. Nakagawa et al.,JAERI-M 84-085 p12
- 3) B.B.Back et al.,Pys. Rev. C32(1985)195
- 4) V.E.Viola.Jr et al., Phys. Rev. C26(1982)178
- 5) B.G.Glagola et al., Phys. Rev. C29(1984)486

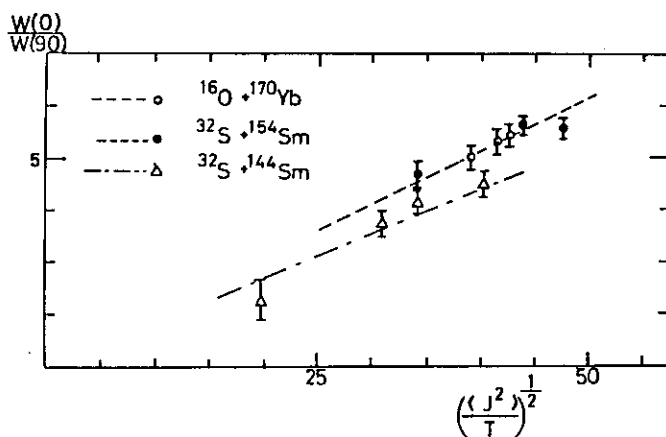


Fig.1 Anisotropy of angular distribution of fission fragments as a function of  $(\langle J^2 \rangle / T)^{1/2}$



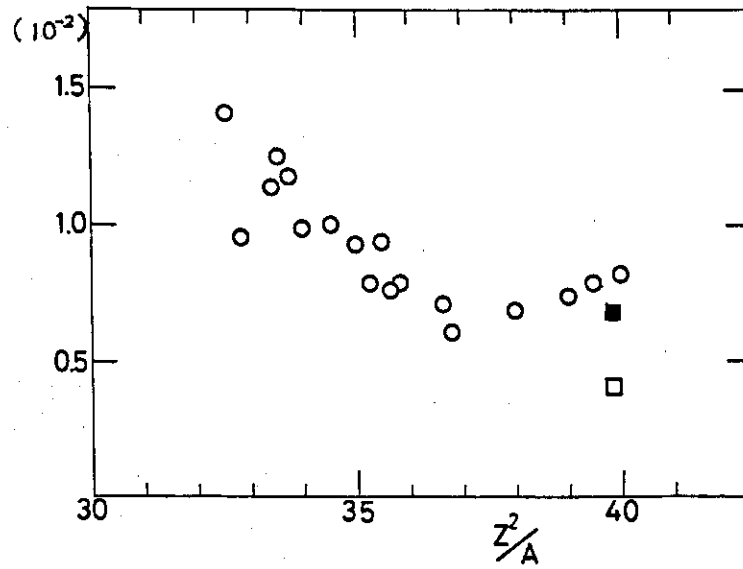


Fig.2 The value of slope for various systems as a function of  $Z^2/A$ , where A and Z are nuclear mass and charge number

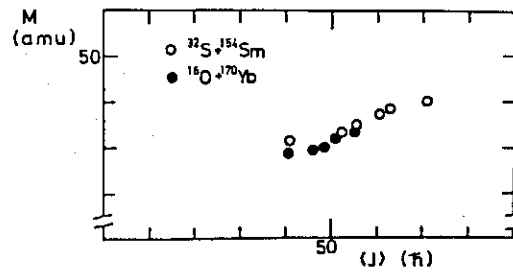


Fig.3 FWHM of mass distributions as a function of  $\langle J \rangle$

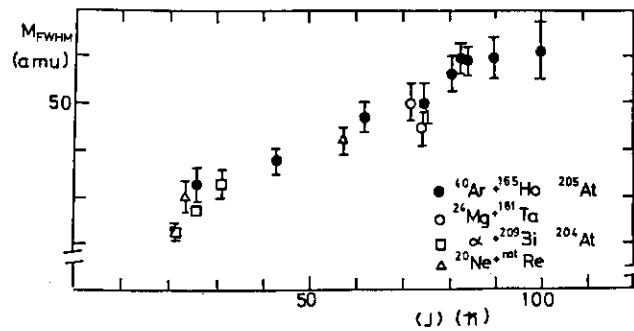


Fig.4 FWHM of mass distributions as a function of  $\langle J \rangle$

28. Coincidence Study of Damped Reaction Fragments  
for the Systems of  $^{35}\text{Cl} + ^{46}\text{Ti}$  and  $^{37}\text{Cl} + ^{48}\text{Ti}$

Kazumi Ideno

Department of Physics, Japan Atomic Energy Research Institute

In the damped reaction a large fraction of incident energy is consumed by the excitations and kinetic movements of the binary fragments from the composite system formed with the incident particle and target nucleus. We can obtain information on the transferred energies to the fragments by measuring the angular distribution of two coincident fragments and their kinetic energies. Using the JAERI tandem accelerator, we made such measurements for the systems of  $^{35}\text{Cl} + ^{46}\text{Ti}$  and  $^{37}\text{Cl} + ^{48}\text{Ti}$  at 180 and 200 MeV. We used two sets of  $\Delta E$ -E counter telescopes with ionization chambers. We combined a position-sensitive detector in one of the sets. One detector was fixed at 45 degrees; the other detector covered the range of 25 to 50 degrees.

Figure shows the examples of the measured coincident events. It is seen that for the system of  $^{35}\text{Cl} + ^{46}\text{Ti}$  a few charges are mainly missed from the coincident fragments while for the system of  $^{37}\text{Cl} + ^{48}\text{Ti}$  coincidence events with no protons missed are dominant. In the case where no protons are missed, emission of a few neutrons is expected from the statistical calculation. We can deduce most probable Q-values and half widths  $\Delta Q$  from the center position and width of the curves in the figure. More elaborate comparisons of the data are now being made.

---

The present work is a result of collaboration with Y. Tomita, H. Ikezoe, Y. Sugiyama, W. Yokota, K. Suzuki, S. Ogiwara, T. Komatsubara, S. M. Lee, and T. Mikumo.

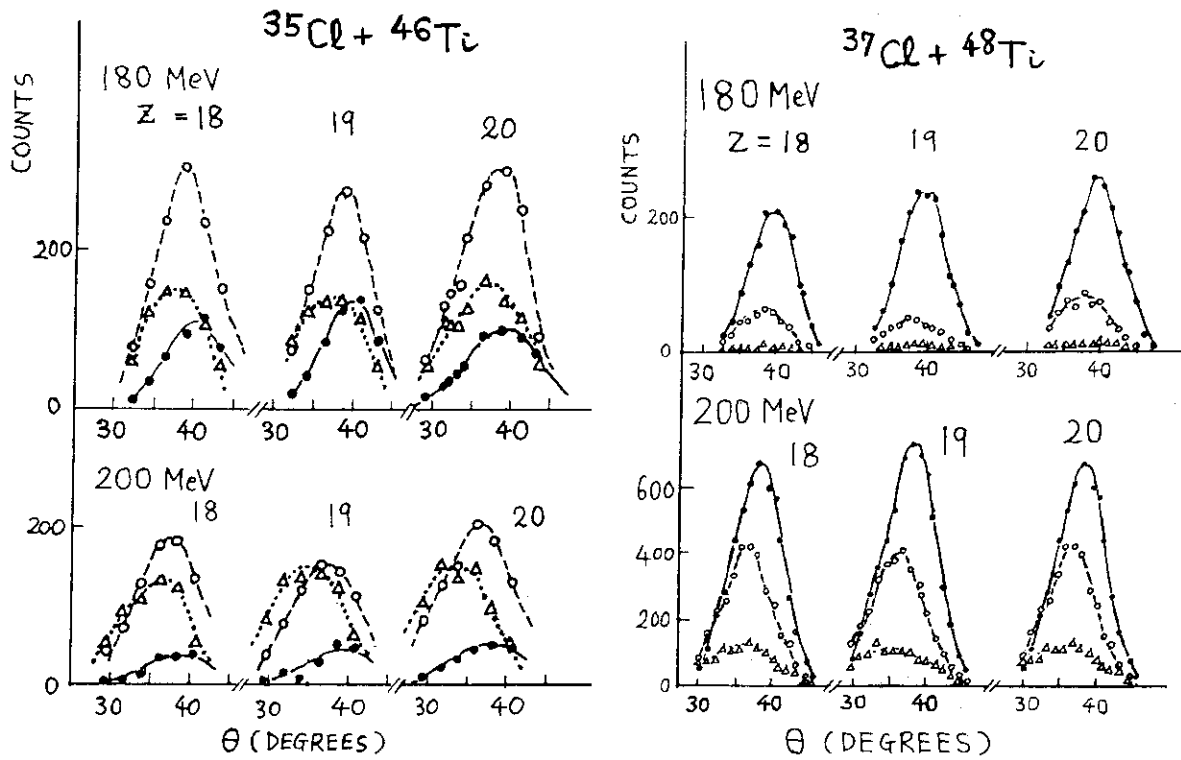


Figure: Angular distributions of coincident events for the systems of  $^{35}\text{Cl} + ^{46}\text{Ti}$  and  $^{37}\text{Cl} + ^{48}\text{Ti}$ . One detector was placed at 45 degrees and the other one was moved covering the range of 25 to 50 degrees. In the figure,  $Z$  denotes the charges of the fragments detected at the fixed angle of 45 degrees; the marks ●, ○ and Δ indicate the events with no proton missed, with one proton missed and with two protons missed, respectively.

29. Dynamical Decay of Nuclei at High Temperature:  
Competition between Particle Emission and Fission Decay

Y. Abe\*, H. Delagrange, C. Gregoire and F. Scheuter

GANIL, B.P. 5027, F-14021 Caen Cedex, France

\*RIFP, Kyoto University, Kyoto, 606, Japan

The salient features of the puzzling particle emission are the observed characteristics of an emission from a thermally equilibrated system<sup>1</sup>, even if many arguments indicated that the composite system does not have equilibrated all its degrees of freedom. To be more precise, the emitted particles present energy spectra and angular distributions compatible with a compound nucleus even if such a behavior is not expected. Coincidence measurements between charged particles and fission fragments indicated that evaporation has occurred before fission to such an extent that it can not be predicted by standard statistical decay calculations<sup>2</sup>. It would be necessary that the energy equilibration degree of freedom which allows particle evaporation when the excitation energy is high enough is relaxed more rapidly than the collective degrees of freedom leading, for example, to fission. Then, it could mean that the fission width will reach its stationary value only after a certain amount of time. Extending the pioneering work of Kramers<sup>3</sup> and Chandrasekhar<sup>4</sup>, Grangé et al.<sup>5</sup> have derived an average fission width depending explicitly on time. Subsequently a master equation involving the time-dependent fission rate was solved to follow the neutron-fission competition. They reached a fair understanding of the enhanced neutron emission for the system studied in ref. 1. They, however, did not include a cooling effect due to particle evaporation in the course of fissioning, as well as a temperature dependence of the fission barrier.

In this work, we propose a generalized diffusion equation describing the evolution of a system towards fission including the emission of particles. In other words, the new equation describes a cooling effect due to particle evaporation as well as transient effect of fission rate reaching the stationary regime.

$$\frac{\partial}{\partial t} d(Q, P, t; s) = - \frac{P}{B} \frac{\partial}{\partial Q} d + \frac{\partial U}{\partial Q} \frac{\partial}{\partial P} d$$

$$\begin{aligned}
& + \frac{\gamma}{B} \frac{\partial}{\partial P} (Pd) + \gamma T \frac{\partial^2}{\partial P^2} d \\
& + \Gamma(Q, P, s-1) \cdot d(Q, P, t; s-1) \\
& - \Gamma(Q, P, s) \cdot d(Q, P, t; s),
\end{aligned} \tag{1}$$

where the last two terms in the right-hand side are gain and loss term due to particle evaporation.  $s$  denotes number of emitted particles and hence specifies compound nucleus. All the other terms constitute the usual diffusion equation, i.e., Kramers' equation. It is readily understood in the following that this generalization is reasonable. If  $\Gamma$  does not explicitly depend on  $Q$  and  $P$ , the equation reduces to the generalized master equation including fission decay,

$$\begin{aligned}
\frac{\partial \bar{f}(t; s)}{\partial t} = & - \Gamma_f(t; s) \cdot \bar{f}(t; s) \\
& + \Gamma(s-1) \cdot \bar{f}(t, s-1) - \Gamma(s) \cdot \bar{f}(t, s),
\end{aligned} \tag{2}$$

where

$$\bar{f}(t; s) = \int_{-\infty}^{Q_s} dQ \int_{-\infty}^{\infty} dP \, d(Q, P, t; s)$$

describes compound nucleus probability for a nucleide with  $s$  particles having evaporated. Thus, the formalism by Hassani and Grangé<sup>6</sup>, where  $\Gamma_f(t; s)$  is determined independently on particle evaporation, is seen to be a particular case of our generalized transport equation.

Actually, we solve the equation (1) for the elongation coordinate leading to fission, neglecting mass asymmetry and necking degree of freedom. The potential  $U$  is simply parametrized in the following, based on the liquid-drop model<sup>7</sup>.

$$U(c) = \frac{1}{2} a(c-1)^2 + \frac{1}{6} b(c-1)^3, \tag{3}$$

where  $(a, b)$  are completely determined in terms of the saddle point parameters  $(c_s, U_B)$ . The inertia tensor  $B$  is calculated approximately by the Werner-Wheeler method<sup>8</sup> and the dissipation tensor  $\gamma$  in the one-body dissipation picture<sup>9</sup>. The initial conditions were chosen as

$$d(Q, P, t=0; s) = \delta(Q - Q_{\min}) \frac{1}{\sqrt{2\pi BT}} e^{-\frac{P^2}{2BT}} \cdot \delta(s), \quad (4)$$

where  $Q_{\min}$  is the ground-state deformation coordinate and  $T$ , the initial temperature of the compound nucleus. Further, we assume that  $d(Q, P, t; s) \propto \delta(s - s^\circ(t))$  where  $s^\circ(t)$  is an average number of emitted particle at time  $t$ , which is determined by the local ( $Q, P$  fixed) master equation.

After solving the equation (1), we calculate

- i) the particle multiplicity associated to the fission fragments:

$$\langle \nu \rangle_F = \int_0^T P_f(t, s^\circ(t)) \cdot s^\circ(t) dt \Big/ \int_0^T P_f(t, s^\circ(t)) dt, \quad (5)$$

where the fission probability  $P_f(t, s^\circ(t)) = \Gamma_f(t; s^\circ(t)) \cdot \bar{f}(t; s^\circ(t))$ ,

- ii) the "statistical model" multiplicity  $\langle \nu \rangle^{SM}$  associated to fission fragments.

$$\langle \nu \rangle^{SM} = \int_0^T P_f^{Kramers}(t, s^\circ(t)) \cdot s^\circ(t) dt \Big/ \int_0^T P_f^{Kramers}(t, s^\circ(t)) dt, \quad (6)$$

where  $P_f^{Kramers}(t, s^\circ(t)) = \Gamma_f^{Kramers}(s^\circ(t)) \cdot \bar{f}(t; s^\circ(t))$ .  $\Gamma^{Kramers}$  is a stationary rate related to Bohr-Wheeler's expression<sup>10</sup> and hence does not depend explicitly on time.

In Fig. 1 are displayed the fission widths obtained by the dynamical calculation (full line) and for the Kramers stationary solution (dotted line) as a function of the dynamical parameter  $s_n$ , number of emitted neutrons. The steep decrease of the stationary solution is due to the cooling of the system during the deexcitation process. The same behavior is observed in the solution of our dynamical equation for  $s_n$  larger than 6 units of mass. Before this stage, the full line exhibits the transient effect for fission decay. During the time needed by the fissioning system to reach the stationary regime, the mean number of emitted

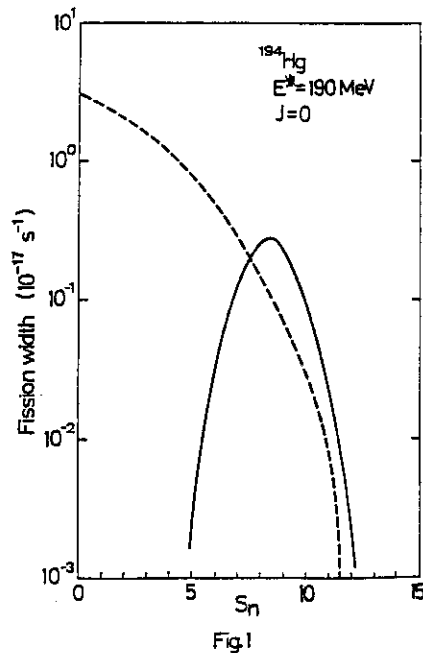


Fig 1

neutrons is equal to 6. One can expect from these dynamical characteristics (transient effect and dynamical cooling of the system) that the particle multiplicity might be larger in our calculation than in a statistical model estimate. The particle multiplicities calculated in our dynamical approach are compared to the predictions of the statistical model in Fig. 2 as a function of temperature. The statistical model multiplicities are quite small than the dynamical ones.

A twofold factor is reached at  $T=5$  MeV.

The generalized transport equation, where the usual fission collective coordinates are treated with explicit intrinsic degrees of freedom, allows to follow simultaneously the fission decay mode and the particle evaporation. As a result of taking into account the transient effect and the cooling effect dynamically, we obtained the enhancement of the particle multiplicity as compared with the statistical model calculations, which is qualitatively similar to the experimental observation.

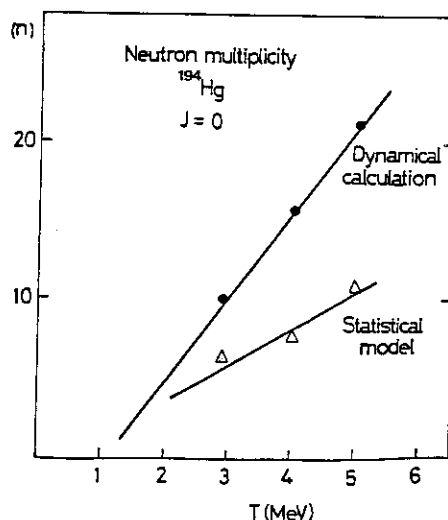


Fig.2

#### References

1. A. Gavron et al., Phys. Rev. Lett. 47, 1255 (1981) and 48, 835 (1982).
2. D. Logan et al., Nucl. Phys. A403, 189 (1983).
3. H.A. Kramers, Physica 7, 284 (1940).
4. S. Chandrasekhar, Rev. Mod. Phys. 15, 1 (1943).
5. P. Grangé et al., Phys. Rev. C27, 2063 (1983).
6. S. Hassani and P. Grangé, Phys. Lett. 137B, 281 (1984).
7. W.D. Myers and W.J. Swiatecki, Nucl. Phys. 81, 1 (1966).
8. K.T.R. Davies et al., Phys. Rev. C13, 2385 (1976).
9. A.J. Sierk and J.R. Nix, Phys. Rev. C21, 982 (1980).
10. N. Bohr and J.A. Wheeler, Phys. Rev. 36, 426 (1939).

## 30. New Approach to Pre-equilibrium Reaction Theory

Shiro Yoshida

Department of Physics, Tohoku University

Pre-equilibrium reaction theories have been extensively used in analyzing experimental data with success. However there still remain fundamental problems unsolved. First the multi-step direct and compound processes, which were introduced by Feshbach, Kerman and Koonin<sup>1)</sup>, are treated separately and no dynamical coupling is taken into account. This problem will be solved by orthogonal transformations introduced by Nishioka and Weidenmueller<sup>2)</sup>. After these transformations the eigenchannel representation takes care of the coupling, so we can work forgetting the direct processes.

Agassi, Weidenmueller and Mantzouranis<sup>3)</sup> gave the quantum mechanical derivation of transport equation for pre-equilibrium process. The Hamiltonian matrix elements which causes the transition between different classes are assumed to be random variable. However the level densities for each class, which should be obtained through the same Hamiltonian are assumed to be given independently. In phenomenological analysis the formula given by Ericson are extensively used but it is based on the independent particle model.

In phenomenological analysis the transition rates between different classes must be cut by a factor to get the agreement with the experimental data. The transition rate is calculated from the mean free path in nuclear matter. Improved level density formula is found to make the reduction factor smaller,



but still they must be reduced by a factor  $2^4$ ). The high energy part of emitted particle is underestimated by the conventional theory.

We have treated the pre-equilibrium processes using generating function and Grassmann integration. The formulation is just an extension of the statistical theory of compound nucleus by Verbaarschot, Weidenmueller and Zirnbauer<sup>6)</sup>. The matrix elements of the Hamiltonian are assumed to be random variable and their distribution function is given by the Gaussian Orthogonal Ensemble(GOE). Their second moment is assumed to be given, and the matrix element with respect to the class is denoted by  $M_{mn}$ . The matrix  $M_{mn}$  is assumed to have an inverse. The one point and two point function of S-matrix, namely  $\overline{S(E)}$  and  $\overline{S(E)S^*(E)}$  are calculated under the following conditions

(1) The number of levels in each class  $N_m$  is much larger than 1.

(2) The escape width for each class are much larger than the level distance in each class. The calculations are carried out without further approximation. There are two cases, both of which are thought to correspond to the pre-equilibrium process.

(1) weak coupling

$$M_{mn}/M_{mm} \longrightarrow 0 \quad \text{as } N_m \longrightarrow \infty$$

(2) strong coupling

$$M_{mn}/M_{mm} \longrightarrow \text{finite(small)} \quad \text{as } N_m \longrightarrow \infty$$

In the case of the weak coupling the resulting expression is same as obtained by AWM<sup>3)</sup>. The different treatment of the level densities does not give any differences. In the case of the strong coupling limit the obtained formula has the same form as the one given by AWM. Each terms in both methods can be

identified. However there is one exception, which is the level density. In our new results, the so-called effective level density corresponds to the level density in AWM. However the effective level density has the dimension of the level density, but it does not correspond to the physical level density. The structure of the two point functions are same in weak and strong coupling cases, and if the weak coupling limit is taken in the strong coupling expression the weak coupling results are obtained. The effective level density reduces to the physical level density.

We can also obtain the compound nucleus results by taking a limit. In the weak coupling case the escape width is taken to be very small, then the system has a long lifetime and reach to the equilibrium. In the case of strong coupling if the limit is taken where the second moment  $M_{mn}$  is independent of  $m, n$ , the mixing of classes are taken place and the equilibrium is realized.

In the case of strong coupling we made a simple calculation of level density in two classes. The effective level density deviates from the unperturbed level density, which has the semi-circle form. If the threshold energies are assumed to be same, the level density for the lower class is enhanced near the threshold energy, and this may explain the enhancement of the high energy tail of the energy spectra mentioned earlier.

Our calculations are carried out assuming the second moments  $M_{mn}$  as inputs. However  $M_{mn}$  can not be obtained from the experimental data but should be calculated by using the average of square of the two body matrix elements and level densities. In the zero-th order approximation ref.<sup>7)</sup> gave the formula.

But we don't know the level density before. So we have to do a self-consistent determination of the level density and the second moments. These problems are not yet solved.

#### References

- 1) H.Feshbach, A.K.Kerman and S.Koonin; Ann.Phys.(N.Y) 125(1980) 429
- 2) H.Nishioka and H.A.Weidenmueller; Phys.Lett. 157B(1985) 101
- 3) D.Agassi, H.A.Weidenmueller and G.Mantzouranis, Phys. Lett. 22c (1975) 145
- 4) J.M.Akkermans and H.Gruppelaar; Z.Phys. A321 (1985) 605
- 5) H.Nishioka, J.J.M.Verbaarschot, H.A.Weidenmueller and S.Yoshida; preprint
- 6) J.J.M.Verbaarschot, H.A.Weidenmueller and M.K.Zirnbauer; to be published in Phys.Rep.
- 7) E.Gadioli, E.Gadioli-Erba and P.G. Sona; Nucl.Phys. A217 (1973) 589

### 31. Anomalous Properties of Spontaneous Fission in Heavy-Actinide Nuclides

Ichirō Fujiwara

Institute of Atomic Energy, Kyoto University

#### (1) Introduction

In the spontaneous fission (SF) of actinide isotopes the mass distributions are generally asymmetric. The lighter isotopes of fermium follow this rule up to  $^{257}\text{Fm}$ . The nuclei  $^{258}\text{Fm}$  and  $^{259}\text{Fm}$ , however, exhibit symmetric mass distribution in SF; in addition the total kinetic energies (TKE) released are anomalously high. It is astonishing that a drastic change from asymmetric to symmetric fission is caused by addition of only one neutron to such a huge nucleus as actinide. This phenomenon is not easily understood with current fission theories. A recent observation on the SF of  $^{259}\text{Md}$  is further puzzling because its mass distribution is highly symmetric but it is accompanied with a TKE much lower than those of  $^{258,259}\text{Fm}$ . In this paper, experimental results of SF of heavy actinides are reviewed briefly.

#### (2) Anomalous Fission Properties of $^{258}\text{Fm}$ and $^{259}\text{Fm}$

The first finding of an anomalous property of SF in heavy actinides was an extremely short life of  $^{258}\text{Fm}$ . Hulet et al.<sup>1)</sup> produced the  $^{258}\text{Fm}$  nucleus by the  $^{257}\text{Fm}(d,p)^{258}\text{Fm}$  reaction and found that this nucleus decays entirely by SF with a half-life of  $380 \pm 60 \mu\text{sec}$ . This very short life compared with 100.5 day for  $^{257}\text{Fm}$  is ascribed to the general trend of the increased instability of even-even nuclei in the region beyond  $N=158$ . Then John et al.<sup>2)</sup> investigated the mass and kinetic energy distributions of fission of  $^{258}\text{Fm}$  using the  $^{257}\text{Fm}(n,f)$  reaction in a thermal column of a reactor. The mass distribution obtained was symmetric as shown in Fig.1,<sup>2)</sup> and the TKE was as high as 233 MeV. The SF of  $^{259}\text{Fm}$  produced by the  $^{257}\text{Fm}(t,p)^{259}\text{Fm}$  reaction was also found to be symmetric fission with a narrow width of mass distribution<sup>3)</sup> as shown in Fig.2; it was associated with a TKE as high as 242 MeV.<sup>3)</sup>

A possible explanation for the symmetric SF of  $^{258}\text{Fm}$  and  $^{259}\text{Fm}$  is given as follows. In the Strutinsky-type calculation<sup>4)</sup> for the lighter actinides, a low energy path appears around the second hump of fission

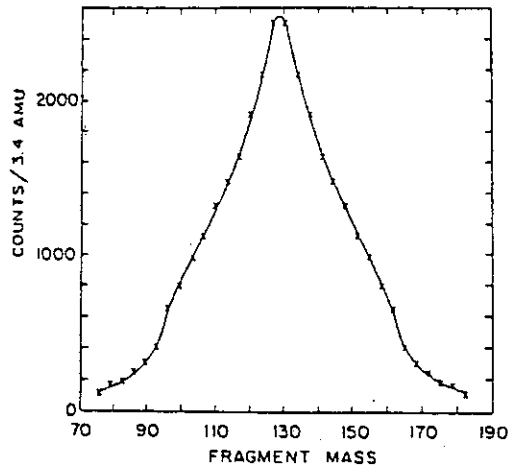


Fig.1 Mass distribution for the fission of  $^{258}\text{Fm}$ .

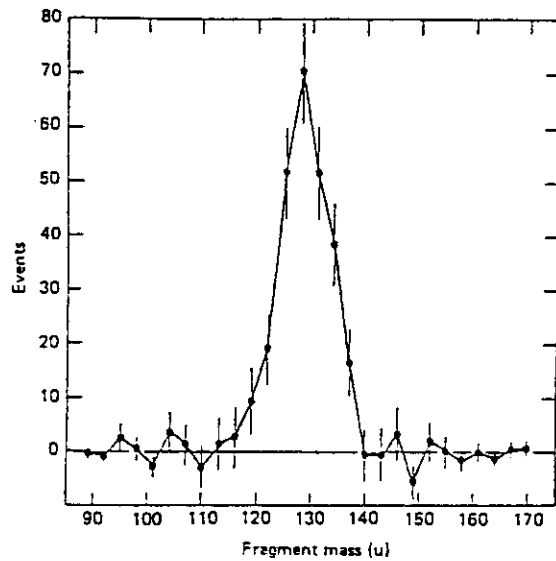


Fig.2 Mass distribution for the fission of  $^{259}\text{Fm}$ .

barrier when an asymmetric drop distortion is introduced. For the heavy actinides, the calculated second hump is decreasing with increasing masses. The SF of  $^{257}\text{Fm}$  is qualitatively explainable by assuming that for a long time the system goes around the second hump with asymmetric distortion, after all resulting in asymmetric fission. In the case of the low second hump, however, sometimes the system tunnels or goes directly through with symmetric distortion. This is applicable to the SF of  $^{258}\text{Fm}$ , because the system is found from calculation to be excited above the second hump. This explanation is supported by the extensive calculations of Pauli et al.<sup>5)</sup> and Gustafsson et al.<sup>6)</sup> From the calculations, the transition from asymmetric to symmetric mass division for even-even nuclei is expected to occur around  $N=160$ .

The SF of  $^{252}\text{No}$  and  $^{262}\text{105}$ , whose atomic numbers are higher and neutron numbers are smaller than  $^{258}\text{Fm}$ , were both found to be asymmetric.<sup>7,8)</sup> Low energy fission properties of some isotopes<sup>9)</sup> are shown in Table 1, and the systematics for TKE in SF of Cm through No<sup>9)</sup> is shown in Fig.3. All the experimental TKE values except those of  $^{258}\text{Fm}$  and  $^{259}\text{Fm}$  fit the systematic trend of Viola<sup>10)</sup> (solid line in Fig.3).

The unusually high kinetic energies associated with the symmetric fission of  $^{258}\text{Fm}$  and  $^{259}\text{Fm}$  are probably related to the proximity of the fragment nucleon numbers  $Z=50$  and  $N=82$ . These nearly doubly magic

Table 1 Low energy fission properties of some heavy-element isotopes.

Nuclide	SF $T_{1/2}(s)$	Mass distribution	TKE(MeV)
$^{250}\text{Cf}$	$5.4 \times 10^{11}$	Asymm.	187.0
$^{252}\text{Cf}$	$2.7 \times 10^9$	Asymm.	186.1
$^{254}\text{Cf}$	$5.2 \times 10^6$	Asymm.	186.9
$^{256}\text{Cf}$	$7.4 \times 10^2$	Asymm.	189.8
$^{254}\text{Fm}$	$2.0 \times 10^7$	Asymm.	195.1
$^{256}\text{Fm}$	$1.0 \times 10^4$	Asymm.	197.9
$^{257}\text{Fm}$	$4.1 \times 10^9$	Asymm.	197.6
$^{258}\text{Fm}$	$3.8 \times 10^{-4}$	Symm.	238
$^{259}\text{Fm}$	1.5	Symm.	242
$^{259}\text{Md}$	$6.2 \times 10^3$	Symm.	201.9
$^{252}\text{No}$	8.6	Asymm.	202.4
$^{262}_{105}$	$4.2 \times 10$	asymm.	

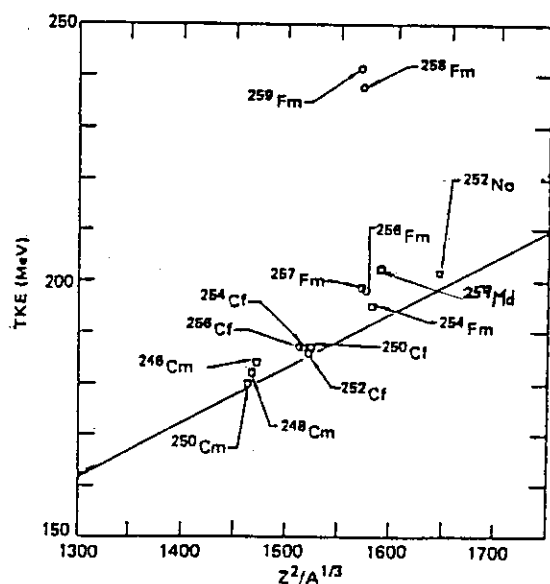


Fig.3 Systematics of TKE for SF of Cm through No isotopes.

fragments will be more resistant to deformation; hence relatively the less energy will go into excitation, the fewer neutrons will be emitted, and the more energy will go into the kinetic energy.

### (3) Low Fragment Kinetic Energy in the Symmetric Fission of $^{259}\text{Md}$

The 103-min isotope  $^{259}\text{Md}$  decays by SF, with symmetric mass distribution like  $^{258}\text{Fm}$  and  $^{259}\text{Fm}$ .<sup>11)</sup> The total kinetic energy distribution is, however, broader than those of  $^{258}\text{Fm}$  and  $^{259}\text{Fm}$ . Further-

more, the most probable TKE of 202 MeV is about 40 MeV lower than those of SF of  $^{258}\text{Fm}$  and  $^{259}\text{Fm}$ . There was a doubt that some energy was missing due to the emissions of light hydrogen-like particles at scission in a

large fraction of the  $^{259}\text{Md}$  SF, but this hypothesis seems to be unfounded. The total kinetic energy deficit at mass symmetry must be distributed between internal excitation and deformation energies at scission. But this has not been proved experimentally.

It is indispensable to investigate experimentally the SF properties of nuclei with neutrons more than 159 toward fully understanding the anomalies. The JAERI Tandem Accelerator facilities would be usable for the study.

#### References

- 1) E.K.Hulet et al., Phys. Rev. Lett., 26(1971)523.
- 2) W.John et al., Phys. Rev. Lett., 27(1971)45.
- 3) E.K.Hulet et al., Phys. Rev., C21(1980)966.
- 4) V.M.Strutinsky, Nucl. Phys. A122(1968)1.
- 5) H.C.Pauli et al., Phys. Lett., 34B(1971)264.
- 6) C.Gustafsson et al., Phys. Lett., 34B(1971)349.
- 7) C.E.Bennis et al., Phys. Rev., C15(1977)705.
- 8) C.E.Bennis et al., Phys. Rev. Lett., 39(1977)1246.
- 9) D.C.Hoffman et al., Phys. Rev., C21(1980)972.
- 10) V.E.Viola, Jr., Nuclear Data, A1(1966)391.
- 11) J.Wild et al., Phys. Rev., C26(1982)1531.

32. Decay properties of light einsteinium isotopes ( $A \leq 247$ )

Yuichi Hatsukawa, Masaaki Magara, Tsutomu Ohtsuki, Keisuke Sueki

Hiromichi Nakahara and Isao Kohno\*

Department of Chemistry, Tokyo Metropolitan University, \*Cyclotron Laboratory  
The Institute of Physical and Chemical Research.

By using heavy ion reactions, we produced neutron-deficient einsteinium isotopes and investigated their decay properties. As reaction systems, we chose  $^{14}\text{N} + ^{238}\text{U}$  and  $^{12}\text{C} + ^{237}\text{Np}$ , and einsteinium isotopes with  $A \leq 247$  were investigated by means of  $\alpha$ -ray spectroscopy.

Mikheev et al.<sup>1)</sup> first reported in 1967 that by the  $^{238}\text{U}(^{14}\text{N}, \text{xn})$  reaction  $^{245}\text{Es}$ ,  $^{246}\text{Es}$ , and  $^{247}\text{Es}$  were synthesized; their  $\alpha$ -particle energies were 7.70, 7.33, and 7.33 MeV, and their half-lives were 1.33, 7.7, and 5.0 min, respectively. Later in 1972, by the reaction of  $^{241}\text{Am} + ^{12}\text{C}$ , Eskola<sup>2)</sup> produced and identified  $^{245-247}\text{Es}$  which decayed by electron capture and  $\alpha$ -emission. He reported that the  $\alpha$ -particle energies of  $^{245}\text{Es}$ ,  $^{246}\text{Es}$ , and  $^{247}\text{Es}$  were 7.73, 7.36, and 7.31 MeV, respectively, and the half-life of  $^{247}\text{Es}$  was 4.7 min. Since there are only a few reports on those isotopes, we first investigated their decay characteristics and then excitation functions.

We produced neutron-deficient isotopes of Es by bombarding a  $^{238}\text{U}$  target with  $^{14}\text{N}$  ions and a  $^{237}\text{Np}$  with  $^{12}\text{C}$  ions at the cyclotron. Beam energies were  $E_{\text{lab}}(^{14}\text{N}) = 80 - 103$  MeV and  $E_{\text{lab}}(^{12}\text{C}) = 67 - 81$  MeV. The reaction products recoiled out of the targets were stopped in a fast flowing He gas (a He-jet system<sup>3)</sup>), and transferred onto the collecting tape heated at 195 °C in order to get rid of the oil that would deteriorate the resolution of alpha spectra. After an appropriate collection period (generally 8 or 3 min), the deposit recoil atoms were moved to face Si(Au) surface barrier detectors for  $\alpha$ -ray measurements.  $\alpha$ -Decay events were recorded together with external clock pulses and stored in a magnetic tape in the list mode for data analysis.

The  $\alpha$ -particle spectra displayed in Fig.1 are the sum of the results obtained by several bombardments of the  $^{238}\text{U}$  with 80 - 103 MeV  $^{14}\text{N}$  ions. The peak profile and energy calibration were determined by using  $\alpha$ -rays of  $^{211}\text{mPo}$ ,  $^{213}\text{Fr}$ , and  $^{214}\text{Ra}$  produced by separate bombardment of a  $^{209}\text{Bi}$  target with  $^{14}\text{N}$ . The  $\alpha$ -peaks at 7.73, 7.36, and 7.32 MeV have been assigned to  $^{245}\text{Es}$ ,  $^{246}\text{Es}$ , and  $^{247}\text{Es}$ , respectively. Some other  $\alpha$ -peaks were also observed, which, from their energies and half-lives, could not be assigned



to some of the nuclei produced by  $^{14}\text{N}$  on Bi or Pb, possibly included in the  $^{238}\text{U}$  target as impurities, or those produced by transfer reaction of  $^{238}\text{U}$ . Further, by the comparison of the excitation functions of each  $\alpha$  peak with those of the known  $\alpha$ -rays, it is concluded that all the peaks but 7.11, 7.47 and 7.52 MeV  $\alpha$ -rays belong to the Es isotopes produced by  $^{238}\text{U}$  ( $^{14}\text{N}, \text{xn}$ )  $^{252-x}\text{Es}$  reactions. (The 7.11 MeV  $\alpha$  peak is assigned to the decay of  $^{245}\text{Cf}$ .)

They could be grouped according to their half-lives and the projectile energy dependence as presented in Table 1. The errors attached to relative intensities merely reflect statistical uncertainties in counting, and those given for  $\alpha$ -particle energies are mostly caused by energy calibration. The preliminary results suggest that  $^{245}\text{Es}$  emits three different  $\alpha$ -rays, and that  $^{246}\text{Es}$  has two isomer state, one of which emits four and the other two  $\alpha$ -rays. More complete and quantitative discussions of level schemes may, however, become possible only after measurements of  $\gamma$ -rays in coincidence with  $\alpha$ -particles.

In order to confirm the above results, bombardments of a  $^{237}\text{Np}$  target with 67 - 81 MeV  $^{12}\text{C}$  ions were performed. The obtained spectra are shown in Fig. 2.  $\alpha$ -Rays belonging to  $^{245}\text{Es}$  were mainly observed. Rough estimate of their half-lives are in good agreement with those obtained in the  $^{14}\text{N} + ^{238}\text{U}$  reaction.

#### References

- 1) V.L. Mikheev, V.I. Ilyuschnko and M.B. Miller: Sov. J. Nucl. Phys., 5, 35, (1967).
- 2) P. Eskola: Phys. Rev., C7, 280 (1973).
- 3) H. Kudo, T. Nomura and J. Fujita: RIKEN Accel. Progr. Rep., 17, 127 (1983).

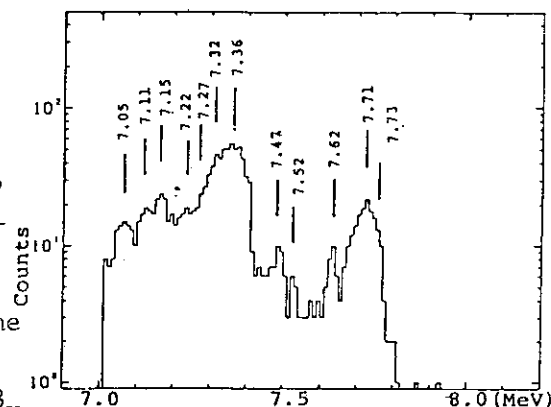


Fig. 1 A part of the  $\alpha$ -particle spectra. Sum of the results of five bombardments of  $^{238}\text{U}$  with 80 - 94 MeV  $^{14}\text{N}$  ions.

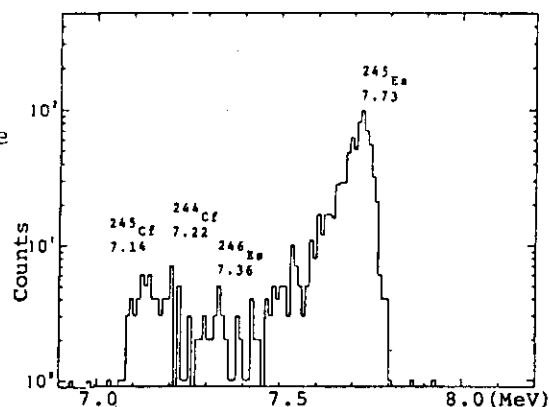


Fig. 2 A part of the  $\alpha$ -particle spectra produced by bombardments of  $^{237}\text{Np}$  with 71 MeV  $^{12}\text{C}$  ions.

Table 1 Summary of experimental results.

Nuclide	Energy (MeV)	Half-life (min)	Branching Ratio
$^{247}\text{Es}$	7.32	$5.24^{+0.52}_{-0.43}$	
$^{246}\text{Es}$	7.05	$4.70^{+0.72}_{-0.55}$	
	7.22	$3.15^{+0.33}_{-0.27}$	0.15
	7.36	$3.20^{+0.80}_{-0.50}$	1.00
$^{246}\text{Es}$	7.15	$7.43^{+1.90}_{-1.26}$	0.99
	7.27	$7.73^{+0.92}_{-0.75}$	1.00
$^{245}\text{Es}$	7.62	$1.18^{+0.27}_{-0.18}$	0.34
	7.71	$1.37^{+0.34}_{-0.23}$	1.00
	7.73	$1.22^{+0.14}_{-0.11}$	0.82

## 33. Ion Exchange Separation of Short-lived Transplutonium Nuclides

Shigekazu Usuda<sup>\*</sup>, Hideki Yoshikawa<sup>\*\*</sup> and Nobuo Shinohara<sup>\*</sup>

<sup>\*</sup> Department of Chemistry, Japan Atomic Energy Research Institute,

<sup>\*\*</sup> Department of Chemistry, Tokyo Metropolitan University

The transplutonium nuclides synthesized by heavy-ion bombardments frequently have short half-lives with small formation yields and emit alpha particles. In order to identify such nuclides, it is necessary to perform rapid separation with high chemical yield followed by immediate source preparation for alpha spectrometry. When the transplutonium nuclides are of electron capture decay, the detection becomes more difficult than that of alpha decay. These nuclides must be purified from fission products and the other reaction products with considerably high decontamination factor.

Novel rapid ion exchange separation methods for the transplutonium elements have been developed by using mineral acid-alcohol mixed media at elevated temperature and pressure.

#### Mutual Anion Exchange Separation

Adsorbability of transplutonium elements on anion exchange resin in nitric acid-methyl alcohol mixed media at 90°C has been investigated in detail as a function of the medium compositions by the pressurized column method<sup>1)</sup>. The results show that Am, Cm and Cf can be mutually separated by use of a very small volume column (0.025 ml) within 20 minutes.

The procedure was applied to separation of the transplutonium elements synthesized by the  $^{12}\text{C} + ^{242}\text{Pu}$  reaction<sup>2)</sup>. The individual transplutonium elements were rapidly isolated from an Al matrix (a catcher

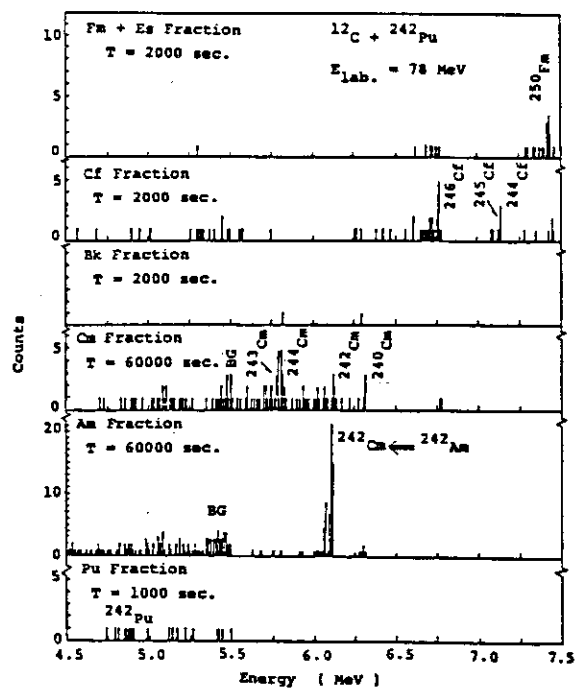


Fig.1 Alpha-ray spectra of each actinoid fraction.

foil), followed by immediate counting source preparation. Figure 1 shows the alpha spectra of each actinoid fraction.  $^{250}\text{Fm}$ ,  $^{244-246}\text{Cf}$  and  $^{240-244}\text{Cm}$  were detected in the corresponding fractions.  $^{242}\text{Cm}$  was also detected from the Am fraction, which means that  $^{242}\text{Am}$  was formed by the reaction and then decayed to  $^{242}\text{Cm}$ .

#### Effective Anion Exchange Separation of Bk, Cf and Fm

Hydrochloric acid-alcohol mixed media are specific for separation of transcurium elements from macro amounts of uranium target. Californium can be efficiently separated from Am, Cm, main fission products, Al and U in several drops of eluent with more than 95% chemical yield<sup>1)</sup> (see Fig.2). In addition, the source suitable for alpha spectrometry could be prepared simply by direct drop-evaporation.

$^{250}\text{Fm}$  and  $^{246}\text{Cf}$  synthesized by the  $^{12}\text{C} + ^{242}\text{Pu}$  or  $^{16}\text{O} + ^{238}\text{U}$  reaction<sup>3)</sup> behave similarly in 0.5M HCl-90%  $\text{CH}_3\text{OH}$  solution. This procedure can consequently be employed in an effective separation

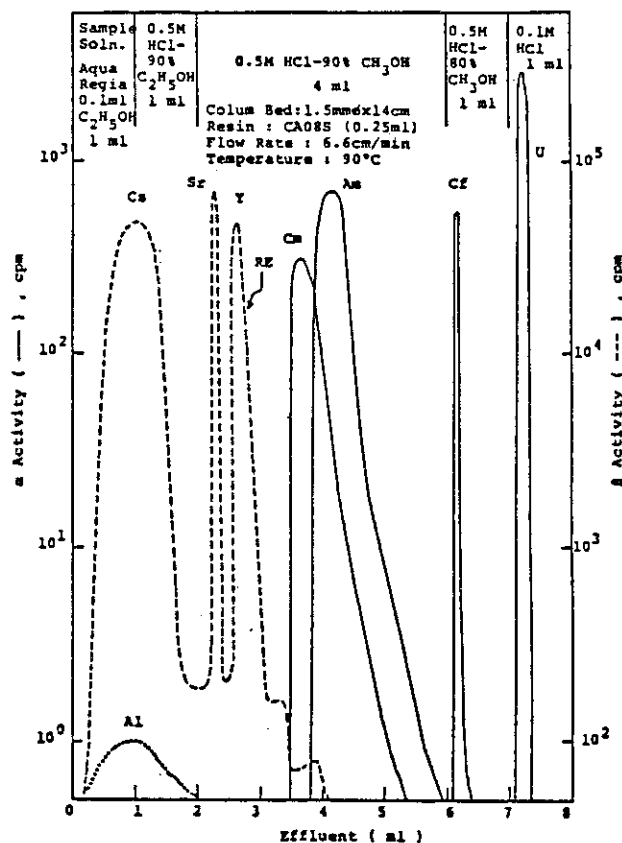


Fig.2 Effective separation of Cf from Am, Cm, fission products and macro amounts of Al and U.

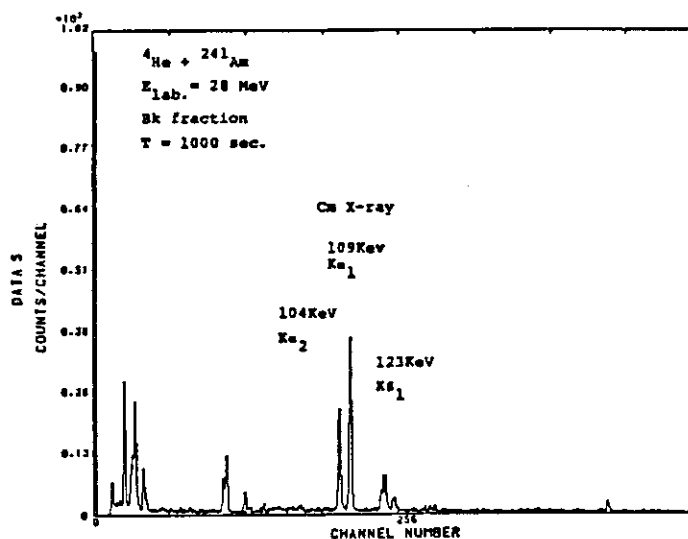


Fig.3 X-ray spectrum of  $^{243}\text{Bk}$  to  $^{243}\text{Cm}$ .

of Fm and Cf from the other elements, as shown in Fig.2.

Adsorbability of Bk is intermediate between those of the Am+Cm and the Cf+Fm fractions, so that it is possible to isolate Bk. The X-ray spectrum of  $^{243}\text{Bk}$  ( $T_{1/2} = 4.5$  hr.) produced by the  $^4\text{He} + ^{241}\text{Am}$  reaction is shown in Fig.3. The time taken the isolation and the source preparation is within 8 minutes. This procedure was also applied to separation of  $^{242}\text{Bk}$  ( $T_{1/2} = 7$  min.).

#### Development of On Line Chemical Separation System

The on line chemical separation system has been devised and attached to the R-2 beam line of the JAERI Tandem Accelerator. The system is composed of a gas-jet transporter, a tape collector, chemical separators and activity measurement apparatus. The chemical separation is performed by a continuous solvent extractor (SISAK system<sup>4)</sup>) and an ion exchange separator which has been designed to practice the rapid separation as described above.

The short-lived transplutonium nuclides, which are synthesized by the JAERI Tandem Accelerator, will be investigate using this system.

#### References

- 1) S.Usuda, to be published.
- 2) N.Shinohara, S.Usuda, S.Ichikawa, T.Suzuki, H.Okashita, H.Yoshikawa, Y.Iwata, T.Horiguchi, Y.Yoshizawa, S.Shibata and I.Fujiwara, JAERI-M 85-104 (1985) 129.
- 3) N.Shinohara, S.Ichikawa, S.Usuda, T.Suzuki, H.Okashita, T.Sekine, K.Hata, T.Horiguchi, Y.Yoshizawa, S.Shibata, I.Fujiwara, Americium and Curium Chemistry and Technology, N.M.Edelstein et al. (eds.), D.Reidel Publishing Company, Dordrecht, 251 (1985).
- 4) G.Skarnemark, P.O.Aronsson, K.Broden, J.Rydberg, T.Bjornstad, N.Kaffrell, E.Stender and N.Trautmann, Nucl. Instr. and Meth. 171 (1980) 323.

## 34. Radioisotope Beam Production at GANIL

Y.Gono, K.Hatanaka, R.Bimbot<sup>\*</sup>, P.Aguer<sup>\*\*</sup>,  
 G.Bastin<sup>\*\*</sup>, R.Anne<sup>\*\*\*</sup>, H.Delagrance<sup>\*\*\*</sup>,  
 and Y.Schuz<sup>\*\*\*</sup>

RIKEN, IPN-Orsay(\*), CSNSM-Orsay(\*\*), GANIL(\*\*\*)

Recent progress of accelerator technology gives us possibilities to use radioisotopes as secondary beams. The developments of radioisotope beams ( RIB ) are much expected<sup>1)</sup> in various research fields such as astrophysics, solid state physics, biology, medical field as well as nuclear physics. In nuclear physics it is rather straight forward to use them as extensions of standard nuclear physics.

RIB production experiments were performed at GANIL as one of the RIKEN-IN2P3 ( FRANCE ) collaboration programs. The primary beam used was 65 MeV/A <sup>18</sup>O from GANIL. Achromatic beam transport system LISE<sup>2)</sup> which consists of essentially two dipole magnets was used to separate secondary beams from the primary one. Targets, a degrader and detectors used in the experiment are listed in table 1. An example of  $\Delta E$ -E spectra is shown in fig.1. Also shown in fig.1 is a <sup>16</sup>C spectrum which was obtained by setting a degrader and adjusting the magnetic field to select

Targets

	Be mg/cm <sup>2</sup>	Al mg/cm <sup>2</sup>	Ni mg/cm <sup>2</sup>	$\Delta E$ MeV/A
A	589	621.5	748	15
B	1036	1138	1351	31.4

Degrader

134.8	142.7	150.8	158.5	166.4 mg/cm <sup>2</sup>
Al				
7.9 mg/cm <sup>2</sup> steps				

Si detectors

$\Delta E$	500 $\mu$ m x 300 mm <sup>2</sup>
E	5000 $\mu$ m x 300 mm <sup>2</sup>

Table 1

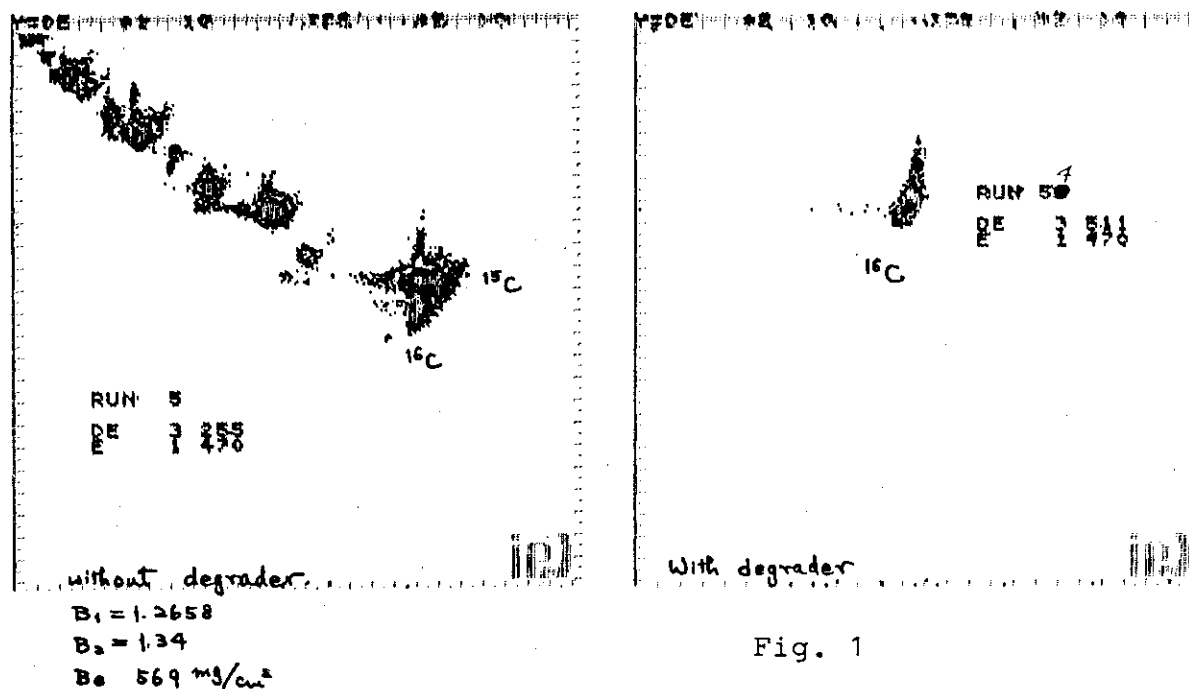


Fig. 1

$^{16}\text{C}^{6+}$  ions. It was found that the yield of  $^{16}\text{C}$  was the largest with Be target comparing with the Al and Ni targets if the target thicknesses are chosen to give the same energy loss for the reaction product  $^{16}\text{C}$ . The relative yields of  $^{14}\text{C}$ ,  $^{15}\text{C}$ ,  $^{16}\text{C}$  in this experiment is shown in fig.2. The largest yield of  $^{16}\text{C}$  was  $10^6$  particles/sec (pps) when the primary beam ( $^{18}\text{O}$ ) intensity was  $2\text{e}\mu\text{A}$ .

In the second experiment, a trial of the production of neutron rich isotopes by multi-nucleon transfer reactions was made using  $^{39}\text{Cl}$  ( $T_{1/2} = 55.6 \text{ m.}$ ) beam which was produced by the  $60.5 \text{ MeV/A } ^{40}\text{Ar}$  beam.

The beam intensity of  $^{39}\text{Cl}$  was  $10^6$  pps. Primary and secondary targets used were  $424 \text{ mg/cm}^2$  Be and  $300 \text{ mg/cm}^2$  Ho, respectively. If  $Q_{gg}$  systematics<sup>3)</sup> works at this

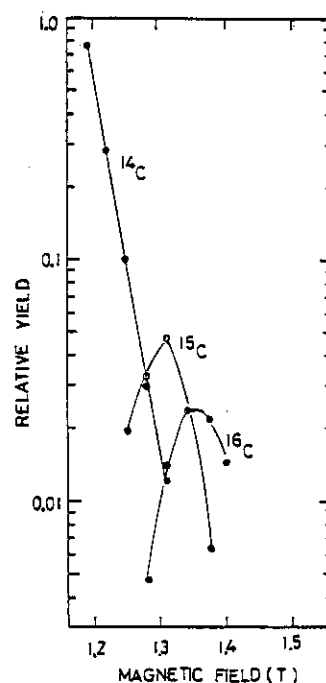


Fig. 2

energy,  $^{39}\text{Cl}$  induced reaction should give about  $10^3$  times better S/N ratio than the  $^{40}\text{Ar}$  induced one. The experiment was done using HPGe and LEPS detectors and a target rotation system. An X-ray spectrum is shown in fig.3. The  $\gamma$ -ray spectrum taken in coincidence with Dy and Tb X-rays is shown in Fig.3. Many  $\gamma$ -rays were identified as from the  $\beta$ -decays of neutron deficient Ho isotopes. It was possible to identify reaction products from the 3-10n emission channels. The gamma ray yields depend strongly on the cycle time of the target rotation and life times of activities. Data analysis is still in progress. The optimization of the condition for the neutron rich nuclei will be made in the next experiment.

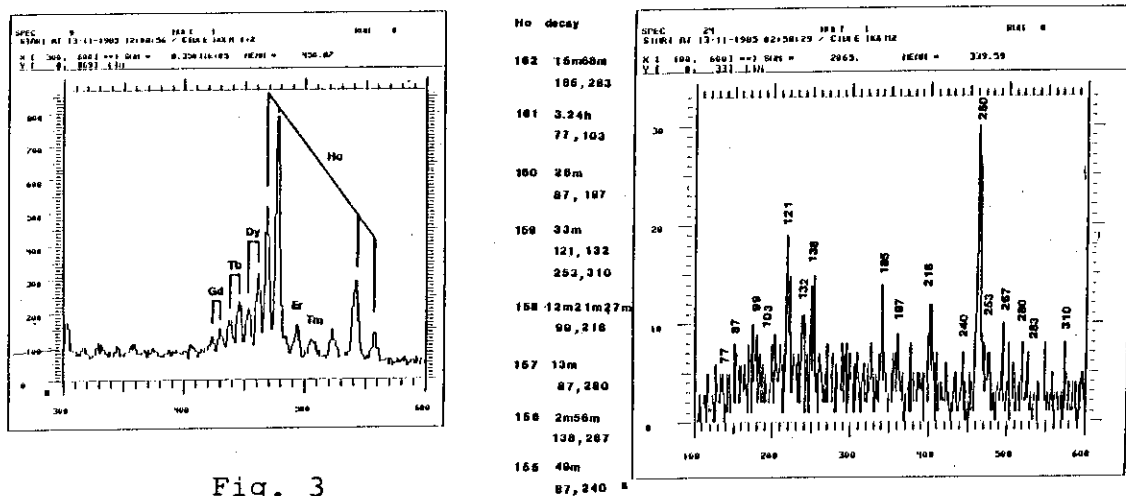


Fig. 3

## References:

1. For example, Proc. Workshop on Prospects for Research with Radioactive Beams from Heavy Ion Accelerators, ed. J.M.Nitschke, Washington DC (1984).
2. M.Langevin and R.Anne, Proc. Int. Conf. on Instrumentation for Heavy Ion Nuclear Research, ed. D.Shapira, Oak Ridge (1984) p.191.
3. A.G.Artukh, V.V.Avdeichikov, J.Ero, G.F.Gridnov, V.L.Mikheev, V.V.Volkov and J.Wilczinski, Nucl.Phys. A160(1971)511.

### 35. Nucleus-Nucleus Scattering and the Interaction Radii of Stable and Unstable Nuclei

H. Sato

Institute for Nuclear Study, University of Tokyo

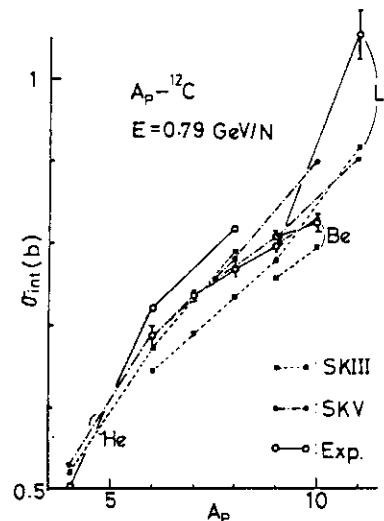
The determination of nuclear size is one of the most important problem in nuclear physics. Thus far various experimental methods (Coulomb displacement energy, high energy electron scattering, X-rays from the muonic atom and pion, proton and alpha scatterings) have been employed to determine the nuclear size. However, due to the experimental restriction on the choice of the target, these measurements are thus far limited to the case of stable nuclei. Recently Tanihata et al (INS-LBL Collaborations) have succeeded in determining the interaction cross sections for light stable and unstable nuclei and stable target nucleus scatterings with the use of secondary isotope beams produced by the Bevalac primary beam.<sup>1,2)</sup> To answer the question whether these interaction cross sections measured indicate the nuclear radii of stable and unstable nuclei, we study the interaction cross section by performing the Glauber model calculation.<sup>3)</sup> We employ the Hartree Fock (HF) type variational method to derive the nuclear density distribution of both closed shell and the middle of shell nuclei, which have been undertaken by Yazaki in the study of the systematics of the core and single particle properties of the sd shell nuclei and Ca isotopes<sup>4)</sup>, and perform the center of mass corrected Glauber model calculation<sup>5)</sup> including terms up to second order in the nucleon-nucleon (NN) profile function evaluated with the Slater determinant.

We find that the experimental interaction cross sections measured by INS-LBL collaboration are nicely reproduced as shown in Fig.1. Assuming a simple formula  $\pi R^2$  for the cross section, we compare those cross sections with the radial distribution of the matter density, and find that the interaction cross sections correspond to the position at about 40% of the central matter density of  $^4\text{He}$  nucleus and at about 30% of those of other nuclei. The corresponding  $R$  is close to the rms matter radius, while there exists small difference between them. We also find that these cross sections nicely satisfy the additivity relationship, which have been suggested by Tanihata et al<sup>1)</sup> as follows

$$\sigma_{\text{int}}(p, t) = \pi (R_p + R_t)^2. \quad (1)$$

Here  $R_p$  and  $R_t$  are respectively the interaction radii of the projectile and target nuclei, which are defined by the interaction cross sections of identical nuclei, in such a way that

Fig. 1. The interaction cross sections for the nucleus ( $A_p$ )- $^{12}\text{C}$  scatterings at 0.79 GeV/N calculated with the SKIII and SKV interactions and the experimental values measured by INS-LBL Collaboration [1]. The solid line with open circles is for the experimental values, the dotted line with solid squares is for the SKIII interaction, and the dash-dotted with solid circles is for the SKV interaction.





$$R_p = \sqrt{\sigma_{\text{int}}(p,p)/4} \quad \text{and} \quad R_t = \sqrt{\sigma_{\text{int}}(t,t)/4} . \quad (2)$$

The additivity relationship for  $^{56}\text{Fe}$ -nucleus interaction cross sections at 1.88 GeV/n are summarized in Table 1.

Table 1. Interaction cross sections for  $^{56}\text{Fe}$ -nucleus scatterings at 1.88 GeV/N calculated with RHS and LHS of eq.(1) with the SKV interaction.

Target	$^7\text{Li}$	$^9\text{Be}$	$^{12}\text{C}$	$^{32}\text{S}$	$^{65}\text{Cu}$	$^{109}\text{Ag}$	$^{184}\text{W}$	$^{207}\text{Pb}$	$^{238}\text{U}$
$\sigma_{\text{int}} \quad (\text{b})$	1.548	1.651	1.758	2.448	3.094	3.744	4.610	4.884	5.179
$\pi(R_p + R_t)^2 \quad (\text{b})$	1.562	1.662	1.766	2.448	3.107	3.747	4.619	4.894	5.191

Here we stress the important implication of the interaction radius  $R_p$ . Thus far the interaction cross section has been studied with the semiempirical formula

$$\sigma_{\text{int}}(p,t) = \pi r_0^2 (A_p^{1/3} + A_t^{1/3} - \delta)^2, \quad (3)$$

where the "overlap parameter"  $\delta$  is meant to represent the diffuseness and partial transparency of the nuclear surfaces. The additivity relationship eq.(1) indicates that the parameters  $r_0$  and  $\delta$  should be defined at each nucleus  $A_p$  (and  $A_t$ ), and that those are considered to be characteristic quantities of the nucleus. Furthermore, since the interaction cross sections of nuclei are essentially independent of energy from 0.1 to 30A GeV<sup>6)</sup>, the interaction radius  $R_p$  is considered to be an energy independent characteristic nuclear radius in nucleus-nucleus scatterings (like the charge radius determined from electron scattering).

The analysis of the track detector is one of the important application of the idea of the interaction radius  $R_p$ . The interaction mean free path (IMFP)  $\lambda_p$  of the projectile  $p$  in the emulsion is given by

$$1/\lambda_p = \sum_i n_i \sigma_{\text{int}}(p,i), \quad (4)$$

where  $n_i$  is the composition of the nuclear component  $i$  in the emulsion and  $\sigma_{\text{int}}(p,i)$  is the interaction cross section between the projectile  $p$  and the target  $i$ . With the employment of eq.(1), eq.(4) can be expressed by

$$1/\lambda_p = AR_p^2 + BR_p + C, \quad (5)$$

with

$$A = \pi \sum_i n_i, \quad B = 2\pi \sum_i n_i R_i, \quad \text{and} \quad C = \pi \sum_i n_i R_i^2. \quad (6)$$

The coefficients  $A$ ,  $B$  and  $C$  are calculated for typical emulsions Ilford G5 and Fuji ET7B<sup>7)</sup>, and those show very weak energy dependence. The interaction radius  $R_p$  and IMFP calculated for typical nuclei are tabulated in Table 2. The proton IMFP  $\lambda_p = 32.7$  cm and  $\lambda_p = 32.6$  cm are obtained, respectively, for Ilford G5 and Fuji ET7B. In Fig.2 we compare the calculated IMFPs in Ilford G5 for 1.8 GeV/N projectiles with the experimental ones obtained with  $^{40}\text{Ar}$  beam<sup>8)</sup>. We find nice agreement with the experimental IMFPs by  $^{40}\text{Ar}$  beam. Since nice agreement between calculated and experimental IMFPs suggests the possibility of the determination of the interaction radius from

the emulsion experiment, we derive the interaction radii ( $R_p^*$ ) from experimental IMFPs by employing A, B and C values calculated. Then we obtain reasonable agreement between calculated  $R_p$  and derived  $R_p^*$ , while the ambiguity due to the experimental error is large,

Table 2. The rms matter ( $r_{rms}$ ) and interaction ( $R_p$ ) radii and IMFPs ( $\lambda_p$ ) of projectile nuclei in the emulsion at 1.88 GeV/N calculated with the SKV interaction<sup>9)</sup>

Proj.	$r_{rms}$	$R_p$	$\lambda_p^{a)}$	$\lambda_p^{b)}$	Proj.	$r_{rms}$	$R_p$	$\lambda_p^{a)}$	$\lambda_p^{b)}$
$^4\text{He}$	1.76	1.52	18.8	18.4	$^{40}\text{Ar}$	3.37	4.30	7.9	7.6
$^6\text{He}$	2.47	2.07	15.5	15.2	$^{39}\text{K}$	3.33	4.24	8.0	7.7
$^8\text{He}$	2.43	2.38	14.0	13.6	$^{40}\text{Ca}$	3.34	4.26	8.0	7.7
$^7\text{Li}$	2.45	2.23	14.7	14.3	$^{48}\text{Ca}$	3.51	4.53	7.5	7.1
$^9\text{Be}$	2.44	2.45	13.6	13.3	$^{56}\text{Fe}$	3.69	4.82	6.9	6.6
$^{11}\text{B}$	2.44	2.61	13.0	12.6	$^{58}\text{Ni}$	3.72	4.86	6.9	6.6
$^{12}\text{C}$	2.44	2.67	12.7	12.3	$^{63}\text{Cu}$	3.84	5.08	6.5	6.2
$^{14}\text{N}$	2.54	2.85	12.0	11.6	$^{65}\text{Cu}$	3.88	5.12	6.4	6.2
$^{16}\text{O}$	2.58	2.98	11.5	11.1	$^{79}\text{Br}$	4.11	5.48	5.9	5.6
$^{19}\text{F}$	2.78	3.25	10.6	10.2	$^{81}\text{Br}$	4.14	5.52	5.9	5.6
$^{20}\text{Ne}$	2.83	3.33	10.4	10.0	$^{107}\text{Ag}$	4.51	6.04	5.2	5.0
$^{23}\text{Na}$	2.92	3.50	9.9	9.5	$^{109}\text{Ag}$	4.54	6.10	5.1	4.9
$^{24}\text{Mg}$	2.94	3.55	9.7	9.4	$^{120}\text{Sn}$	4.67	6.29	4.9	4.7
$^{27}\text{Al}$	3.00	3.68	9.4	9.0	$^{127}\text{I}$	4.77	6.40	4.8	4.6
$^{28}\text{Si}$	3.02	3.72	9.3	8.9	$^{181}\text{Ta}$	5.36	7.27	4.1	3.9
$^{31}\text{P}$	3.14	3.93	8.7	8.4	$^{184}\text{W}$	5.39	7.30	4.0	3.8
$^{32}\text{S}$	3.18	4.00	8.6	8.2	$^{208}\text{Pb}$	5.56	7.66	3.8	3.6
$^{35}\text{Cl}$	3.26	4.12	8.3	8.0	$^{238}\text{U}$	5.87	8.03	3.5	3.3

Units:  $r_{rms}$  in fm,  $R_p$  in fm and  $\lambda_p$  in cm.

Emulsions: a) Ilford G5 and b) Fujii ET7B.

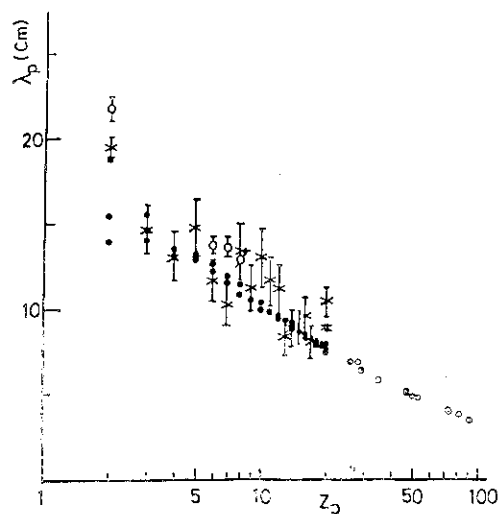


Fig.2. The IMFPs in Ilford G5 at 1.8 GeV/N calculated with SKV interaction (solid circle)<sup>9)</sup> and experimental IMFPs obtained with  $^{40}\text{Ar}$  beam<sup>8)</sup> (cross) and obtained with 2.1 GeV/N nuclear beams<sup>10)</sup> (open circle).

Thus we summarize that the interaction cross sections of medium and high energy nucleus-nucleus scatterings are generally well understandable in terms of the interaction radius, and those are nicely reproduced by the

realistic Glauber model calculation with the employment of the realistic nuclear wave functions. This nice agreement between the experimental and theoretical values may give a significant one step to study the consistency between normal nuclear physics and nuclear physics for nuclei far from stability.

The work has been performed with the collaboration of Dr. Y. Okuhara. The author thanks Prof. M. Muraoka for his hospitality. The numerical calculation is performed with FACOM M380 at INS.

#### References

- 1). I.Tanihata et al., Phys.Lett. 160B (1985) 380.
- 2). I.Tanihata et al., Phys.Rev.Lett. 55 (1985) 2676.
- 3). H.Sato and Y.Okuhara, Phys.Lett. 162B (1985) 217.
- 4). K.Yazaki, Nucl.Phys. A277 (1977) 189.
- 5). V.Franco and G.K.Varma, Phys.Rev. C18 (1978) 349.
- 6). A.S.Goldhaber and H.H.Heckman, Annu.Rev.Nucl.Part.Sci. 28 (1979) 161.
- 7). W.H.Barkas, Nuclear Research Emulsions (Academic Press, NY, 1973) and C.Nagoshi, private communication.
- 8). R.Bhanja et al., Phys.Rev.Lett. 54 (1985) 771.
- 9). H.Sato and Y.Okuhara, Phys.Lett. B, to be published.
- 10). H.H.Heckman et al., Phys.Rev. C17 (1978) 1735.

### 36. Sub-barrier fusion reactions: Multi-phonon and Isotope Effects

N.Takigawa and K.Ikeda

Department of Physics, Tohoku University, Sendai 980, Japan

Coupled channel equations have been used to understand the large enhancement of sub-barrier fusion cross section over the potential model prediction in terms of the effects of nuclear intrinsic degrees of freedom. In this approach, simplified equations which do not explicitly treat the angular momentum problem have often been adopted to achieve qualitative understanding of the mechanism of the enhancement.

In this contribution, we showed that such simplified equations can be derived<sup>1)</sup> from the original coupled channel equations which take into account the angular momentum problem if one ignores the change of the centrifugal potential barrier due to nuclear intrinsic excitation. To this end, we made use of completeness relations concerning the Clebsch-Gordan and Racah coefficients. The scale of coupled channel calculations is thus much reduced. The multipolarity of nuclear intrinsic excitation appears in the coupling strength as a scaling factor.

We then used these coupled channel equations of reduced scale to discuss multi-phonon and "isotope" effects, as well as the importance of the pre-fusion nuclear excitation<sup>1,2)</sup>. We analyzed the fusion cross section for  $^{58}\text{Ni} + ^{58}\text{Ni}$ ,  $^{58}\text{Ni} + ^{74}\text{Ge}$ ,  $^{74}\text{Ge} + ^{74}\text{Ge}$ ,  $^{32}\text{S} + ^A\text{Mo}$ ,  $^{36}\text{S} + ^A\text{Mo}$  ( $A: 92, 94, 96, 98, 100$ ),  $^{112}\text{Sn} + ^{116}\text{Sn}$ ,  $^{112}\text{Sn} + ^{122}\text{Sn}$  systems. We assumed the Akyuz - Winther potential<sup>3)</sup>, and took into account the first  $2^+$  phonon for each nucleus. Our study shows the followings<sup>1,2)</sup>.

The two-phonon states of a vibrational mode of excitation yields a sizable extra enhancement of the sub-barrier fusion cross section, in addition to the one-phonon state, especially at low bombarding energies. The extra effect of higher phonon states is small. The pre-fusion excitation is considerable for

the  $2^+$  vibration due to long range Coulomb excitation, and moderates the enhancement of the fusion cross section. The enhancement gets larger in the order of  $^{58}\text{Ni}+^{58}\text{Ni}$ ,  $^{58}\text{Ni}+^{74}\text{Ge}$ ,  $^{74}\text{Ge}+^{74}\text{Ge}$ , and  $A=92,96,100$  for  $^{36}\text{S}+^A\text{Mo}$  scattering. This "isotope" effect can be understood as a reflection of the excitation energy of the 1st excited  $2^+$  phonon state and its amplitude of the zero point motion (cf. eq.(2.25) of ref.4). The same reasoning can be applied to explaining the absence of strong isotope-dependence of the fusion cross section for Sn system.

Our calculations do not, however, explain the clear isotope effect observed in  $^{32}\text{S}+^A\text{Mo}$  system<sup>5,6</sup>). As suggested in ref.5, the effects of nucleon transfer may resolve this problem.

A puzzle is that, although the order of enhancement mentioned above is in line with the experimental data, the magnitude of the reduced fusion cross section for  $^{58}\text{Ni}+^{58}\text{Ni}$ ,  $^{58}\text{Ni}+^{74}\text{Ge}$  and  $^{74}\text{Ge}+^{74}\text{Ge}$  has been predicted by our coupled channel calculations to be in the reversed order of the experimental data<sup>6</sup>). Different considerations, such as the change of view from a vibrational excitation to a rotational excitation for  $^{74}\text{Ge}$ , or the consideration of the stability of the compound system, might be required to resolve this problem.

#### References:

- 1) N.Takigawa and K.Ikeda, preprint, Tohoku University, 1985
- 2) N.Takigawa and K.Ikeda, to be published.
- 3) R.A.Broglia and Aa.Winther, Heavy Ion Reactions (Benjamin, London, 1981)
- 4) N.Takigawa, Heavy Ion Fusion Reactions (World Scientific, Singapore, 1984) p.20; Proc. of the Tsukuba International Symposium on Heavy Ion Fusion Reactions, Sep.3-5, 1984, eds. K.Furuno and T.Kishimoto
- 5) R. Pengo et al., Nucl.Phys. A411(1983)255
- 6) M.Beckerman, Phys.Rep. 129(1985)145

## 37. Subbarrier Fusion Reactions

Akira Iwamoto and Kichinosuke Harada

Department of Physics, Japan Atomic Energy Research Institute

Enhancement of the subbarrier fusion reaction data over the one dimensional barrier penetration calculation was attacked by several theoretical models.<sup>1)</sup> Coupled channel model is a typical one and it predicts an enhancement of the cross section. The calculation, however, is very complicated and it is hard to get a good result for heavy systems since so many channels are necessarily coupled. Some authors pointed out the possibility of the neck formation between two nuclei when they come close together and it was calculated by the schematic coupled channel model<sup>2)</sup> and by a classical dynamical model<sup>3)</sup>. The neck in the former model is very abstract and is not directly related to the classical idea of the neck. The latter one performed the WKB calculation for the one dimensional necking motion and the coupling of it to the relative motion is restricted too severely. We propose here a new model of the subbarrier fusion reaction based on the idea of the neck formation. The details of our model is given in Ref.4.

The fusion cross section in our model is written as

$$\sigma_{\text{fus}} = \frac{\pi}{k^2} \sum_L (2L+1) \{ |S_{\alpha\alpha}^{(L)}|^2 + |S_{\beta\alpha}^{(L)}|^2 \},$$

where suffix alpha means the no neck state and beta means the neck formed state. As this expression shows, we adopt a two state approximation for the fusion process, that is, the fusion occurring through the penetration of the original no neck barrier (first term) and the fusion occurring through the formation of the neck in the course of the reaction. The former term is calculated by the standard Hill-Wheeler form and the latter is calculated by the perturbation for the transition from the no neck state to the neck formed state and also by using the semiclassical evaluation of the time dependent Green's function. The essential quantity in this treatment is the potential energy for the no neck and neck formed state. It is calculated by the method of Krappe et al.<sup>5)</sup> by specifying the shape

of the no neck and neck formed state. The parametrization of the shape was performed by starting from the two-center potential<sup>4)</sup> and the parameter values were fixed independent of the system. One another important quantity is the matrix element of the transition from no neck state to the neck formed state. It was replaced by the phenomenological derivative Woods-Saxon form with the standard value of the radius and the diffuseness parameter. The strength parameter is determined by the best value for the Ni+Ni system and the value (1.0 MeV at maximum) was fixed for all other system.

For the numerical calculations, we choose 6 mass symmetric systems

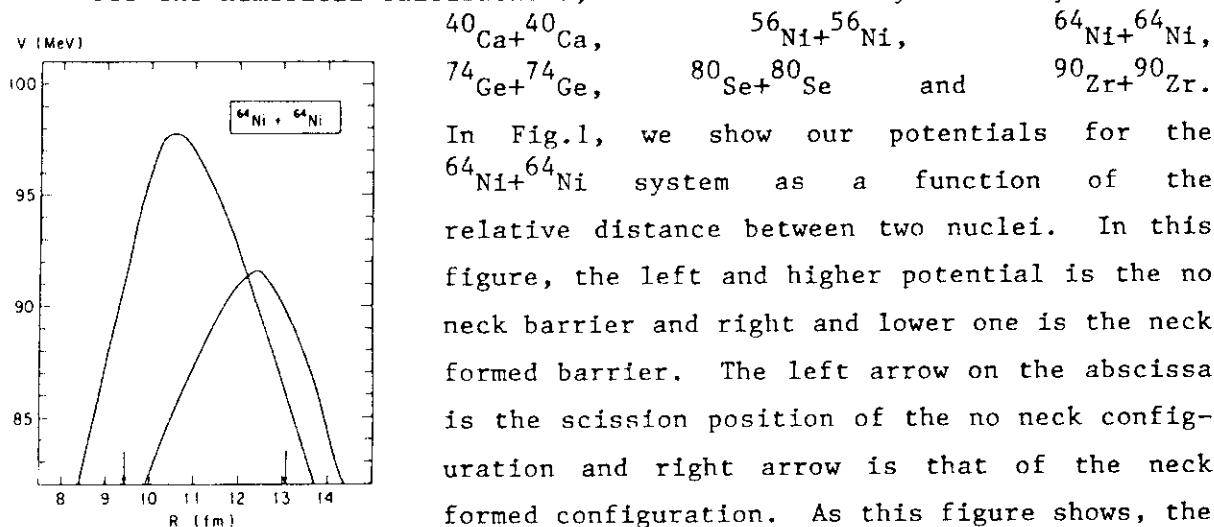


Fig.1.

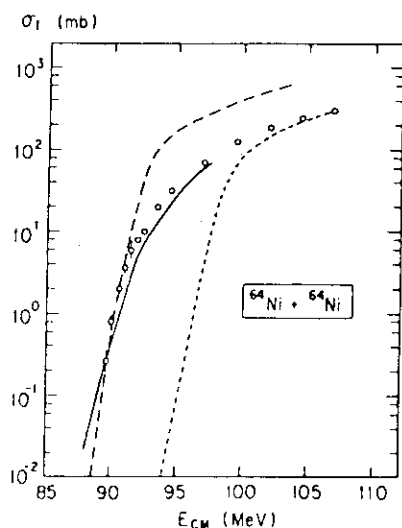


Fig.2.

In Fig.1, we show our potentials for the  $^{64}\text{Ni}+^{64}\text{Ni}$  system as a function of the relative distance between two nuclei. In this figure, the left and higher potential is the no neck barrier and right and lower one is the neck formed barrier. The left arrow on the abscissa is the scission position of the no neck configuration and right arrow is that of the neck formed configuration. As this figure shows, the formation of the neck leads to the reduction of the potential height and at the same time, the peak position moves to the larger center separation. Such kind of the change occurs for all other systems and the reduction of the height becomes larger as the system becomes heavier. Such tendency is consistent with the experimental fact that the enhancement of the fusion cross section becomes larger as the system becomes heavier. We show in Fig.2 the fusion cross section for this  $^{64}\text{Ni}+^{64}\text{Ni}$  system as a function of the center of mass energy. Small open circle is the experimental data from Ref.6 and short dashed curve is the

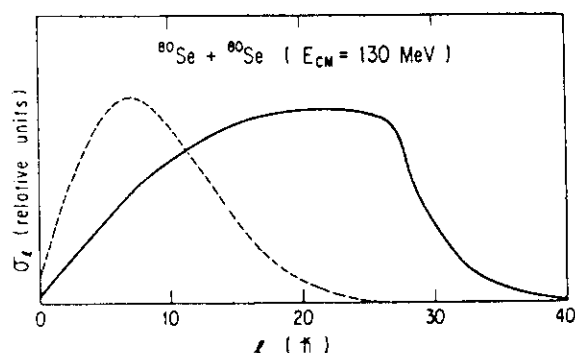


Fig.3.

unperturbed barrier penetration calculation and the long dashed curve is the unperturbed calculation for the neck formed potential. Our calculation shown by the solid curve lies in between these two curves and reproduces the data well. Fitting to the data is almost the same for other 5 systems except for the low energy part of the  $^{80}\text{Se} + ^{80}\text{Se}$ , where the

calculated cross section is not large enough to reproduce the data. The data of this system is much largely enhanced than other systems and will need a treatment which takes into account the effect of the nuclear structure. In Fig.3, we show the partial wave cross section for the  $^{80}\text{Se} + ^{80}\text{Se}$  system for the incident energy of 130 MeV. The solid line is our present calculation and the dashed line is the unperturbed calculation with arbitrary normalization for each calculation. From this figure, we find that the contribution from higher partial wave is largely enhanced in our calculation compared with the unperturbed one, which is consistent with the data of Ref.7.

In summary, our simple model of neck formation mechanism explains the enhancement of the subbarrier fusion data well. By fixing all the parameters to one set, we can reproduce all the data of mass symmetric systems well. The point of our model is that a part (typically 10 percent) of the incident flux is transfer to the neck formed barrier.

#### References

- 1) see for example, Proc.Int.Conf.on Fusion Reaction Below the Coulomb Barrier, MIT (1984) ed, S.G.Steadman, Lecture Note in Phys.219 (Springer, Berlin 1985)
- 2) H.K.Krappe et al.: Z.Phys.A314, 23 (1983)
- 3) C.E.Aguiar et al.: Phys.Rev.C31, 1969 (1985)
- 4) A.Iwamoto and K.Harada: JAERI-memo 61-074 (1986)
- 5) H.J.Krappe, J.R.Nix and A.J.Sierk: Phys.Rev.C20, 992 (1979)
- 6) M.Beckerman et al.: Phys.Rev.C25, 837 (1982)
- 7) P.J.Nolan et al.: Phys.Rev.Lett.54, 2211 (1985)



### 38. Transfer cross sections for $^{28}\text{Si} + ^{58,62}\text{Ni}$ reactions near the Coulomb barrier

Yasuharu Sugiyama, Yoshiaki Tomita, Hiroshi Ikezoe, Kazumi Ideno, Naomoto Shikazono, Norihisa Kato\*, Hiroshi Fujita\*, Tsuyoshi Sugimitsu\* and Shigeru Kubono\*\*

Department of Physics, Japan Atomic energy Research Institute, \*Department of Physics, Kyushu University, \*\*Institute for Nuclear Physics, University of Tokyo

Quasielastic reactions of  $^{28}\text{Si} + ^{58,62}\text{Ni}$  were carried out<sup>1)</sup> at JAERI tandem accelerator in order to investigate correlation between quasielastic reaction strength and the enhanced subbarrier fusion cross section<sup>2,3)</sup>. The  $^{28}\text{Si}$  beam energy was 110 MeV which was about 40% higher than the Coulomb barrier. The energy spectra were measured with an energy resolution of  $\sim 250$  keV by using the heavy-ion spectrograph<sup>4)</sup> named "ENMA". The spectrograph has a characteristic feature that a kinematic momentum shift  $k$  is compensated well, so that a high energy resolution is achieved over a wide range of  $k$ . The outgoing particle were momentum analyzed in the spectrograph ENMA and detected in the focal plane with a 40-cm-long hybrid focal plane detector<sup>5)</sup>. From a measurement of total energy  $E$ , energy loss  $\delta E$  and position BP an unambiguous determination of mass, atomic number,  $Q$  value and atomic charge state  $q$  were possible. Four nuclei  $^{29}\text{Si}$ ,  $^{30}\text{Si}$ ,  $^{27}\text{Al}$  and  $^{26}\text{Mg}$ , which were produced from neutron-pickup or proton-stripping reactions, were observed in addition to elastically scattered  $^{28}\text{Si}$ . Other reaction producing nuclei could not be identified because of their small yields.

Energy spectra obtained for  $12^+$  charge state at  $\theta_{\text{lab}} = 34.7^\circ$  from the reactions  $^{62}\text{Ni}(^{28}\text{Si}, ^{29}\text{Si})^{61}\text{Ni}$ ,  $^{62}\text{Ni}(^{28}\text{Si}, ^{30}\text{Si})^{60}\text{Ni}$ ,  $^{58}\text{Ni}(^{28}\text{Si}, ^{29}\text{Si})^{57}\text{Ni}$  and  $^{58}\text{Ni}(^{28}\text{Si}, ^{30}\text{Si})^{56}\text{Ni}$  are shown in Fig.1. Energy resolution of  $\sim 250$  keV made it possible to resolve transitions to low-lying discrete levels. Angular distributions for the elastic and

inelastic scatterings to the first  $2^+$  states in  $^{58}\text{Ni}$ ,  $^{62}\text{Ni}$  and  $^{28}\text{Si}$  are shown in Fig.2. Angular distributions from the neutron-pickup reactions  $^{58,62}\text{Ni}(^{28}\text{Si}, ^{29}\text{Si})$  and  $^{58,62}\text{Ni}(^{28}\text{Si}, ^{30}\text{Si})$  are shown in Fig.3. Strong isotope dependence in the reaction cross sections is observed. Following results are obtained by analyzing these angular distributions.

For the elastic and inelastic scattering, the coupled-channel calculations were performed with the code Ptolemy<sup>6)</sup>. The results are shown by solid lines in Fig.2. The potential parameters obtained are as follows:  $V=50$  MeV,  $W=10$  MeV,  $r_0=1.2$  fm,  $a=0.65$  fm. The imaginary potential depth  $W$  is reduced by half compared to the one obtained at  $E_{\text{lab}}=140$  MeV. This reduction leads to the increase of the transfer cross sections.

For the neutron-pickup reactions, DWBA calculations were performed with the code Ptolemy. The results are shown by solid and dashed lines in Fig.3. The spectroscopic factors obtained from the  $(p,d)$  and  $(d,p)$  reactions are used for the one-neutron pickup reaction ( $^{28}\text{Si}, ^{29}\text{Si}$ ). For the two-neutron pickup reaction ( $^{28}\text{Si}, ^{30}\text{Si}$ ), we set spectroscopic factors to 1 and used a cluster wave function for the transferred dineutron. The angular distributions for the ground state transitions are reproduced well by the simple DWBA calculations. The isotope dependence of the reaction cross sections results mainly from the different  $Q$  values between the systems  $^{28}\text{Si}+^{58}\text{Ni}$  and  $^{28}\text{Si}+^{62}\text{Ni}$ . The total reaction cross sections observed at the present experiment have isotope dependence similar to the one observed in the subbarrier fusion yields.

#### References

- 1) Y.Sugiyama et al., to be published.
- 2) S.G.Steadman, ed., Intern. Conf. on Fusion reactions below the Coulomb barrier, Lecture Notes in Physics, Vol.219(Springer, Berlin, 1985).
- 3) A.M.Stefanini et al., Phys. Rev. C30(1984)2088.

- 4) Y.Sugiyama et al., Nucl. Instr. Methods 187(1981)25;  
Z.Phys. 322(1985)579.
- 5) E.Takekoshi et al., Nucl. Instr. Methods A237(1985)512.
- 6) D.H.Gloeckner et al., Argonne National Laboratory report  
No. ANL-76-11(1978), unpublished; M.J.Rhoades-Brown et  
al., Phys. Rev. C21(1980)2417,2436.

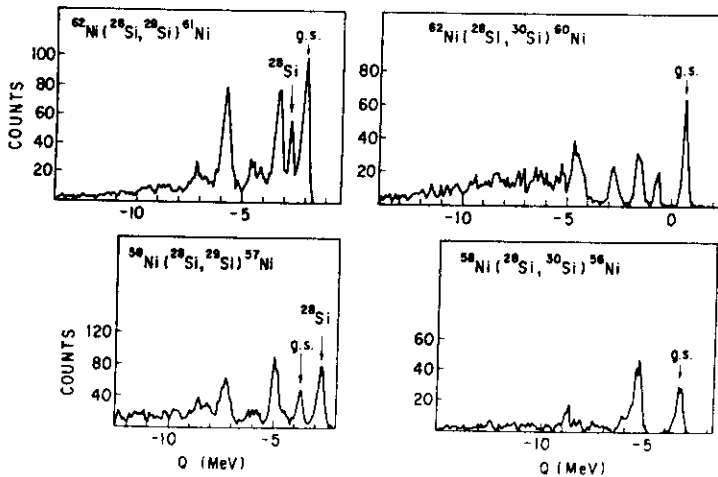


Fig.1 Spectra obtained for  $12^+$  charge state from the  $(^{28}\text{Si}, ^{29}\text{Si})$  and  $(^{28}\text{Si}, ^{30}\text{Si})$  reactions on  $^{58}\text{Ni}$  and  $^{62}\text{Ni}$  at  $\theta_{\text{lab}} = 34.7^\circ$ .

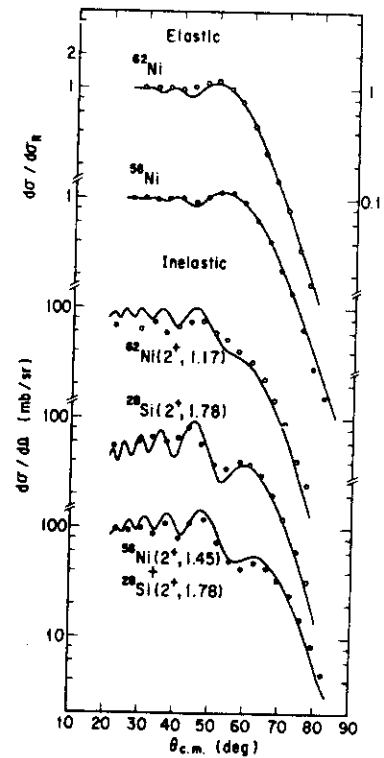


Fig.2 Angular distributions for the elastic and inelastic scatterings. The solid lines are coupled-channel calculations.

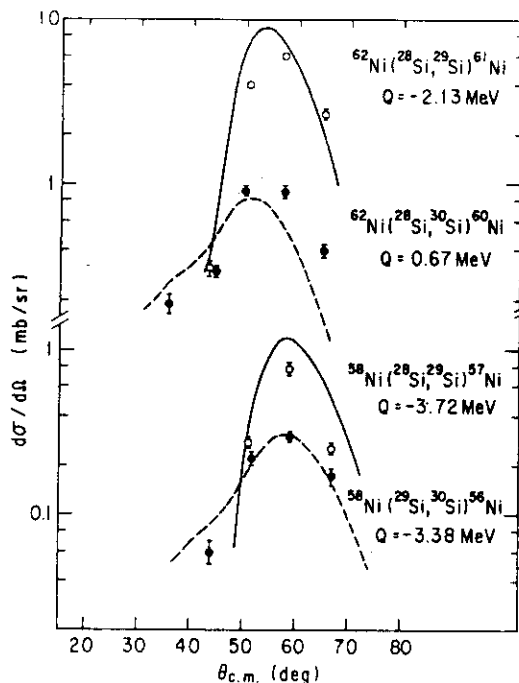


Fig.3 Angular distributions of the ground state transitions from the neutron-pickup reactions. Solid and dashed lines are DWBA calculations.